Numerical Investigation of the Effect of Flow Turbulence on Heterogeneous Reaction Rates

Jonas Krüger

June 14, 2017

Abstract

In this thesis, the effect of turbulence on heterogeneous reactions is investigated. After a short introduction into the state-of-the-art of turbulent combustion modelling, an overview over the numerical methods and models used to simulate homogeneous and heterogeneous combustion in turbulent flows is given. Then, a brief introduction into the most important features of the numerical implementation is provided.

Simulations featuring a simple heterogeneous reaction system involving a passive reactant are performed with a compressible Direct Numerical Simulation (DNS) Computational Fluid Dynamics (CFD) code, called ”The Pencil Code”. Different particle numbers, sizes and flow properties are investigated, and an inhibiting effect of the turbulence on the reaction rates for high particle numbers is found.

In further studies using the simplified model, the inhibiting effect is quantified for a range of particle numbers, and a model predicting the inhibiting effect from flow and particle properties is proposed.

A sub model for the detailed modelling of particles burning in a cloud of gas, the ”Stanford Code” is extended and implemented into ”The Pencil Code”. The proposed model to predict the inhibiting effect is compared against data from simulations that use real chemistry represented by a simple reaction mechanism. Agreement between the proposed model obtained from the simplified reaction systems and the data from the more complex combustion system is found to be good.

The performance of the proposed model is discussed and recommendations for further work to increase the predictive capabilities of the model are given.

Preface

This thesis is submitted to the Norwegian University of Science and Technology (NTNU) for partial fulfillment of the requirements for the degree of philosophiae doctor.
This doctoral work has been performed at the Department of Energy and Process Engineering, NTNU, Trondheim, with Professor Terese Løvås as main supervisor and with Associate Professor Nils E.L. Haugen as co-supervisor.

The author received funding from strategic funds of the NTNU and is grateful to the visiting PhD fellow program of the Nordic Institute of Theoretical Physics (Nordita) for funding his stay in Stockholm.

Acknowledgements

First, I would like to thank both my supervisors, Terese Løvås and Nils Erland Leinebø Haugen for their support, patience and encouragement through sometimes frustrating, but always exciting times. Thanks to your help, I am now much closer to being a scientist than I was three years before, and it would have not been possible without you.

I am also very grateful to Dhrubaditya Mitra for his collaboration and for inviting me to Stockholm in the framework of the visiting PhD program. It is a memory that I will always look back with a broad, but also slightly confused smile. Apparently, engineers are easily overwhelmed by astrophysics.

What makes the constant struggle of science bearable? Sharing it with people having the same problem. I thank all the people I ate rice, ice or cake, drunk coffee or beer, bouldered, cross country skied, climbed, ran, hiked, talked, cooked, barbecued, played Dominion, saved the world and brewed with in the last three years. It was a pleasure to be part of so many conversations that began with a serious topic and became utterly hilarious with astonishing speed, mostly by application of reason and logic in all the wrong ways.

A german saying goes: ”If your children are young, give them deep roots. If they are old enough, provide them with wings.” My parents Brigitta and Roland have done that and so much more, I am happy and grateful to have them in my life. I am always looking forward to come back to my roots. And what could have been better for my young, slightly overdeveloping ego than to have a younger brother who ends up half a head higher, hm, Tilman?

Last but not least is the person who endures, among others, my creative cooking, my lack of control over my voice level and my trust in the soundness of half baked plans. And, after all that, still does her best to laugh at even the worst puns I just had to make. Or, at least, roll her eyes. Anna, around you being a better me is much easier and it is also very fun. I presume you already know this, but I thought I should also say it here. Just in case.

Papers and Presentations

Papers included in the thesis

- Paper 1: Jonas Krüger, Nils E.L. Haugen, Terese Løvås and Dhrubaditya Mitra (2015). *A study on the coupling between isotropic turbulence and heterogeneous reactions*, Proceedings of MekIT'15 Eighth National Conference on Computational Mechanics. International Center for Numerical Methods in Engineering (CIMNE), p. 243-257.

- Paper 2: Jonas Krüger, Nils E.L. Haugen, Dhrubaditya Mitra and Terese Løvås (2017). *The effect of turbulent clustering on particle reactivity*, Proceedings of the Combustion Institute 36 p. 2333-2340.

- Paper 3: Joanna Lazar, Nils E.L. Haugen, Jonas Krüger and Andrzej Szlek, (2016). *Numerical Study of Hydrogen Inhibition of Char Gasification Using Detailed Hetero- and Homogeneous Chemical Kinetics* in Energy & Fuels 30, 4411-4418.

- Paper 4: Nils E.L. Haugen, Jonas Krüger, Dhrubaditya Mitra and Terese Løvås (2017). *The effect of turbulence on mass and heat transfer rates of small inertial particles*, submitted to Journal of Fluid Mechanics.

- Paper 5: Jonas Krüger, Nils E.L. Haugen and Terese Løvås (2017). *Correlation effects between turbulence and the conversion rate of pulverized char particles*, submitted to Combustion & Flame.

The authors contributions on joint papers

The papers on which this thesis is based are co-authored according to the following description. For the presented papers, the supervisor (Terese Løvås) and co-supervisor (Nils E.L. Haugen) contributed by giving feedback and suggestions during the production of the data and papers; the author has performed the following work:

- Paper 1: The author set up and conducted the simulations, as well as creating and using the scripts necessary for post-processing. The paper was co-written with Nils Haugen. Terese Løvås gave feedback on theoretical as well as language aspects of the work. Dhrubaditya Mitra contributed

with feedback and suggestions and additionally helped with establishing the theoretical framework of the analysis.

- Paper 2: The author set up and conducted the majority of simulations, as well as creating and using the scripts necessary for post-processing. Nils Haugen supplied additional data. Evaluating the results and writing the paper was a joint effort with Nils Haugen. The theory section was co-authored with Dhrubaditya Mitra, who also supplied suggestions and feedback during the writing process. Terese Løvås contributed with reviews and suggestions on both the technical as well as the theoretical aspects of the work.

- Paper 3: The author extended the Stanford code simulation software to read mechanism files. This was then used by the main author Joanna Lazar to run simulations. The author also provided suggestions and revised the article before submission.

- Paper 4: The author extended diagnostics used in this work, as well as co-writing and revising the paper. Running the simulations, postprocessing of the results and the main writing effort was done by Nils Haugen.

- Paper 5: The author extended the simulation software with what was necessary to simulate the cases, set up and conducted the simulations, and created and used the post-processing scripts. The author wrote the paper and evaluated and interpreted the results. Nils Haugen supplied values for the proposed model to compare against and auxiliary data. Terese Løvås reviewed the work and pointed out weaknesses in the description of it, which have been subsequently addressed.

Other papers and conference contributions

Co-authored papers, conference contributions and poster presentations that were created during the time of the PhD study:

- Jonas Krüger, Nils E.L. Haugen and Terese Løvås, (2016). *What is the effect of turbulence on the heterogeneous reaction rates in the high and low Damköhler regimes?*, 9th International Conference on Multiphase Flow, May 22-27, Firenze, Italy.

- Jonas Krüger, Nils E.L. Haugen, Dhrubaditya Mitra and Terese Løvås, (2015). *How important is turbulence for the rate of heterogeneous combustion of solid particles?*, Nordita Seminar, April 3, Trondheim, Norway.

- Jonas Krüger, Nils E.L. Haugen and Terese Løvås, (2015). *A study on the coupling between isotropic turbulence and heterogeneous reactions*, 8th National Conference on Computational Mechanics, May 18-19, Trondheim, Norway.

- Jonas Krüger, Terese Løvås and Nils E.L. Haugen (2015). *Analysing the performance of a reduced heterogeneous gasification mechanism.*, Nordic Flame Days, October 6-7, Snekkersten, Denmark.

- Jonas Krüger, Nils E.L. Haugen and Terese Løvås, (2015). *Comparison of reduced mechanisms for gasifying applications* , 5th International Workshop on Model Reduction in Reacting Flows, June 28 - July 1, Lübbenau, Germany.

- Jonas Krüger, Nils E.L. Haugen, Matthew B. Tilghman, Reginald E. Mitchell and Terese Løvås, (2014). *Numerical analysis of hydrogen inhibition during coal gasification.* (Work in progress poster), 35'th international symposium on combustion, August 3-8, San Francisco, United States of America.

- Jonas Krüger, Nils E.L. Haugen and Terese Løvås, (2015). *How does turbulent fluid motion influence heterogeneous combustion?*, 15th International Conference on Numerical Combustion, April 19-22, Avignon, France.

- Jonas Krüger, Nils E.L. Haugen and Terese Løvås, (2014). *Modelling of char particle conversion processes*, Joint British and Scandinavian-Nordic Section Combustion Meeting, March 27-28, Cambridge, United Kingdom.

Contents

Abbreviations

DNS Direct Numerical Simulation

RANS Reynolds Averaged Navier Stokes

LES Large Eddy Simulation

IGCC Integrated Gasification Combined Cycle

CCS Carbon Capture and Storage

CFD Computational Fluid Dynamics

SGS subgrid scale

CRIEPI Central Research Institute of Electric Power Industry

CLC Chemical Looping Combustion

FI Flame Index

PNN Projection onto Neighboring Nodes

PDF Probability Density Function

IFCM Infinitely Fast Chemistry Model

CMC Conditional Moment Closure

EDC Eddy Dissipation Concept

SLFM Steady Laminar Flamelet Model

IMF International Monetary Fund

UDF User Defined Function

EBU Eddy Break Up

PCC Pulverized Coal Combustion

CPD Chemical Percolation Devolatilization

PSR Perfectly Stirred Reactor

IEA International Energy Agency

BML Bray Moss Libby

SCM Shrinking Core Model

ECM Exposed Core Model

PCM Progressive Conversion Model

IPC Individual Particle Combustion

GC Group Combustion

RNG Re-Normalisation Group

SC Sheath Combustion

DDM Discrete Droplet Method

RHS Right Hand Side

Chapter 1

Introduction

1.1 Motivation

The International Energy Agency (IEA) predicts that global energy demand will rise by 30% until 2040 [63]. According to the International Monetary Fund (IMF), the rate of development of emerging countries is currently at about 4% annually and is predicted to be stable [64]. As more and more people are lifted out of poverty and countries develop, a rise in the per-capita use of electricity is inevitable. The relative abundance, low cost and wide distribution of coal means that especially developing countries will rely on it to fulfill their energy demands, even as developed countries lessen their dependence on it. Coal, a fossil fuel in widespread use since the industrial revolution, currently satisfies 29% of the demand of primary energy worldwide. According to even the most ambitious scenarios proposed by the IEA, coal will contribute 13% to the global primary energy supply in 2040 [63]. This, together with the rise in energy demand, implies that coal will stay an important source of primary energy for the near future.

Processes that use fossil fuels for power generation rely on the thermal fuel cycle to convert chemical energy stored in fossil fuels to electrical energy. In this cycle, a working fluid (usually water) undergoes the following stages:

- $1 \rightarrow 2$: The pressure of the working fluid is increased in a pump.
- $2 \rightarrow 3$: Fuel is burned. The resulting thermal energy is used to evaporate and increase the temperature of the working fluid. The working fluid is gaseous after this stage.
- $3 \rightarrow 4$: The fluid is expanded in a turbine and mechanical work is ex-

tracted. The pressure and temperature of the working fluid is decreased in this process. The mechanical work is then used to turn an electric generator, producing electrical power.

- $4 \rightarrow 1$: The working fluid is condensed in a heat exchanger. This stage extracts additional energy from the working fluid, but this energy is usually discarded into the environment.

The focus of this thesis is on *how* the fuel in the stage $2 \rightarrow 3$ is burned. There are a lot of different combinations of fuels and oxidisers that are used to supply heat to the overall process. The fuel itself has a large variability, with a wide variety of different coals being available. Moreover, biomass can also be added to the fuel, or burned exclusively [29]. Usually, the oxygen content of air is used as oxidiser, but also purified oxygen with recirculated flue gases can be used.

Depending on the fuel, oxidiser and the desired properties and operating conditions of the power plant, a set of different combustion technologies can be used. The main technologies used are:

- Grate-fired combustion, where relatively large fuel particles are transported along on a grate and burn over time. This was the earliest technology, which is still in use for waste and biomass combustion or for small applications [133].

- Fluidized bed combustion, where the fuel is crushed to small particles and placed in a combustion chamber together with a large amount of inert particles. The fuel and inert particles are kept in a fluidized state by the oxidiser flow, which also increases the dispersion of the fuel particles as well as heating the fuel particles quickly. The advantages of this technology are its fuel flexibility and high combustion efficiency [20].

- Pulverized Coal Combustion (PCC), where the fuel is milled to the size of dust particles and blown into the combustion chamber with preheated air. The preheated air dries the coal particles which are then ignited in the combustion zone [11]. This process can reach the highest temperatures. It is the most widely used coal combustion technology.

Apart from the main technologies to burn coal to produce heat, other technologies adapt or augment the process: A process called Chemical Looping Combustion (CLC) is proposed, where fuel is burned in a reactor together with an oxygen-containing solid oxidiser, which is then regenerated in a second reactor [60]. This

process could be used to reduce the cost for CO_2 capture. PCC or gasification can also be used in potentially carbon neutral energy systems, for example in an Integrated Gasification Combined Cycle (IGCC) with Carbon Capture and Storage (CCS) [11]. Being a critical step in the production of chemicals, turbulent heterogeneous combustion is very likely to be extensively used in the foreseeable future [96]. A wide range of the methods initially developed for PCC can also be employed for biomass combustion and gasification [31], but the peculiarities of biomass, for example its higher variance in composition and anisotropy compared to coal, further complicates its analysis.

Both design and control of fuel combustion systems rely heavily on empirical models [28], but recent advances in measurement techniques, and the use of simulations, has yielded greater understanding of those systems. This knowledge is then used to optimize existing and planned systems. As such, further research of combustion systems, be it study of the basic underlying processes or novel approaches, is warranted, as improved comprehension of turbulent pulverized combustion can lead to improvements in the areas of safety, economic viability and environmental friendliness.

Computer simulations take a prominent part in planning new and optimizing old combustion processes, and their use is increasing due to improved computational capabilities [95] as well as the increasing ease of use [6]. While simulations will always need experiments for validation, the ability to access all flow properties at all times, their variability and relative cheapness means that no new combustion system is planned without being simulated beforehand [129]. As turbulent heterogeneous combustion is a highly complex interaction of multiple processes, such as mass, momentum, species and energy transfer taking place at scales ranging from the scale of the combustion chambers (several meters) down to the scales of a single particle (micrometers), it is, and may always be, impossible to simulate and fully resolve an industrial system. Therefore, models are required to account for the scales that are not resolved, and these models are developed from analytical approaches, experimental investigations and detailed simulations of smaller parts of the industrial process. The topic of this thesis is the simulation of combustion of small particles in a flow with isotropic turbulence. The goal is to develop a sub-grid scale model that accounts for the effect of turbulence on the heterogeneously reacting particles. This model is intended to improve the predictive capabilities of simulations of industrial scale combustion systems, as well as providing a starting point for more extensive models.

1.2 Phase descriptions

The main element of a combustion system is usually a multiphase turbulent flow. Multiphase means that the flow contains several phases; gaseous, liquid or solid. These phases interact and transfer properties with each other, and it is these transfer processes that need to be calculated and studied in order to accurately simulate a combustion system. To successfully simulate a reacting turbulent flow with several species and phases, one has to account for and, if required, model several properties of the flow:

- An important process is the phase interaction, where two distinct phases interact with each other via e.g. evaporation, devolatilization, condensation, drying, momentum transfer or chemical reactions. In addition, individual droplets and particles can collide with each other.

- Processes that affect the shape and number of liquid and solid particles, which can be influenced by particles breaking up or sticking together, which can heavily influence the particle dynamics, number density and surface-to-volume ratio.

- Turbulence and vortices have to be accounted for over a wide range of scales, from the smallest possible scales of the flow, the Kolmogorov scales [106], to the scales of the industrial system. Turbulence is crucial for mixing processes in the fluid phases.

- Chemical reactions have to be accounted for since they change the flow composition, temperature, density, pressure and other connected properties. To properly define the physical properties such as viscosity, diffusivity, heat capacity or speed of sound, the species composition of the flow has to be known.

For each of the properties and processes mentioned above, there are a multitude of modelling approaches available. Care has to be taken to choose the ”right” model for the application to be simulated, as there is no one-size-fits-all method that will perform well in all imaginable scenarios. An overview over the most widely used, but by no means all, models to account for each of the bullet points is given below.

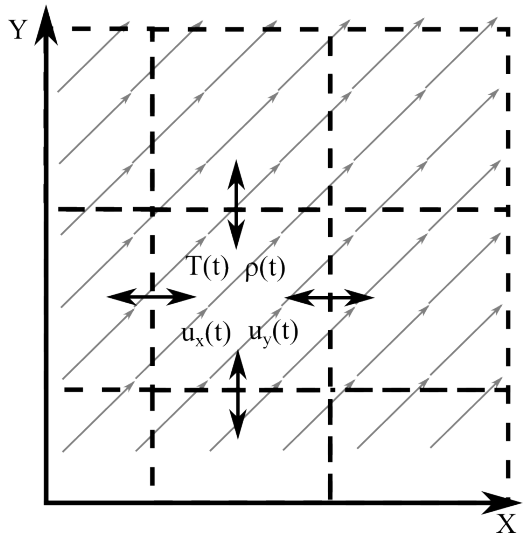

Figure 1.1: Graphical description of the Eulerian description: The phase flowing to the upper right (grey vectors) is divided into discrete volumes (dashed boxes). The phase in the boxes have certain properties (e.g. temperature T, density ρ, velocity in x and y direction u_x and u_y respectively), which are affected by the interaction with attached volumes (double-ended vectors).

1.2.1 Eulerian and Lagrangian phase descriptions

There are two main methods to describe a flow phase, its movement and its properties: the Eulerian and the Lagrangian description. The Eulerian description treats the phase as a continuum. The phase is divided into discrete volumes that are fixed in space, the evolution of the properties of the phase inside each of the discrete volumes is described and calculated. The discrete volumes can interact with the volumes that are attached to it. A sketch of the method can be seen in Fig. 1.1. The discrete volumes are the shaded boxes, and the interaction of directly neighbouring volumes is depicted as the double ended arrows. The evolution of properties of the phase inside the volume over time is determined by the interaction with the neighbouring volumes and the transport of properties over the volume boundaries by the flow field, which is depicted as grey arrows.

The Lagrangian description follows an entity, e.g. a fluid volume or particle along its path in a flow. Thus, the position of the entity changes, as do the properties of the entity. The change of properties is defined by the interaction of entities that are adjacent to it. Entities that are adjacent can be other Lagrangian entities, or entities that are fixed in space and described by an Eulerian approach. Since neighbouring entities can have different paths than the entity in question,

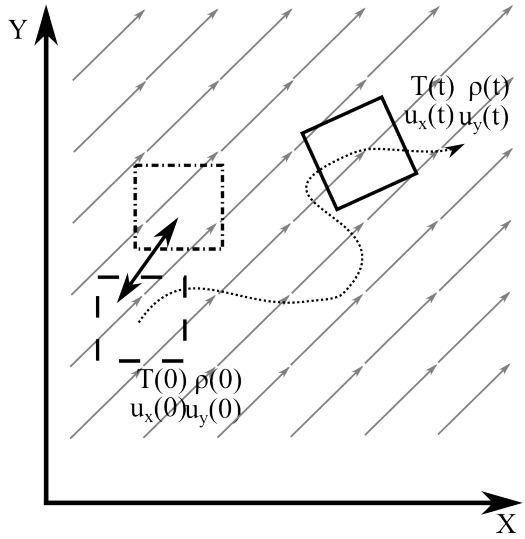

Figure 1.2: Graphical description of the Lagrangian description: An entity, which can be a flow packet or particle (dashed box) is followed on its path (dotted line) in a flow field (grey vectors). The properties of the entity is evolved taking into account interactions (double ended arrows) with neighbouring entities (dash dotted box). The position of the box changes over time (solid box), as are its properties.

or the entity has moved closer to different entities that are described by the Eulerian approach, the neighbouring entities have to be found in each step of the calculation. This description is outlined in Fig. 1.2. The entity, here shown as a dashed box at the starting time and solid box at time t, can be a particle or a fluid volume, travels along its path (dotted line) and its internal properties change due to interaction with other, neighbouring entities (dash dotted box). The neighbouring entities can change over time, as entities change position. For simulation problems featuring several phases, one can mix and combine these approaches to describe each phase in the most fitting manner. This also influences how the transfer processes between the phases have to be accounted for.

1.2.2 Multiphase system description

Most of the flows encountered in combustion research are of multiphase nature, meaning they consist of several distinct phases. Examples of this are spray flames (air, liquid fuel droplets) or pulverized coal jets (air, coal particles). Even all three phases can be present in a flow, but in this thesis, only descriptions featuring two different phases like gaseous-solid, liquid-solid and gaseous-liquid are described

for brevity. Additionally, the first phase in the following descriptions is the less dense of the two. Depending on the flow and the scale of the simulated systems, different combinations of descriptions can be used to describe the two phases:

- Eulerian-Eulerian: The Euler-Euler approach treats both the fluid as well as the solid matter as continuous phases and uses source terms to account for the transfer of properties from one phase to each other. This approach is often used in applications simulating large scale fluidized bed reactors, where the volume fraction of the solid matter is high [125]. This method is not employed here and only mentioned for completeness, the interested reader is referred to the work of Kuipers and van Swaaij [76] for an introduction to Euler-Euler methods.

- Lagrangian-Eulerian: In large scale simulations of fluidized beds, it may be more efficient to model rising bubbles of gas using a Lagrangian approach and the fluidized particles as the continuum. This approach is still in early development and a short description can be found in the work of van der Hoef [125].

- Euler-Lagrangian: This approach treats the fluid phase as continuous, with its movement described by the Navier-Stokes equation. The disperse phase is treated as distinct particles, single, or as a parcel of uniform particles. Each of these distinct parcels [34] interact with the surrounding fluid according to equations taking into account the local fluid properties, and the particle affects the flow using source terms in the equations defining the properties of the local fluid. An extensive review of Euler-Lagrangian modelling of multiphase flows can be found in Crowe et al. [28]. If the grid size of the Eulerian grid is much smaller than the typical diameter of the particles, the particles are resolved, while they are usually treated as point particles when the particle diameter is much smaller than the grid size. The topic of non-resolved or resolved particles is further explained in Section 1.3.2.

- Lagrangian-Lagrangian: If the scales of the system are very small, both the solid particles as well as the gas molecules are described with a Lagrangian approach. Due to its high cost, this method is restricted to the smallest of system scales [126].

1.3 Lagrangian particles in a fluid

When distinct particles are placed in a flow, their behaviour and interaction with the surrounding flow has to be modelled for several physical properties.

1.3.1 Momentum

The momentum of a particle influences its velocity and position. Maxey and Riley give a very detailed description for the motion of a hard sphere in non-uniform flow [90] and arrive at an equation that consists of four terms:

1. Shear stress and pressure of an undisturbed flow
2. Steady state drag, assuming creeping flow around the particle and no acceleration. For low Reynolds number, the drag coefficient is inversely proportional to the Reynolds number, which is referred to as the Stokes flow regime [119].
3. Virtual mass contribution due to no-slip condition at the particle surface. A film of fluid follows the movement and acceleration of the particle
4. Basset force which takes into account recent fluid acceleration

However, for small particles with a much higher density than the fluid, only the Stokes drag is taken into account. An overview over the different terms, their derivation and models can be found in the book of Crowe et al. [28].

1.3.2 Volume

When prepared for industrial combustion, solid fuels are usually ground down to small diameters. Coal particles used in PCC have a diameter between 0.001 and 0.1mm [47], while biomass particles can have a diameter up to several cm [31]. The article of van der Hoef et al. [125] gives an overview over the different methods to account for the particle volume in numerical simulations. In lab- and semi-industrial scale simulations, the particles are assumed to be point-source particles, where the particles volume is neglected when solving the flow field. This is only reasonable for dilute particle suspensions when the particle diameter is much smaller than the grid cell resolution, and a ratio of particle diameter and grid cell size of around 0.1-0.3 is encountered in published studies [85, 52]. For simulations of industrial systems, this method is adapted so that one particle

stands for a parcel of uniformly reacting particles, the so called Discrete Droplet Method (DDM) [5]. This approach greatly reduces the computational load of large-scale combustion simulations.

Due to the extreme computational cost, simulations where the surface and volume of a particle is resolved by the computational grid are still restricted to lab scale applications [30], or, for the case of reactive particles, to single particle studies [123, 124]. Moreover, there are several methods to describe the change in volume of the particle during conversion. First, there is the Exposed Core Model (ECM) [29], which assumes a shrinking particle where ash is ejected from the particle. In the Shrinking Core Model (SCM), a shrinking unreacted core of coal is surrounded by ash is assumed. The Progressive Conversion Model (PCM) treats the particle as undergoing reactions with constant diameter and uniformly changing composition [78]. In contrast to spray combustion, solid fuel break up or agglomeration is usually not taken into account. In the work of Haugen et al. [56], described in Subsection 2.3.3, a model is used that describes the change in particle size and density during combustion with a method developed by Thiele [121].

1.3.3 Shape

Depending on the grinding mechanism and type of fuel, the particles can have a wide range of shapes. While coal particles used in PCC are approximately spherical, biomass can be fibre shaped, or oblate or prolate spheroids [29]. For spherical particles, rotational moments can be neglected, which simplifies calculation and saves storage space. For non-spherical particles, this can not be assumed, and their shape has a profound influence on their motion [136] and alignment [135] in turbulence. An overview of the research activities on non-spherical particles can be found in [89].

1.3.4 Internal and external structure

Coal [66] and biomass [79, 31] particles are not homogeneously structured. Instead, they have fissures and pores and a large internal surface area, especially after devolatilization [96], which is further explained in Subsection 1.6.2. The porosity and internal surface area changes during the combustion of the particle. If not resolved [58], the effect of porosity on particle reactions can be described using Knudsen diffusion and a Thiele modulus [121], as used in the study of Haugen et al. [56, 55].

1.3.5 Temperature

The particle temperature is dependent on chemical reactions and energy transfer with the surroundings. Energy is transported via convective and radiative heat transfer. When the particle is small enough, it is usually treated as having uniform temperature, although particle-resolved studies are also put forward for a small number of particles [96]. While the full energy equation for the convective heat transfer [38] is quite complex, for most systems a simplified equation using a Nusselt number obtained by the Ranz-Marshall correlation [107] is used. Particle radiation can be described by models of different complexity, depending on the optical thickness of the fluid, presence of solid surfaces and other particles in the flow [56]. An overview over different radiation models can be found in [51, 5].

1.3.6 Particle collisions

For dilute systems, the collisions between particles can be neglected [117]. For simulations of systems with a very high volume fraction of particles, it may be more practical to describe both the gaseous as well as the solid phase with an Eulerian approach, as mentioned in Subsection 1.2.2 [125]. Simulations that take into account particle-particle collisions for Lagrangian particles and an Eulerian fluid become very expensive for large numbers of particles, and methods are developed to mitigate this problem [120]. From the list above it becomes clear that the research field of reacting particles in turbulent flows is extremely complex and features a multitude of distinct, interacting processes and attributes. While there is considerable research activity in each field, a ”complete” description of the combustion process is still out of reach. However, with a careful selection of modelling approaches for each sub-process, the predictive capabilities of simulations are already impressive and are used in every field of engineering [82].

1.4 Turbulence

Flows can be further classified by how they account for turbulence. Commonly, flow simulations are performed using either a Reynolds Averaged Navier Stokes (RANS), Large Eddy Simulation (LES) or Direct Numerical Simulation (DNS). Good descriptions of all methods are found in the books of Ferziger, Pope and Chung ([40], [106], [27]).

1.4.1 RANS

The RANS method decomposes the instantaneous flow field (i.e. the exact flow field at a given time) into a mean and a turbulent component. Then, an equation describing mean velocity is used, which is closed with a model to account for the effect of the turbulent components on the mean. The mean velocity $\overline{u}$ at a defined position in a general flow field is sketched as the flat dotted line in Fig. 1.3. Today, the RANS approach is most used in engineering applications, it comes with modest computational cost and uses the coarsest grid of the methods mentioned. Moreover, in most engineering applications, one is mainly interested in the mean flow. The drawback is that results are very dependent on which modelling approach is used to account for the effect of the turbulence, and choosing the "right" closure models for the system at hand is a non-trivial task. There are a lot of closure models to choose from that are tuned to different flow conditions [5]. The k-ε model introduced by Jones and Launder [65] is widely used and many studies of industrial scale systems have been published, e.g. ([53], [2]).

1.4.2 LES

LES, as opposed to RANS, calculates the instantaneous flow field. LES resolves the large scales that contain the bulk of the kinetic energy of the flow. As the resolved and unresolved scales interact with each other, a subgrid scale (SGS) model has to be used to account for the effect of the unresolved scales. Due to the decreasing cost of high-performance calculations, LES is getting used more and more, and the first simulations of lab or semi-industrial scale systems are reported [101]. For a detailed description of LES, the interested reader is referred to the book of Sagaut [110]. LES usually uses a grid that is finer than that of RANS, but coarser than for DNS. The resulting instantaneous velocity at one position in a general flow is shown as the solid curve in Fig. 1.3.

1.4.3 DNS

The first Direct Numerical Simulation of a turbulent flow was published in the seminal work of Kim et al. [70]. Of all three methods mentioned here, it is the most straightforward, as no modelling is needed. The velocity obtained at one position in a general flow is plotted as the dashed line in Fig. 1.3. The signal changes over time and shows variance at higher frequency than LES. If the boundary conditions of the simulation could be exactly replicated in an experiment with perfect

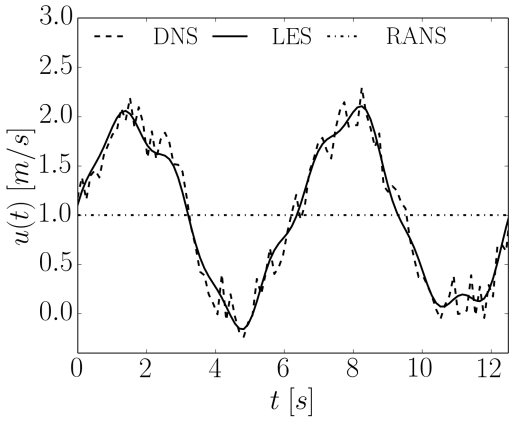

Figure 1.3: Velocity at one point in a turbulent flow as resolved by different turbulence modelling approaches, RANS, LES and DNS.

measurement tools, statistics of both simulation and experiment would be identical. All scales down to the smallest possible are resolved, so the simulation describes a turbulent system entirely. The disadvantage is its computational cost, which scales proportional to Re^3 [106], as the smallest scales become smaller when the flow Reynolds number is increased, which gives rise to a decrease in timestep as well. For comparable flows, DNS needs to have a finer grid than LES and RANS. This restricts use of this method to simple systems [25], although simulations of lab-scale systems have been published recently ([52],[85]).

1.5 Homogeneous combustion models

Homogeneous combustion models describe the chemical reactions that take place between species that are both in the gas phase, one example being a methane-air flame. Here, methane is the fuel and oxygen is the oxidising agent, and both reactants are in the gas phase. The progress in this field of study has been considerable in the last decades, helped by the increasing computer power and availability of combustion models. A good review of homogeneous combustion models can be found in the book of Poinsot and Veynante [104] or alternatively in the review paper of the current state of combustion modelling by Veynante and Vervisch [129].

The choice of methods differs dependent on the condition of the flow, for example wether fuel and oxidizer are premixed or not. Another condition influencing the choice of model is the turbulent time scale, which is inversely propor-

tional to the local fluid speed. In the case of premixed flames, the flame can be described by one variable that describes the transition from unburned to burned gases, the progress variable $c = (Y_f - Y_f^u)/(Y_f^b - Y_f^u)$, where Y_f is the local fuel mass fraction, Y_f^u the fuel mass fraction in the unburned state and Y_f^b the fuel mass fraction for the burned state. In this case, a high local speed can extinguish the flame by transporting too much energy away from it. The book of Lipatnikov [80] provides a good overview over methods used to describe premixed combustion. Among others, these methods are used:

- The Eddy Break Up (EBU) model, published by Spalding [116]. It assumes that the flow contains burned and unburned gas pockets, and that the rate of reaction from the unburned to the burned state is dependent on the turbulent mixing time.

- The Bray Moss Libby (BML) model, which calculates the probability to find either burned, unburned or burning gases at a certain time and position in the fluid [18]. When the reaction is fast, the probability to find burning gases is near zero, and the pdf becomes bimodal. The probability to find either burned or unburned gases is determined by the progress variable and the heat release factor of the reaction.

- Geometrical descriptions of the flame, such as the G-field equation [69], where a field describing the distance to the flame front is solved, or the flame surface density description [105], where the available flame surface per volume unit is calculated.

When non-premixed flames are concerned, the ratio of chemical time scale and the turbulent time scale become important. For the non-premixed case the mixture fraction $Z = \phi Y_f \left(Y_{f,0} - (Y_{O_2}/Y_{O_2,0}) + 1\right)/(\phi + 1)$ can be used to describe the flame. In this case Y_f is the local fuel mass fraction, $Y_{f,0}$ the initial fuel mass fraction in the fuel stream, Y_{O_2} the local oxidiser fraction, $Y_{O_2,0}$, the oxygen mass fraction in the oxidiser fuel stream and ϕ the equivalence ratio. Methods employing the concept of mixture fraction are among others:

- A very simple model is the Infinitely Fast Chemistry Model (IFCM). It uses a Probability Density Function (PDF) whose shape is defined by the mean and the variation of the mixture fraction to account for the mixing of fuel and oxidiser [21, 129].

- The Steady Laminar Flamelet Model (SLFM), modelling the reactions as laminar flamelets [103]. For each combustion system, the local flame structure has to be computed beforehand from laminar flames.

- Statistical descriptions, like the Conditional Moment Closure (CMC), which focuses on different states of flamelets which are computed and tabulated using a flamelet assumption beforehand ([71], [13])

- The Eddy Dissipation Concept (EDC), based on the work of Magnussen and Hjertager [88], is an extension of the EBU to non-premixed combustion, where the reaction rate is limited by either the fuel, the oxidiser or chemical kinetics.

- Geometrical descriptions, like flame surface density models with flamelets stored in a library, are also possible. Here, the flame surface density is obtained from the turbulence and dissipation, and the reaction rates are then obtained from the flamelet library. There is an interlink between the flame surface density and the PDF of the mixture fraction Z and it has been used to study partially premixed flames [62], [128].

In summary, there are many models available, each tuned to different combustion processes. More general models are also available that feature fine resolution and large chemical mechanisms. Since these simulations are very costly, an own field of research is working on methods of extracting reduced mechanisms tuned to special cases from the large mechanisms for faster calculations without sacrificing precision [84, 83].

1.6 Heterogeneous reactions

A particle of solid fuel undergoes several distinct processes, which changes its chemical composition, if placed in a combustion environment. These changes are results of heterogeneous reactions, i.e. reactions between elements in different phases. Note that when a particle is losing mass due to any process, a resulting flow away from the particle is created, the so called *Stefan-flow* [50, 96]. This flow phenomenon has influence on the mass, momentum, species and energy transfer, as the medium through which species diffuse is moving away from the particle, and the no-slip condition that is usually assumed at the particles surface is no longer valid. The distinct processes a particle undergoes if placed in a combustion environment are described in the Subsections below.

1.6.1 Drying

Moisture that is present in the particle transforms into steam and is ejected from the particle. The simplest model assumes that all the moisture content is located on the particle surface, so that drying can be described like droplet evaporation [29]. A widely used model divides the particle in a growing outer dry shell and a shrinking wet core. Both shell and core are assumed as having uniform attributes, and between from core to shell and from shell to surrounding fluid are established [72]. An overview over methods to describe the drying of a particle can be found in [130]. A sketch of the drying process in depicted in the leftmost panel of Fig. 1.4, where heat is transported to the particle and vaporized moisture is ejected from it.

1.6.2 Devolatilization/Pyrolysis

Coal and biomass particles consist of complex molecules that crack when exposed to high heating rates and high temperatures. Cracking of these complex molecules yield gaseous or liquid molecules than can in turn react with the molecules inside of the particle or be ejected from it. This process is called devolatilization, or pyrolysis, if it takes place under an inert atmosphere [29]. The product gases or liquids of the process are highly dependent on the particle composition and the heating rate, and have been intensively studied. Usually, a higher heating rate results in a higher yield of volatile gases. Several approaches have been established for this process: Treating the process as a set of simple reactions [115], reactions with activation energies that follow a Gaussian distribution [7] and the most complex one; network models [42, 98]. Network models such as Chemical Percolation Devolatilization (CPD) calculate the products of the cracking and repolymerization of the large molecules that the particle consists of. They are the most expensive, yet also most precise. One way to reduce the computational cost is to fit the rates obtained from a network model calculation with one- or two-rate processes [127]. The values for the one- or two-rate processes have to be calculated a priori. Further information on devolatilization models can be found in the book of de Souza-Santos [29]. Devolatilization is shown in the middle panel of Fig. 1.4. Heat is transported to the particle, where it is used to break molecular bonds inside the particle, yielding smaller molecules that are gaseous or liquid. These molecules are then available for further reactions, or are ejected from the particle. For large particles, with diameters over 1 mm, drying and devolatilization can happen simultaneously [96].

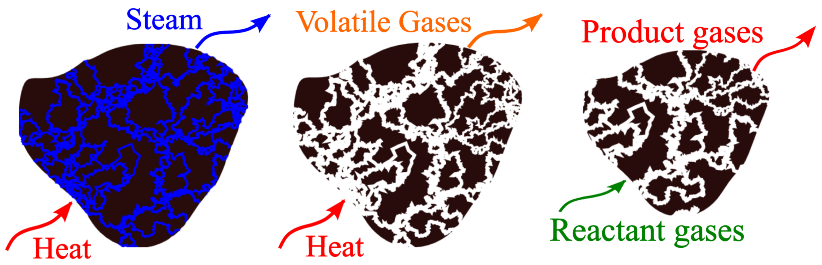

Figure 1.4: Coal combustion processes. From left to right: Drying, devolatilization/pyrolysis, combustion/gasification

1.6.3 Combustion/Gasification

Combustion or gasification occurs when biomass or coal particles are dried such that devolatilized and only large carbonaceous molecules remain. Combustion reactions are reactions where the gaseous reactant is oxygen (otherwise they are called gasification reactions). The earliest model that account for the transfer processes from the particle surface to the surrounding fluid is the so-called single-film model, where oxygen reacts with carbon to form carbon dioxide on the surface of the coal particle [100]. More elaborate is the model proposed by Burke and Schumann [22] assuming reaction of oxygen with carbon to carbon monoxide, which then reacts to carbon dioxide in the gas phase.

Even more comprehensive models taking into account the processes inside of the particle are also in use. Hecht et al. [59] describe char combustion as occuring on the surfaces of the micro pores penetrating the particle. Other models account for species adsorption/desorption, species diffusion along the pores, evolution of porosity and radius over time as well as different radiation models [55]. However, due to complexity, these models are only used to look at the combustion behaviour of one particle or a cloud of uniformly reacting particles.

1.7 Particle clustering and combustion regimes

Particles, when placed in a turbulent flow, tend to cluster in areas of high shear and low vorticity [32]. However, this ability is dependent on how well a particle can follow the flow around it [131], which is described by the Stokes number St. The dimensionless numbers used in this work are described in detail in Section 2.1. Particles preferably cluster due to vortices that have the same time scale as themselves. The fluid time scale can be based on any scale the study focuses on, from the smallest possible scale of the flow, the Kolmogorov scale η, to the most energetic scale, the integral scale. Particles with a Stokes number near zero follow the fluid volume they were initialized in (they are then called tracer particles), while particle with very high Stokes numbers are hardly influenced by the fluid flow. Figure 1.5 shows the pattern of particles in an evolving turbulent flow simulation starting from an initial random distribution. The particles have a Stokes number of one in relation to the most energetic fluid time scale. All panels of Fig. 1.5 show the particle position in one slice of the fluid domain. In the leftmost panel, the initial random positions of the particles are shown. The panel right to it shows the particles at later times, and the concentrating of particles at certain regions begins to be apparent. Also first voids, regions with no particles present, appear. The third panel from the left shows the particles at even later times, where the particles have gathered in distinct regions separated by regions void of any particles. The rightmost panel shows a photo of real particles subjected to turbulent air in microgravity [37], where the same structures appear. Describing the shape and size of these structures can be done with fractals [10], the statistical features of the preferential concentration [24], with Lyapunov exponents [36], Minkowski functionals [23], or by investigating the dynamics of the flow and the particles [54, 108]. A way to find the characteristic size of the clusters is to transform the particle number density field into spectral space and finding the wave number of the most energetic mode. The wavelength corresponding to this mode is the characteristic length scale of the clusters [108].

When particles cluster, more particles are affecting the same region of fluid. This profoundly changes the effects the particle can have on the fluid and vice versa. Annamalai and Ramalingam studied the combustion regimes as a function of the internal particle number density of coal particles [3]. They assumed a cloud of immobile particles situated in a frozen, quiescent cloud of gas and identified three combustion regimes:

- Individual Particle Combustion (IPC): For small particle number densities,

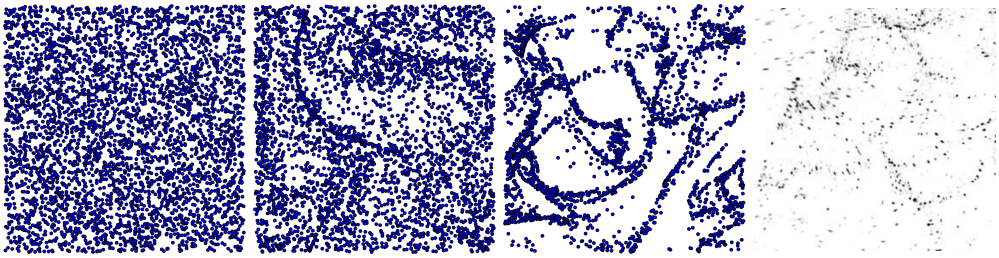

Figure 1.5: Particles cluster due to turbulent eddies. The time of the snapshots increases from left to right for the first three plots from the left. The rightmost figure is a photo of particles in turbulence and micro gravity taken from [37].

the interaction of particles can be neglected, and each particle react on its own. Fluid around the particle can be assumed as having the same attributes as the fluid far away from the particle cloud. The oxygen mass fraction as a function of the position in the particle cloud for this combustion regime is shown in the leftmost panel of Fig. 1.6.

- Group Combustion (GC): If the particle number density inside the cloud increases, oxygen inside the particle cloud is consumed faster than it can be replenished by transport from the fluid outside of the particle cloud. Over time, the oxygen mass fraction inside the particle cloud decreases. The oxygen mass fraction as a function of the position in the particle cloud in this regime can be seen in Fig. 1.7.

- Sheath Combustion (SC): For even higher particle number densities, the particles on the outer shell of the particle cloud consume all the oxygen that is transported to them from outside the particle cloud. After an initial period, where the internal particles consume the internal oxygen, they stop reacting since no oxygen is transported to them. This state is displayed in Fig. 1.8, where the oxygen mass fraction decreases already close to the particle cluster and no oxygen is present inside of it.

Reveillon and Demoulin [108] published a DNS study where they investigate the evaporation of droplets. Simulations are run where droplets of varying Stokes numbers (from 0.025 to 11) are placed in isotropic turbulence and allowed to cluster. After droplets and flow have reached dynamical equilibrium, drop evaporation is started. The saturation mass fraction of fuel depends on the temperature. Combustion is modeled by a one step Arrhenius law. To start the combustion process, a spherical ignition kernel is placed in the centre of the domain at ignition time.

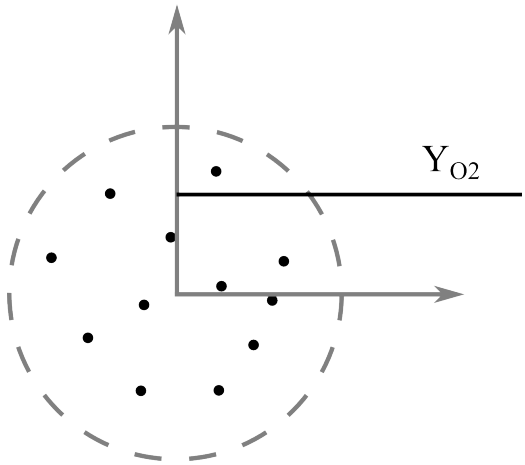

Figure 1.6: Oxygen mass fraction as a function position: IPC

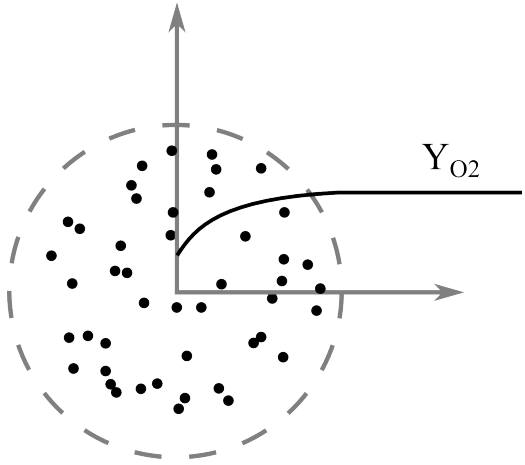

Figure 1.7: Oxygen mass fraction as a function position: GC

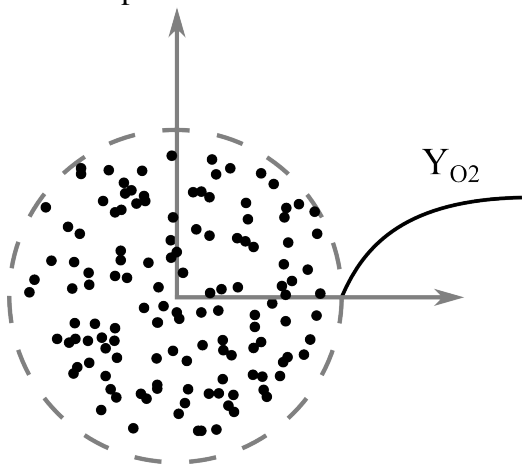

Figure 1.8: Oxygen mass fraction as a function position: SC

They report that the strongest clustering is found at a particle Stokes number of 1, with less clustering at lower or higher Stokes numbers. This is due to the fact that particles with lower Stokes numbers are still dispersed by small scale turbulence, while particles with large Stokes numbers are not entirely caught in the vortices. The evaporation rates are slower for highly clustered cases, with Stokes numbers around 1. This is due to the fact that when a lot of particles are close to each other, the combined evaporating gases are quickly increasing their local partial pressure to the saturation pressure, stopping further evaporation. This situation is comparable to the GC or SC regime. Subsequently, the case with high clustering shows a much higher range of mixture fractions. Since the droplets lose mass during evaporation, particles with an initial Stokes number higher than 1 eventually reach a Stokes number that makes them more suspectible to clustering. During the process of evaporation, a wide range of combustion regimes can be observed, ranging from premixed to partially premixed combustion. This study sheds some light on the connections of particle clustering and reaction rates, even though only homogeneous combustion is considered.

1.8 Recent studies on combustion of particulate matter

There is considerable research ongoing on all scales of coal and biomass combustion; single particle scale, lab scale and industrial scale. Single particles are studies where a single particle and its surrounding flow are resolved. This is done in order to study the connection of intra-particle processes on the particle-fluid interactions and vice versa. Moreover, the influence of particle internal properties such as porosity, pore diffusion, internal mass and heat transfer are studied. Before an overview over recent research efforts is given, one concept and one experimental setup are explained, since they feature heavily in recent works.

CRIEPI flame:

On the scale of laboratory systems (on the order of 0.1 to 1.0 m), the effects of turbulence and particle velocities and positions can be studied, while the small size allows for fast adaptation and relatively low cost of operation. Another topic of interest that can be investigated in flames of this size is the fine flame structure. This scale enables research groups to compare experimental results with simulations of the same system. As an example, the Central Research Institute

of Electric Power Industry (CRIEPI) flame [61] is a lab scale pulverized coal jet flame with flame stabilisation via a methane flame. By employing an array of different non-intrusive optical measurement techniques, particle diameters and velocities as well as flame temperatures and structures are known. This data, together with its simple geometry, makes the CRIEPI flame suited for numerical replication and comparison.

Flame index:

An important tool to classify the combustion regime is the Flame Index (FI) [132]. The FI is defined as

$$\mathrm{FI} = \nabla \mathrm{Y_{O_2}} \cdot \nabla \mathrm{Y_f}, \tag{1.1}$$

where Y_{O_2} is the oxygen mass fraction and Y_f the fuel mass fraction. A sketch of FI analysis is shown in Fig. 1.8. The arrows in this sketch point in directions of decreasing oxygen or fuel fractions. The concept of premixed and non-premixed combustion can be used in homogeneous combustion as well as in heterogeneous combustion. In the sketch, the particles in the case of heterogeneous combustion are releasing fuel into the fluid around them, so the fuel mass fraction decreases with increasing distance to the particle. The FI is positive if the gradients of the fuel and oxidiser fractions point in the same direction (their dot product is positive) and negative otherwise. A positive FI stands for premixed combustion and a negative for non-premixed. To connect the combustion modes to the particle combustion regimes, the non-premixed combustion is closer to the IPC, while premixed combustion is similar to GC.

1.8.1 Single particle studies of biomass and coal

Tufano et al. [123] investigated the early stages of single particle ignition and devolatilization of coal under different gaseous atmospheres, which shed light on the difference between air-fired and oxy-fuel combustion with recycled flue gas. The goal was to accurately replicate data from experiment [94] and compare ignition delays. They account for intra-particle and particle-gas heat transfer to accurately describe the particle heating rate and use a single kinetic rate for the devolatilization rate. They are able to combine the simplicity and low computational cost of the single kinetic rate with good predictive capabilities by fitting the kinetic rate to CPD data a priori. To speed up the homogeneous reaction calculations a skeletal mechanism tailor-made for this system from a much larger system

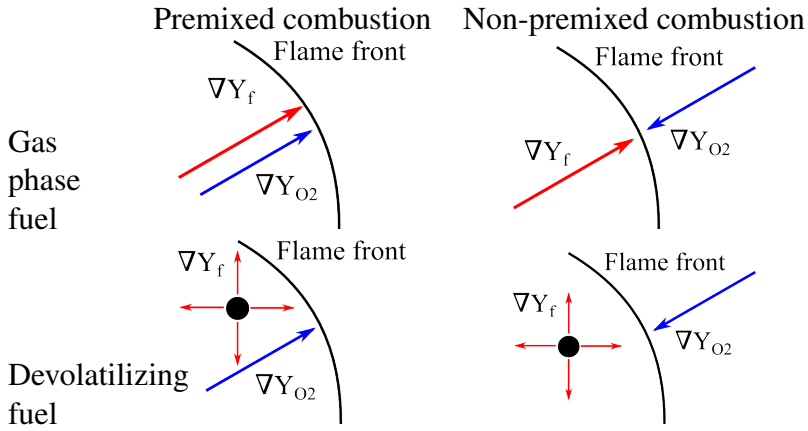

Figure 1.9: Combustion modes according to FI analysis. (Non-)premixed combustion is present when the gradients of fuel and oxygen point in the same (opposite) direction [19].

is used. They report good agreements with the experimental ignition delay times and they are able to predict the ignition delay times for coal combustion under different atmospheres.

A study focussing on the later stages of coal combustion and gasification is put forward by Nikrityuk et al. [97]. They numerically investigate the combustion of a single, dried, devolatilized char particle in air with different temperatures and steam mass fractions. Three homogeneous and three heterogeneous semi-global reactions are used in the study, and four different sets of rate coefficients for the heterogeneous reactions obtained for different coals are compared. The effects of heat, mass and species transfer as well as the Stefan flow and radiative heat transfer are included. It is found that different kinetic rates yield different particle consumption rates, even if the kinetic rates are obtained from quite similar coals. The differences decreased for higher gas temperatures and nearly disappeared for 3000 K, as the reactions become diffusion controlled. Reactions become diffusion controlled when the kinetic rates of the reaction are so fast (usually at high temperatures), that the rate of reaction is limited by the speed of which reactant species are transported to the particle surface. Also, the onset of the diffusion controlled regime is shifted to higher temperatures if the turbulence in the air flow is increased. This is thought to be due to the increase of the mass transfer to the particle surface.

1.8.2 Studies of lab-scale systems for biomass and coal combustion

For biomass, Elfasakhany et al. [34] investigate a biomass flame experimentally and with simulations, modelling particle anisotropy, rocket force, radiation, drying, devolatilization, combustion and turbulence modulation in a k-ε RANS simulation. The rocket force is the force due to the ejection of evaporated moisture or devolatilizing gases in a preferred direction [33]. Coal is usually nearly isotropic and gases are emitted in all directions, so little net acceleration is found. Biomass particles on the other hand have a preferential direction in their structure, and mass ejected in one direction accelerates the particle into the opposite direction. They show that the rocket force due to jets of boiling moisture or devolatilizing gases have a effect on the particle distribution, and that this effect is higher for larger particles. Going to the test scale, Ma et al. [87] investigated the combustion of wood fuel in an industrial furnace. They present a model for NO_x formation and potassium release, which achieves good agreement with experimental results. Moreover, it is reported that the particle shape has a significant effect on the particle trajectories. The same group also performed a simulation of a prototype scale 0.5 MW co-fired furnace and compared the results against experiments [86]. They found that while the majority of small biomass particles burn up rapidly, some of them burn slowly and then gather at the bottom of the furnace. It is important to note that accurate data on the specific heats of coal and biomass is required for different fuel types to achieve reliable results in all cases, which is critical for all numerical modelling of combustion systems.

A LES with detailed description of particle devolatilization by CPD and flamelet-based homogeneous chemistry of the CRIEPI flame has been published by Rieth et al. [109]. They compare this with earlier work [43, 118], where the devolatilization rate is found from empirical models with fitted and standard rate constants. Char combustion is taken into account by a single-film model, assuming direct oxidation of carbon to carbon monoxide [114], with subsequent further oxidation of carbon monoxide in the gas phase. However, the influence of carbon conversion models is quite low, since the residence time of the coal particles in the domain is short and the coal is not fully converted [92]. In this and other LES [118], good agreement of flow velocities and particle velocities with the experiment is found. Additionally, they report a high variance in the individual particle heating and devolatilization rates, but the direct employment of CPD can take account of this at reasonable computational cost without tuning. This approach

is thought to be of use in systems where a broad range of particle heat-up rates is found. However, the effect of turbulence on char combustion/gasification is not explicitly studied, as the CRIEPI flame's focus is rather on devolatilization reactions.

1.8.3 Industrial scale studies of biomass and coal combustion

Karampinis et al. [67] investigate the co-firing of cardoon (artichoke thistle [1]) in an industrial 300 MW lignite fuelled furnace using Ansys Fluent. Different co-firing rates and biomass particle sizes and their limits for acceptable NO_x levels are studied. Simulation results are compared with plant data for design point operation (without co-firing). Coal particles are assumed to be spherical with a mean diameter of 104 μm and 27 μm for two different coal fuel streams, respectively. Two different biomass diameters of 1 mm and 5 mm are investigated, with an aspect ratio of four. This corresponds to cylindrical particles and shows the significant differences in typical shape and size of coal and biomass fuels [31]. Gas phase combustion is modelled using the EDC with finite rates from a 2-step global mechanism. Equations governing the lignite and biomass motion, heat up and combustion are implemented using a User Defined Function (UDF). The non-sphericity of the biomass is accounted for by introduction of a shape factor. Both coal and biomass drag factors are then calculated using the implemented model in Fluent for spherical and non-spherical particles, respectively. The particles are inserted into the domain dried, and the amount of flue gas recirculation is calculated to match the energy required to dry the solid mass. Devolatilization is governed by a single rate model with different rate constants for coal and biomass respectively, and combustion is governed by two- and one-step kinetic/diffusion limited model, for coal and biomass respectively. For the non-spherical biomass particles, the reaction rate is sped up by a enhancement factor, taking into account the faster reaction of non-spherical particles in comparison to a spherical particle [44]. This additional modelling required to account for large particle sizes and irregular shapes highlights the increased complexity of biomass combustion in comparison to coal. Thermal and fuel NO_x formation is studied, prompt NO_x is neglected due to the fuel lean conditions in the furnace. Fuel NO_x is modelled by assuming intermediate nitrogen species released during devolatilization, and char bound nitrogen that forms NO directly via a surface reaction [81, 5]. The composition of the intermediate nitrogen species from devolatilizing are different for biomass and coal. Good agreement between measurements and simulations

is found for the heat flux and composition of flue gases. The mass flow is decreased, while the outlet temperature is increased during co-firing, which results in a nearly unaffected heat flux. A 10% decrease in NO_x emissions is reported, which is assumed to be due to the lower fuel bound nitrogen of biomass. Moreover, the intermediate nitrogen compound which is mainly released by biomass has a lower conversion ratio to NO than the nitrogen compound mostly released by coal. This trend of decreased NO_x emissions is reported to be in accordance with published data, but failed to materialize during the co-firing campaign of the furnace in question. A short duration and varying load during the co-firing campaign are given as reasons for this discrepancy. Regarding the influence of the biomass particle size, large biomass particles are found to exit the furnace via the hopper with low burnout, increasing hopper losses. These particles mostly entered the furnace through burners located farther down in the burner. Small biomass particles achieve high burnouts. The authors recommend milling the biomass particles to small sizes or inserting the particles via a distinct feeding system located in the middle section of the furnace. Via simulations, recommendations for upgrade of an existing system can be made that would have been much more costly if investigated with experiments.

Choi and Kim [26] studied an industrial 500 MW pulverized coal furnace using RANS with Re-Normalisation Group (RNG) k-ε as the turbulence closure. The effect of the turbulent flow on the particle trajectories is accounted for by stochastic tracking, where the particles are displaced in random directions with a magnitude that depends on the local turbulence intensity [5]. Devolatilization is modelled by a two competing rate model and char combustion by a kinetic/diffusion limited model of Baum and Street [9]. Gas phase combustion is modelled by solving for the mixture fraction. The influence of turbulence on the chemistry is accounted for by a presumed β-PDF. The goal of this study was to investigate the effect of air staging on the NO_x emission, and the NO_x emissions are calculated as a post-processing step, assuming that NO_x has negligible effect on the combustion itself. They report good agreement between the simulation and measurements on such global values as total heat flux to the furnace walls, temperatures and species concentrations at the furnace exit. Furthermore, it is shown that air staging can reduce the forming of thermal NO_x, due to the reduced temperature. This work is an example for the use of simulation tools in the improvement of control or design of an industrial scale furnace. It also highlights a possibility where the research of the present thesis can be of use. The kinetic/diffusion limited model of Baum and Street implemented into Ansys

Fluent does not take into account turbulent clustering on the char conversion rate. The work conducted in this thesis aims to provide a model that can account for this effect for RANS and coarse LES.

1.8.4 DNS studies

Luo et al. [85] performed a study of the CRIEPI flame at a Reynolds number of 28,000 and with homogeneous and heterogeneous reactions. Fluid-particle transfers are evaluated for momentum, mass, species and energy. The particle is accelerated by gravity and drag. Particle drying is modelled akin to a droplet evaporation model, and devolatilization is described by a competing rate model, where the volatile species is assumed to be CH_4 to reduce computational cost. Coal combustion is then modelled using a three-step global mechanism. Particles are treated as point particles and the number of grid cells in the domain is around 700 million. Gas phase combustion is modelled by a two-step global mechanism [112]. The radiation heat transfer between particle and gas is modelled by a simple radiation model between the particle and the mean temperature of the surrounding gas.

They find qualitative agreement with experiments for the particle mean and rms velocity, and that particles with a smaller diameter have a larger radial distance to the jet centreline that larger ones. This may be due to the ability of small (and light) particles to follow vortices easier than large, heavy ones. Moreover vortex rings are created around the jet, and as these vortex rings travel downstream and begin to become skewed, particles aggregate around them. In the upstream region close to the burner nozzle, only singular particles are reacting in the IPC regime, while the majority of the particles in the jet are not yet reacting. Further downstream, particle dispersion and turbulence has mixed oxidiser and particles, and large groups of particles are burning together in a GC regime. To gain insight into the connections between the mixture fraction, temperature and mass fraction, conditional means and averages of the temperature and heat release rates with respect to the mixture fraction are analysed. It is found that the heat release rate in the downstream region has two peaks, which is explained as being due to the heat release having two possible sources: homogeneous combustion where the mixture fraction in the gas phase is close to its stoichiometric value, and on the fuel rich side where char combustion takes place. When studying the distribution of the particle number density as a function of the axial distance from the nozzle, a zone with deceleration and subsequent dispersion is found. As in

the LES study of Rieth et al. [109], char conversion is low due to the insufficient length of the domain. So, while char combustion is taken into account, the combustion process is only studied at its beginning, where devolatilization and homogeneous combustion processes dominate.

A DNS study of the influence of the fuel equivalence ratio in gas and particulate phase and turbulent fluctuations on the ignition process of a coal particle laden mixture is performed by Brosh and Chakraborty [19]. For the gas phase and particle phase equations, as well as devolatilization and gas phase combustion modelling the same approach as used in Luo et al. [85] is chosen. The rate coefficients for the homogeneous reaction mechanism are calibrated to yield a realistic laminar unstrained burning velocity. The general models for particle heat transfer, combustion and devolatilization as well as the ones for gas phase combustion are similar to the study of Luo et al., but here, the particles are assumed to be pre-heated and dried. To study ignition behaviour of turbulent particle laden mixtures, a range of turbulence fluctuation velocities are analysed. Additionally, the amount of gaseous volatiles and the amount of particles (containing volatiles) are varied. An ignition kernel is placed in the centre of the domain and the ensuing temperature changes, devolatilization rates and reaction rates are studied.

If the particles have volatile content, the mixture burns in the non-premixed mode for laminar flows, but the premixed mode of combustion is stronger for turbulent flows due to turbulent mixing. Moreover, it is reported that too high turbulent velocities transport too much energy away from the ignition kernel, so that no sustained combustion follows ignition. For cases with a low fuel content in the particle phase, the fuel content in the gas phase has no big influence on the sustained combustion. However, for fuel-rich particles, a high gaseous fuel load decreases the chance of sustained combustion, as the mixture becomes too fuel rich. Again, the early stages of combustion are studied, where devolatilization and the combustion of devolatilized gases are the primary processes.

An investigation of the CRIEPI pulverized coal jet flame is performed numerically by Hara et al. [52]. The goal of the study is to find a simple global homogeneous reaction mechanism that is able to describe the combustion of volatile matter of varying composition, so that the use of different coal types can be simulated. They propose a two-step global reaction scheme validated against data of the laminar flame speed and burned gas temperature of a detailed reaction scheme. Additionally, the physical and chemical properties of the devolatilized gas are fitted to yield good approximations for different coals and heating rates. The reaction rates are adapted to take into account effects of equivalence ratio, pressure,

temperature and dilution by CO_2 and H_2O. With the extended global reaction scheme, they are able to reproduce the laminar flame speed for different coals, temperatures and pressures. Particles are inserted with a varying diameter but constant density. For particle motion, the Stokes drag with the Schiller-Naumann correlation for low and intermediate Reynolds numbers [111] and for heat transfer the Ranz-Marschall correlation with a Stefan flow extension [50, 102] is used. Gravity is neglected. The diameter of the coal particles is assumed to be constant during the combustion process. Combustion of the carbon fixed in the char is governed by the model proposed by Field [41], taking into account the reaction as well the diffusion rate of oxygen to the particle surface.

The streamwise motion of the coal particles on the central axis agrees well with the data obtained from experiments [61]. Regarding the streamwise particle velocities depending on their radial position on two axial positions, lower values than found in the experiment are reported. A possible explanation is that the additional air from the pulverized coal feeder is not accounted for correctly. Another reason for discrepancies between the experimental and numerical data is that gravity's influence on the particles is neglected in the simulations. Comparisons between simulated and measured gas and particle temperatures are presented, and the simulated particle temperatures are found to be higher than the ones measured. This discrepancy is thought to be due to the measurement method that cannot reliably distinguish between particle, gas and soot radiation. The O_2 and CO_2 levels reported for the simulation are closer to the measured ones than for a LES study of the same system [43], but also here some of the discrepancies are reckoned to be due to low spatial resolution of the measurement method. Particle clustering is reported to happen mostly when each particles Stokes number is around unity, which happens upstream for smaller and further downstream for larger particles, as they lose mass. Additionally, combustion behaviour is analysed by means of the FI (as in the study of Brosh and Chakraborty in Section 1.8.4). A negative FI, implying non-premixed combustion is reported for the outer flame layer, while premixed combustion is found in the inner flame layer, close to the particle position. Even closer to the central axis, a diffusion regime is identified by the FI, but closer examination reveals that the release of devolatilized gases overpowers the consumption by the actual pre-mixed combustion. This turns the gradient of fuel fraction, making the FI negative. Concluding, the simple reaction mechanism is able to correctly predict combustion behaviour for a wide range of conditions, and DNS is able to predict a lab-scale pulverized coal jet flame, making it a good tool to further study PCC systems.

Chapter 2

Theory

In order to understand the different combustion and particle regimes, it is helpful to define a range of dimensionless numbers. These dimensionless numbers are helpful to identify which physical processes are dominant in a system. The basic dimensionless numbers that are used to describe turbulent combustion systems and their subprocesses are introduced in Section 2.1.

In Section 2.2 the equations are given for the flow system that treats the heterogeneous reactions as a consumption of a passive reactant. The passive reactant is convected and diffused by the flow, but is only consumed at the particles surface. The reactant does not interact with the fluid or particles in any other way. This system is examined and presented in Papers 1 and 2 (Section 5.1 and 5.2), while a slightly more advanced system is studied in Paper 4 5.4. Subsequently, the equations used to describe a flow system with more realistic chemistry are given in Section 2.3. The studies involving the more realistic chemistry are used for Paper 5 which is presented in Section 5.5. Moreover, at the end of the chapter in Subsection 2.3.3, the equations governing particle combustion with adsorbed species are introduced. These equations are part of the ”Stanford Code” [55] and are as part of the present work implemented into ”The Pencil Code”. No studies have been performed with them in junction with solid fuel combustion in a DNS framework. The ”Stanford Code” has been used for studies published in Paper 3, which is found in Section 5.3.

2.1 Dimensionless numbers

Reynolds number:

The Reynolds number is the ratio between the convective and the viscous force and defined as

$$\mathrm{Re} = \frac{\boldsymbol{u}L}{\nu}, \tag{2.1}$$

where $\boldsymbol{u}$ is a velocity, L a typical lenght scale, and ν the dynamic viscosity. The numerator stands for the chaotic, inertial forces, the denominator for the damping, viscous forces. When the Reynolds number is low, a flow is smooth. Opposed to this, at high Reynolds numbers, the flow is dominated by vortices and generally unstable.

Sherwood and Nusselt number:

The Sherwood number is the ratio between the convective and diffusive mass transfer

$$\mathrm{Sh} = \frac{kL}{D}, \tag{2.2}$$

where k is the convective mass transfer rate and D the diffusion coefficient. The used correlation for the Sherwood number is Eq. 2.22 in Subsection 2.2.2. In analogy, the Nusselt number is the ratio between the convective and conductive heat transfer

$$\mathrm{Nu} = \frac{HL}{k_g}, \tag{2.3}$$

where H is the heat transfer coefficient and k_g the conductivity. A Nusselt number correlation is found in Eq. 2.54 in Subsection 2.3.2.

Stokes number:

The Stokes number is defined as the ratio between the stopping time of a particle, which depends on the inertia of a particle in its surrounding flow, and a typical flow time scale:

$$\mathrm{St} = \frac{\tau_p}{\tau_f}. \tag{2.4}$$

Here τ_p is the *particle stopping time* and τ_f a relevant *fluid time scale*, such as the time one vortex in the flow needs to fulfill one rotation. Particles with a low Stokes number are able to follow the motion of their surrounding fluid very precisely, while the trajectory of particles with a high Stokes number is much less influenced by fluid movements. Note that the flow time scale can be defined to have a broad range of values, and particles that have a high Stokes number in respect to very small flow scales (with small time scales) have a low Stokes number in respect to large flow scales.

Damköhler number:

The Damköhler number is used to compare the speed of chemical reactions with the speed of turbulent mass transfer. In the present work, it is evaluated as

$$\mathrm{Da} = \frac{\tau_f}{\tau_c}, \tag{2.5}$$

where τ_c is a chemical time scale. If the Damköhler number is high, chemical reactions are much faster than the transport processes. Reactions are then proceeding in a non-premixed regime. For low Damköhler numbers, transport rates of species in a flow are faster than the chemical reaction potentially consuming species, and the combustion regime can be described as being well mixed or premixed.

For a description of the chemical time scales for homogeneous combustion, both non-premixed and premixed, the reader is reffered to the book of Poinsot and Vervisch [104].

In the current analysis, the chemical time scale is constructed from a reaction rate,

$$\alpha_c = \overline{n}_p \overline{A}_p k_{eff}, \tag{2.6}$$

where $\overline{n}_p$ is the mean number density of particles in the domain, $\overline{A}_p$ the mean particle surface and k_{eff} a reaction rate. The reaction rate is the available reactive surface area per volume multiplied with the reaction speed. The chemical time scale is then found with

$$\tau_c = \frac{1}{\alpha_c}. \tag{2.7}$$

2.2 Passive scalar studies

2.2.1 Fluid equations

Mass conservation:

For the passive scalar studies, the flow that is simulated is isothermal, yet compressible. To obtain a flow system that is homogeneous and isotropic, gravity is neglected and the boundaries of the domain are periodic. The equation of the conservation of mass is:

$$\frac{\mathrm{D}\rho}{\mathrm{D}t} = -\rho\nabla\cdot\boldsymbol{u}, \tag{2.8}$$

where the advective derivative is

$$\frac{\mathrm{D}}{\mathrm{D}t} = \frac{\partial}{\partial t} + \boldsymbol{u}\cdot\nabla. \tag{2.9}$$

Here, ρ is the density of the fluid and t time. The operator $\nabla = \frac{\partial}{\partial x} + \frac{\partial}{\partial y} + \frac{\partial}{\partial z}$ that appears in the second term on the Right Hand Side (RHS) is the gradient of a function in three Cartesian coordinates x, y and z.

Momentum conservation:

The equation of conservation of momentum of one fluid element is:

$$\rho\frac{\mathrm{D}\boldsymbol{u}}{\mathrm{D}t} = -\nabla p + \nabla\cdot(2\mu\boldsymbol{S}) + \rho\boldsymbol{f} + \boldsymbol{F}, \tag{2.10}$$

where viscous effects are accounted for by the traceless rate of strain

$$\boldsymbol{S} = \frac{1}{2}\left(\nabla\boldsymbol{u} + (\nabla\boldsymbol{u})^T\right) - \frac{1}{3}\delta_{ij}\nabla\cdot\boldsymbol{u}, \tag{2.11}$$

and the dynamic viscosity μ. The symbol δ_{ij} in the second term on the RHS is the Kronecker delta, which is 1 if $i = j$, and 0 otherwise. The pressure is calculated from the isothermal sound speed and density: $p = c_s^2\rho$. The term $\boldsymbol{f}$ accounts for volumetric forces like gravity, but in this study, was used to produce isotropic, homogeneous turbulence. The forcing function used is taken from Brandenburgs study [15], which was already employed in a study on hydrogen combustion of Babkovskaia et al. [8]. The function forces the flow every time step in a random direction in the plane perpendicular to a random wave vector which is shorter

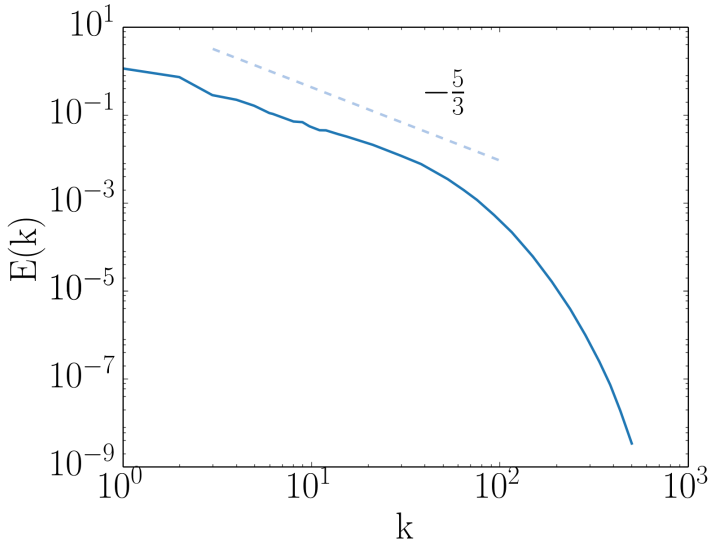

Figure 2.1: Power spectrum the kinetic energy of wave number k of a simulation with turbulent forcing and a grid cell number of 1024^3.

than the length of the domain. The length of the wave vector is also the length of the most energy rich scale of the flow, the integral scale L.

The term $\boldsymbol{F}$ accounts for the back reaction of the particle drag on the fluid. Two way coupling of heavy particles can enhance production or dissipation of turbulence, depending on the ratio of the particle stopping time and the flow time scale, as well as the mass loading. The study of turbulence and particles is a very active field of research [46, 117, 35, 39], and the use of two-way coupling with forced turbulence is discouraged. To obtain knowledge of the turbulence-particle interaction, they recommend use of decaying turbulence. However, since the dynamic particle-turbulence interaction is not the focus of the thesis and a statistical steady state is required, continuous forcing with two-way coupling is used. The turbulent energy spectrum is modulated by the turbulence, in accordance with the findings of [48]. Figure 2.1 shows the power spectrum of kinetic energy as a function of the wave number k for a simulation of with a cell number of 1024^3. The $-5/3$ gradient of the inertial range (dashed line) is evident. The energy rich integral scale is visible as the flat top of the power spectrum in the upper left corner of each plot. Also visible is the faster dissipation of energy in the dissipation range at higher wave numbers.

Passive reactant:

A simplified system to study reactions, mixing, diffusion or conversion processes include the use of the passive scalars [40]. A passive scalar is a variable that is transported and diffused by the flow field, but has no influence on the properties of the flow otherwise. To study heterogeneous reactions, the passive scalar is assumed to be consumed at the surface of particles present in the flow. Since this process can be compared to catalytic conversion or the passive scalar being interpreted as a reactant for a isothermal, unimolar reaction, the term ”passive reactant” is used from now on. The convection-diffusion equation of the molar fraction of the passive reactant X, with a consumption term at the particles surface, is given by:

$$\frac{\mathrm{D}X}{\mathrm{D}t} = -D\nabla^2 X + \widehat{R}_{pass}, \tag{2.12}$$

with D being the diffusivity of the passive reactant and $\widehat{R}_{pass}$ the sink term due to the conversion of the reactant at the particles surface. Note that there is no dissipation term in this formula. The only way the total amount of passive reactant in the computational domain can change is via particle dependent reactions. This method is a stable, computationally effective method to study heterogeneous reactions in a turbulent flow field.

2.2.2 Particle equations

The particles in the passive reactant studies are much smaller than the grid size and much denser than the fluid. Therefore, the only force acting on the particle is the Stokes drag [28]. Gravity forces are, as for the fluid, neglected. The particles are tracked in a Lagrangian manner, and since the volume fraction of the particles in the flow is dilute, no particle-particle interaction is modelled.

Speed and position:

The velocity $\boldsymbol{v}$ of one particle is evolved as:

$$\frac{d\boldsymbol{v}}{dt} = \frac{1}{\tau_p}(\boldsymbol{u} - \boldsymbol{v}) = \frac{\boldsymbol{F}}{m_p}, \tag{2.13}$$

with the particle stopping time given as $\tau_p = \rho_p d_p^2/18\mu(1 + f_c)$ when $f_c = 0.15\mathrm{Re}_p^{0.687}$ is due to the Schiller-Naumann correlation [111] which extends the

applicability of this model to particle Reynolds numbers of up to 800. The particle Reynolds number is given by

$$\mathrm{Re}_p = \frac{|\boldsymbol{u} - \boldsymbol{v}| d_p \rho}{\mu}, \tag{2.14}$$

where d_p is the particle diameter, μ the dynamic viscosity of the fluid and ρ the fluid density. The particles density is given by ρ_p, and m_p is the particles mass. The drag force $\boldsymbol{F}$ is the one inserted into Eq. 2.10 in Subsection 2.2.1. The particle position $\mathbf{X}$ is then found by:

$$\frac{d\mathbf{X}}{dt} = \boldsymbol{v} \tag{2.15}$$

Particle specific consumption rate:

The reactant that is carried by the fluid phase is converted at the particle surface at a rate of

$$\widehat{R}_{pass} = \frac{A_p k_{kin} X_s}{V_{cell}}, \tag{2.16}$$

where A_p is the particles surface area, X_s the passive reactant molar fraction at the particle surface, k_{kin} the kinetic reaction rate and V_{cell} the volume of the grid cell. By assuming equilibrium between diffusive transport and passive reactant consumption at the particles surface it is possible to express the X_s as a function of the molar fraction X_∞ in the grid cell:

$$\underbrace{k_{kin} X_s}_{Reactant\ consumption} = \underbrace{k_{diff}(X_\infty - X_s)}_{Diffusion}. \tag{2.17}$$

Solving for X_s yields:

$$X_s = \frac{k_{diff} X_\infty}{k_{kin} + k_{diff}}. \tag{2.18}$$

Inserting Eq. 2.18 in Eq. 2.16 gives:

$$\widehat{R}_{pass} = \frac{A_p k_{eff} X_\infty}{V_{cell}}, \tag{2.19}$$

where

$$k_{eff} = (k_{kin}k_{diff})/(k_{kin} + k_{diff}) \tag{2.20}$$

is the effective reaction rate after the ideas of Baum and Street [9]. The mass transfer coefficient is here given by

$$k_{diff} = \frac{D\mathrm{Sh}}{d_p}, \tag{2.21}$$

where Sh is the Sherwood coefficient. The Sherwood coefficient is taken from the Ranz-Marshall correlation and is:

$$\mathrm{Sh} = 2 + 0.69\mathrm{Re}_p^{0.5}\mathrm{Sc}^{0.33}, \tag{2.22}$$

with the Schmidt number being $\mathrm{Sc} = \mu/\rho D$. The Sherwood coefficient was set to two, assuming quiescent fluid immediately around the particle, for Papers 1 and 2, and was calculated with Eq. 2.22 for Papers 4 and 5. An example of how the particles consume passive reactant is shown in the left panel of Fig. 2.2, where the fraction of passive reactant is shown for a slice of the domain for an example simulation. Dark areas have a low content of passive reactant, light areas still have high fractions of passive reactant. The position of particles in this slice is shown in the right panel and aligns exactly with the regions of low passive reactant fraction. The kinetic reaction rate k_{kin}, as well as the passive scalar diffusivity D are parameters set on startup, and are unchanged during the simulation.

2.3 Chemistry studies

To study more realistic heterogeneous reactions, ”The Pencil Code” has been extended to model more realistic homogeneous and heterogeneous reactions and their effect on the flow. While the fluid in the passive reactant case was not affected by the conversion of the reactant, the mass, species, momentum and energy transfer from and to the fluid will in reality change the nature of the flow. These changing properties of the flow have to be taken into account since their impact on the connection between turbulence and heterogeneous reaction rates is unknown. The extension to account for homogeneous and heterogeneous chemistry comes with increasing computational cost, due to the need to store and evolve more

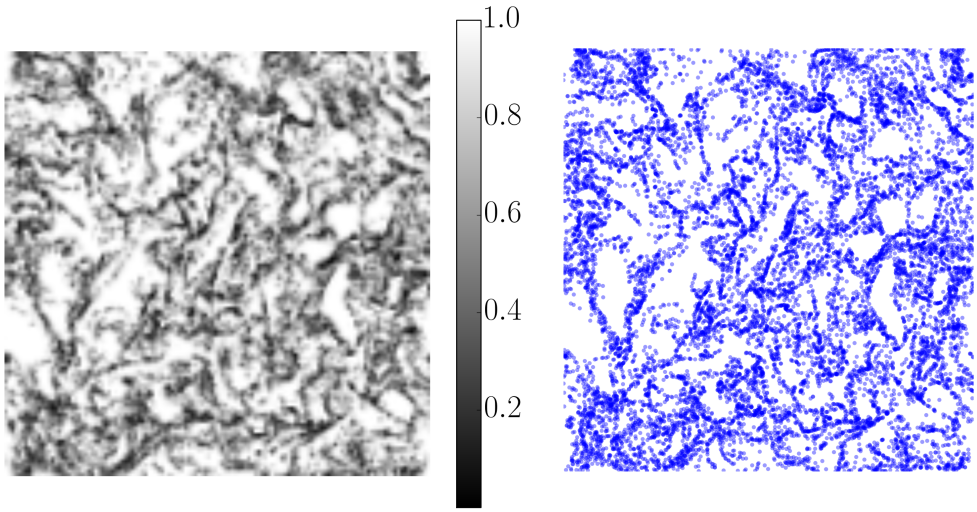

Figure 2.2: Sketch of the fraction of passive reactant in a slice of the domain (left). Dark areas have a low content of passive reactant, light areas a high one. The position of particles (right) exactly aligns with regions of low passive reactant content.

chemical and physical properties of the flow and particles. Moreover, some of the transfer effects, such as mass transfer from particle to fluid phase, adversely affect the numerical stability of the simulations. Some of the methods that are applied to increase numerical stability and computational speed are described in Section 2.4.

2.3.1 Fluid equations

Mass conservation:

As in the simulation of the passive reactant, the continuity equation is solved in the form

$$\frac{\mathrm{D}\rho}{\mathrm{D}t} = -\rho\boldsymbol{\nabla}\cdot\boldsymbol{u} + S_\rho, \tag{2.23}$$

where $\mathrm{D}/\mathrm{D}t = \partial/\partial t + \boldsymbol{u}\cdot\nabla$ is the advective derivative, ρ is the density, $\boldsymbol{u}$ is the velocity and

$$S_\rho = \frac{-1}{V_{\text{cell}}}\sum_{i}^{N_{particles}}\frac{dm_{p,i}}{dt} \tag{2.24}$$

is the mass source term due to mass transfer from the particles to the fluid. In the above equation $m_{p,i}$ represent the mass of particle number i, V_{cell} is the volume of the grid cell and the summation is over all particles i in the grid cell, $N_{particles}$.

Momentum conservation:

The momentum equation is written in the form

$$\rho \frac{\mathrm{D}\boldsymbol{u}}{\mathrm{D}t} = -\nabla p + \nabla \cdot (2\mu \boldsymbol{S}) + \rho \boldsymbol{f} + S_{m,p} + \boldsymbol{F}, \tag{2.25}$$

where the term

$$S_{m,p} = \frac{1}{V_{\text{cell}}} \sum_{i}^{N_{particles}} \frac{dm_{p,i}}{dt}(\boldsymbol{u} - \boldsymbol{v}_i) \tag{2.26}$$

accounts for the momentum that is transferred to the fluid by the mass that is transferred from the particle with velocity $\boldsymbol{v}$ to the fluid velocity $\boldsymbol{u}$. Note that $\frac{dm_{p,i}}{dt}$ is negative when the particle is losing mass.

Species conservation:

The equation for the mass fractions of each species is

$$\rho \frac{\mathrm{D}Y_k}{\mathrm{D}t} = -\nabla \cdot \boldsymbol{J}_k + \dot{\omega}_k + S_{y,k}, \tag{2.27}$$

where Y is the mass fraction, $\boldsymbol{J}$ is the diffusive flux, $\dot{\omega}_k$ is the source term due to gas phase reactions, subscript k refers to species number k and

$$S_{y,k} = \frac{1}{V_{\text{cell}}} \sum_{i}^{N_{particles}} \left(\dot{W}_{k,i} + Y_k \frac{dm_{p,i}}{dt} \right) \tag{2.28}$$

is due to gas phase species being products or reactants in the heterogeneous reactions. Here $\dot{W}_k$ is the species mass production rate (mass per time per particle) of gas phase species k due to heterogeneous reactions, which will be described in Eq. 2.41 in Subsection 2.3.2. Please note that the term $dm_{p,i}/dt$ is the change in particle mass given by Eq. 2.40. The diffusive flux of species k is given by

$$\boldsymbol{J}_k = \rho Y_k \boldsymbol{V}_k \tag{2.29}$$

when $\boldsymbol{V}_k$ is the diffusive velocity of species k.

Energy conservation:

The energy equation is

$$c_v \frac{\mathrm{D} \ln T_{gas}}{\mathrm{D}t} = \sum_{k}^{N_{species}} (-\nabla \cdot \boldsymbol{J}_k + \dot{\omega}_k) \left(\frac{R}{\overline{M}_k} - \frac{h_{s,k}}{T_{gas}} \right) - \frac{R}{\overline{M}_k} \nabla \cdot \boldsymbol{u} + \frac{2\nu \boldsymbol{S}^2}{T_{gas}} - \frac{\nabla \cdot \boldsymbol{q}}{\rho T_{gas}} + S_{T,conv} + S_{enth}, \tag{2.30}$$

where T_{gas} is the fluid temperature, c_v is the heat capacity at constant volume, R is the universal gas constant, $h_{s,k}$ is the sensible enthalpy, $\overline{M}_k$ is the molar mass and $\boldsymbol{q}$ is the heat flux

$$\boldsymbol{q} = \sum_{k}^{N_{species}} h_k \boldsymbol{J}_k - k_g \nabla T_{gas}. \tag{2.31}$$

Here, $h_k = h_{s,k} + \Delta h^0_{f,k}$ is the enthalpy of species k and $\Delta h^0_{f,k}$ is the heat of formation of species k. The heat conductivity is given by k_g. In the above equation, the sum of the conductive and convective heat transfer from the particles to the gas is given by

$$S_{T,conv} = \frac{1}{\rho T_{gas}} \frac{1}{V_{\text{cell}}} \sum_{i}^{N_{particles}} Q_{c,i}. \tag{2.32}$$

The term Q_{ci} is the convective heat transfer from particle to fluid which is described in Eq. 2.52 in Subsection 2.3.2. The term S_{enth} in Eq. 2.30 is the transport of enthalpy via mass transfer from the particle to the fluid. It is described in Eq. 2.57 as part of the description of the particle equations in Subsection 2.3.2.

Homogeneous reactions:

Each grid cell is assumed to be a Perfectly Stirred Reactor (PSR), where the reaction rates can be found directly from the kinetic reaction rates, the molar fraction and the molar gas concentrations $C_g = p/RT_{gas}$ of the reactant species. The rate of one reaction $\widehat{R}_{hom,j}$ can be found as:

$$\widehat{R}_{hom,j} = k^+_{kin,g,j} \prod_{k}^{N_{species}} (X_k C_g)^{\nu'_{j,k}} - k^-_{kin,g,j} \prod_{k}^{N_{species}} (X_k C_g)^{\nu''_{j,k}}, \tag{2.33}$$

where $k^+_{kin,g}$ and $k^-_{kin,g}$ are the forward and reverse reaction rates in the gas phase, respectively. The production rate of species $\dot{\omega}_k$ is now found as:

$$\dot{\omega}_k = \overline{M}_k \sum_{j}^{N_{reactions}} (\upsilon''_{j,k} - \upsilon'_{j,k}) \widehat{R}_{hom,j} \tag{2.34}$$

In this equation, $\overline{M}_k$ stands for the molar mass of species k, $\upsilon''_{j,k}$ and $\upsilon'_{j,k}$ are the stochiometric coefficients of the species for the product and reactant side respectively.

Forward and reverse reaction rate:

The kinetic rate of the reaction $k^+_{kin,g}$ is given by the Arrhenius expression

$$k^+_{kin,g,j} = B_j T^{\alpha_j}_{gas} \exp\left(\frac{-E_j}{RT_{gas}}\right), \tag{2.35}$$

where B_j is the pre-exponential factor, α_j is the temperature exponent, and E_j is the activation energy, which is given by a chemical mechansism. The reverse reaction rate $k^-_{kin,g,j}$ is calculated with the equilibrium constant $K_{eq,j}$:

$$K_{eq,j} = \frac{k^+_{kin,g,j}}{k^-_{kin,g,j}}, \tag{2.36}$$

where $K_{eq,j}$ is:

$$K_{eq,j} = \exp\left(\frac{\Delta S^0_j}{R} - \frac{\Delta H^0_j}{RT_{gas}}\right)\left(\frac{p}{RT_{gas}}\right)^{\Delta N_{gas,j}}. \tag{2.37}$$

The term in the first set of parentheses on the RHS represents $-\Delta G^0_j/RT_{gas}$, where ΔG^0_j is the change of Gibbs free energy over the reaction [68]. The change in Gibbs free energy is a measure of the thermodynamic potential that a system tries to minimize. In essence, endothermic processes are favoured at higher temperatures, while exothermic ones are favoured at lower temperatures. The term in the second parentheses accounts for the change in gas phase moles over the reaction and introduces a pressure dependence on the equilibrium. This is important since the simulation system has a fixed volume, so changing the number of gaseous molecules in the domain has an influence on the pressure. The change in gas

molecules over the reaction $\Delta N_{gas,j}$ is:

$$\Delta N_{gas,j} = \sum_{k}^{N_{species}} \upsilon''_{j,k} - \upsilon'_{j,k}. \tag{2.38}$$

Implemented reaction types:
The homogeneous reaction module of "The Pencil code" is compatible with all reaction types that are present in the mechanism GRI-Mech 3.0 [113]. The GRI-Mech 3.0 is a widely used and heavily optimized flame mechanism for propane flames. It is fitted to experimental targets such as ignition delay, species profiles and laminar flame speeds and is constantly updated. The reaction types that are implemented into the homogeneous reaction module of "The Pencil Code" are:

- Non-reversible reactions
- Reversible reactions
- Third body reactions
- Reactions of arbitrary reaction order
- Pressure dependent reactions with low and high pressure limits
- The TROE falloff form

The different reactions types are necessary to describe reactions that are global or detailed. Falloff reactions are reactions that need a third body to proceed for low pressures, but not for high pressures. Information about the calculation of the reaction rate for the different reaction types, please consider the CHEMKIN manual [68].

2.3.2 Particle equations

In this work, the particles are regarded as point particles, displacing no volume of the fluid, which is valid for particles much smaller than the grid resolution. This approach was chosen as the goal was to conduct DNS studies with a large number of particles. Moreover, intra-particle transfers are neglected, greatly saving on computational cost. Although the number of particles simulated was quite high, the small volume of each particle meant that particle-particle interaction could also be neglected. While there are studies where the particles are resolved, their

prohibitive computational cost restricts the simulated scale to very small systems [30, 125]. However, knowledge gained from studying the small scales can be used to create closure models for large scale models.

Speed and position:

The speed and position of the particles is evolved as the passive scalar studies in section 2.2.2. Due to the implemented large density ratio and neglected gravity, the particles are only accelerated according to the Stokes drag. A Ranz-Marshall correlation is used to account for the effect of low to intermediate slip velocities on the drag coefficient.

Particle mass loss and reaction rate, global mechanism:

The current particle reaction model assumes the combustion of dried, devolatilized char. While all studies in Subsection 1.8.4 use a particle combustion model, they focus on the phenomena early in the combustion, where devolatilization processes and homogeneous combustion of volatiles dominate. The particles are usually leaving the domain with a large part of their fixed char unreacted. It was the goal to shed some light on the processes that happen after the particles have dried and devolatilized. The particles are assumed to be spherical, and reactions happen only at the surface. This assumption is mostly valid for high temperatures, when the kinetic reaction rate is much higher than the transport of gaseous reactants to the particle. Moreover, this reaction is a comparable process to the one used in the studies using the passive reactant in Subsection 2.2.2, while the whole simulation includes more realistic chemistry. This facilitates comparison and analysis. For the global mechanisms, only non-reversible reactions of the form

$$C + O_2 \rightarrow CO_2 \tag{2.39}$$

are considered. The mass loss rate of a single particle is calculated as:

$$\frac{dm_p}{dt} = -\sum_{k}^{N_{species}} \dot{W}_k, \tag{2.40}$$

where the $\dot{W}_k$ is the mass production rate per particle of species k. The mass production rate is:

$$\dot{W}_k = A_p \widehat{P}_k \overline{M}_k, \tag{2.41}$$

where $\widehat{P}_k$ is the surface specific production rate and $\overline{M}_k$ the molar mass. The surface specific production rate is constructed from the stoichiometric coefficients $\upsilon''_{j,k}/\upsilon'_{j,k}$ of the product/reactant side and the reaction rate $\widehat{R}_j$ of reaction j:

$$\widehat{P}_k = \sum_{j}^{N_{reactions}} \widehat{R}_j(\upsilon''_{j,k} - \upsilon'_{j,k}), \tag{2.42}$$

with the rate of reaction j, $\widehat{R}_j$, being:

$$\widehat{R}_j = k_{kin,s,j} \prod_{k}^{N_{species}} (X_{k,s} C_g)^{\upsilon'_{j,k}}. \tag{2.43}$$

The molar concentration of the gas around the particle $C_{g,p}$ is calculated with the ideal gas law,

$$C_{g,p} = \frac{p}{R T_{film}}, \tag{2.44}$$

where the film temperature is $T_{film} = (2T_p + T_{gas})/3$ [134].

Calculating the molar surface fraction:

The evolution of the molar surface fraction $X_{k,s}$ of the reactant species k is, for a general set of reactions, given by [55]:

$$\frac{dX_{k,s}}{dt} = \frac{A_p}{\Theta C_{g,p} V_p}\Big[\underbrace{\widehat{P}_k}_{Consumption} \underbrace{-\Big(\sum_{m}^{N_{species}} \widehat{P}_m\Big) X_{k,s}}_{Stefan\ flow} + \underbrace{k_{diff,k} C_g (X_{k,\infty} - X_{k,s})}_{Diffusion}\Big]. \tag{2.45}$$

The mass transfer coefficient here is found from:

$$k_{diff,k} = \frac{\mathrm{Sh} D_{diff,k}}{2 r_p}, \tag{2.46}$$

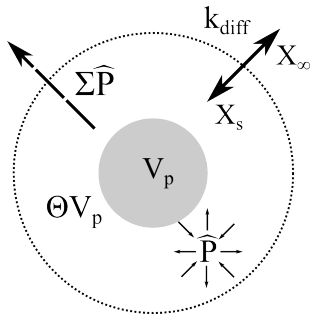

Figure 2.3: Processes in and at the fluid film around the particle

where the Sherwood number is taken from Eq. 2.22 in Subsection 2.2.2. This model assumes that the particle is surrounded by a thin film of fluid which has the surface molar concentration of species $X_{k,s}$. The total volume of the fluid film is ΘV_p, where θ is a parameter relating the volume of the fluid field to the volume of the particle. A vsiualization of the fluid film around the particles and all the processes affecting the surface molar fraction are shown in Fig. 2.3. The diffusive transfer of species between ambient fluid and film is shown by the solid double ended vector. The dashed vector pointing away from the particle describes the transport away from the particle surface by the Stefan flow. The volume of the particle is given by V_p, while the volume of the film zone is given by ΘV_p and the consumption or production of surface species is given by $\widehat{P}$.

The surface molar fraction has to be initialized at startup, either with a chosen value or with the molar fraction of the far field, $X_{k,\infty}$. When equilibrium is assumed for each timestep, $\frac{dX_{k,s}}{dt} = 0$, the term in the square brackets of Eq. 2.45 becomes

$$0 = \widehat{P}_k - \Big(\sum_{m}^{N_{species}} \widehat{P}_m \Big) X_{k,s} + k_{diff,k} C_g (X_{k,\infty} - X_{k,s}), \tag{2.47}$$

and can be used to solve for the surface molar fraction without having to evolve it as a flow variable. For a single unimolar reaction with one reactant (where the second term in Eq. 2.47 is zero), the relation $\widehat{P}_k = k_{kin,s} C_g X_{k,s}$ is used to solve for the surface molar fraction:

$$X_{k,s} = X_{k,\infty} k_{diff,k} / (k_{diff,k} + k_{kin,s}). \tag{2.48}$$

For several reactions involving several reactants, a multivariate set of equations has to be set up and solved by a Newton-Raphson method.

Particle temperature:

The particles are assumed to be thermally thin, resulting in a uniform temperature distribution throughout the particle. This is reasonable for char particles below 7 mm [29], and the particles used in this study are in the μm scale. This means that the assumption of thermally thin particles is valid, which saves on computation time and storage space. The particle temperature evolution is given by:

$$\frac{dT_p}{dt} = \frac{1}{m_p c_{p,p}}(Q_{reac} - Q_c + Q_{rad}), \tag{2.49}$$

where Q_{reac} is the reactive heating rate, Q_c the conductive heat loss to the fluid and $Q_{rad} = \epsilon\sigma A_p(T_w^4 - T_p^4)$ the radiative heat transfer to the wall. Since there is no wall inside the domain, the wall temperature T_w is a parameter that is set at runtime. Further, ϵ is the emissivity and σ the Stefan-Boltzmann constant. This is a simple radiation model which acts mainly as a heat sink in the system. The reactive heating rate is given by the sum of the heat of the reaction multiplied with the reaction rate:

$$Q_{reac} = A_p \sum_{j}^{N_{reactions}} \widehat{R}_j q_{reac,j}. \tag{2.50}$$

The heat of reaction j is calculated as:

$$q_{reac,j} = \sum_{k}^{N_{species}} h_{0,k}(\upsilon'_{j,k} - \upsilon''_{j,k}), \tag{2.51}$$

where $h_{0,k}$ is the heat of formation of species k. The reactive heating only heats up the particle, as the heat loss to the fluid is already accounted for by evaluating the species enthalpy that is transferred to the fluid at the particles temperature.

The conductive heat transfer from the particle to the fluid is:

$$Q_c = HA_p(T_p - T_{gas}). \tag{2.52}$$

The heat transfer coefficient H can be expressed as

$$H = \frac{\mathrm{Nu}k_g}{d_p}\frac{B}{\exp(B) - 1} \tag{2.53}$$

when k_g is the thermal conductivity of the gas mixture and Nu is the Nusselt num-

ber obtained from the Ranz-Marshall correlation [107] for low and intermediate particle Reynolds numbers:

$$\mathrm{Nu} = 2 + 0.6\mathrm{Re}_p^{0.5}\mathrm{Pr}^{0.33} \tag{2.54}$$

with Pr being the Prandtl number of the fluid calculated with

$$\mathrm{Pr} = \frac{\mu c_p}{k_g}. \tag{2.55}$$

The Stefan flow constant B in Eq. 2.53 is given by

$$B = \frac{\dot{m}_p c_{p,g}}{\pi d_p \mathrm{Nu} k_g}. \tag{2.56}$$

The mass bound heat transfer appearing in Eq. 2.30 is thus given by:

$$S_{enth} = \sum_{k}^{N_{species}} \dot{W}_k, h_k(T_{phase}) \tag{2.57}$$

which consists of the sum of the enthalpies h_k of the species transferred to and from the particle and the respective mass production rate. If the species is net consumed at the particle, its enthalpy is evaluated at the gas temperature, if it is net produced, its enthalpy is evaluated at the particle temperature.

2.3.3 Particle reactions with adsorbed species

Detailed heterogeneous mechanisms deal with adsorption and desorption of species on the reactive surface of the particle. When exposed to reactive compounds in gaseous form, adsorbed species can form at carbon atoms on the surface of the particle (called free carbon sites) [57]. The particle is no longer assumed to be spherical and only reactive on the surface, but porous, with pore diffusion and an internal surface.

An example is given as the adsorption of water on two free carbon sites on the surface of a carbonaceous particle to form an adsorbed $C(OH)$ and $C(H)$ complex:

$$2C_f + H_2O \rightarrow C(OH) + C(H), \tag{2.58}$$

which is sketched in the upper left panel of Fig. 2.4. These adsorbed species then

can react with gaseous species,

$$C(O) + CO \rightarrow C_f + CO_2, \tag{2.59}$$

which is shown in the upper right panel of Fig. 2.4, or desorb into the gas phase:

$$C(O) \rightarrow CO. \tag{2.60}$$

This process is shown in the lower left panel of Fig. 2.4. In the figure, black circles are the free carbon sites, oxygen is depicted as a red circle and blue circles are hydrogen atoms. Carbon atoms that are not reachable by gaseous species are light gray. When a adsorbed complex desorbs into the gas phase, an underlying carbon atom subsequently becomes a free carbon site. This type of reaction mechanism is implemented into the "Stanford Code" to study the inhibition by adsorbed species on the surface of char [55] and was extended to read mechanism files. This facilitated studies that investigated the influence of individual reactions on the hydrogen inhibition during char gasification [77, 122]. The equations governing the combustion or gasification of a particle with adsorbed species have been implemented into "The Pencil Code". However, due to constraints in both time as well as in computational resources, no studies have been performed with "The Pencil Code" and these kind of mechanisms. To perform a simulation using a detailed mechanism using adsorbed/desorbed species, the memory required for each particle increases, as does the number of equations. Moreover, the adsorbtion/desorbtion reaction rates can vary by several magnitudes, potentially leading to stiff equations [49]. This, with the necessity to calculate these stiff equations for each particle, restricts use of detailed reaction mechanisms to small scale studies.

Burning mode:

The particle can undergo a change in density, radius and mass during combustion. Depending on the ratio of the speed of reactions to the diffusion of reactants, the particle can undergo combustion in three combustion zones [12, 93]:

- Zone 1: When the speed of reactions is slow compared to the diffusion of reactants inside the particle, combustion is proceeding throughout the particle. The particle is losing mass by losing density.
- Zone 2: This is an intermediate zone of combustion, where the particle is losing mass by shrinking and losing density.

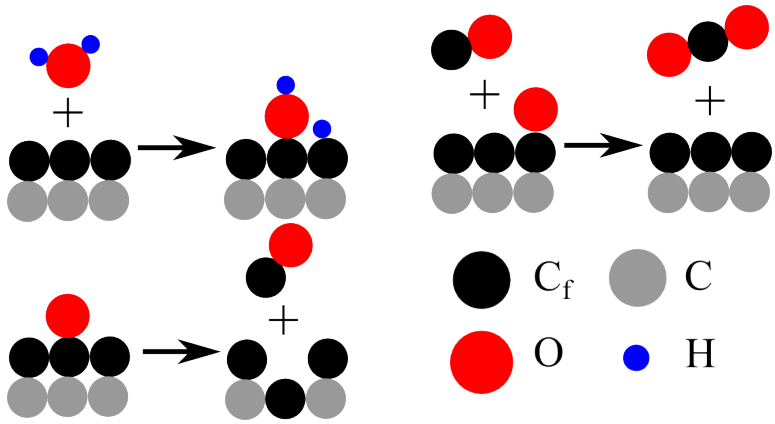

Figure 2.4: Different adsorption/desorption processes: Upper left is $2C_f + H_2O \rightarrow C(OH) + C(H)$, upper right $C(O) + CO \rightarrow C_f + CO_2$, lower left $C(O) \rightarrow CO$

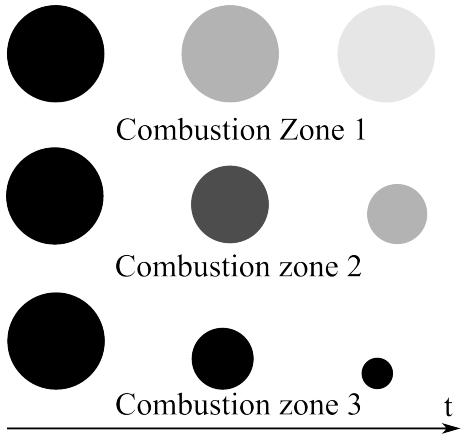

Figure 2.5: Particle size and density evolution over time for different combustion zones.

- Zone 3: When the speed of reaction is high compared to the internal diffusion of reactants in the particle, reactions can be assumed to only be happening at the particles surface. Thus, the particle is losing mass by shrinking, retaining its density.

The different combustion zones are visualized in Fig. 2.5. The denser the particle, the darker it is depicted. While a particle burning in zone 1 retains its radius but slowly loses density, a particle in zone 3 just burns at the surface, shrinking but retaining its density. A particle burning in zone 2 is a mixture of both. The relation between the density evolution and its mass evolution taking into account

the combustion zone is:

$$\frac{\rho(t+\Delta t)}{\rho(t)} = \left(\frac{m_p(t+\Delta t)}{m_p(t)}\right)^{\alpha}, \tag{2.61}$$

while the relation between the mass of a particle and its size is:

$$\frac{r_p(t+\Delta t)}{r_p(t)} = \left(\frac{m_p(t+\Delta t)}{m_p(t)}\right)^{\beta}. \tag{2.62}$$

The burning mode parameter α is zero when the particle is only reaction on the surface and 1 when the particle is reacting throughout its volume. The burning mode parameter β, on the other hand, is zero when the particle is reacting in zone 1, and $1/3$ when only reacting on the surface. By assuming spherical particles, all combinations have to obey following law:

$$\alpha + 3\beta = 1. \tag{2.63}$$

Effectiveness factor:

To find the combustion zone, which defines if a particle is reacting only on its outer surface, or throughout its internal, much larger surface, Thiele [121] defined an effectiveness factor η_{Thiele}. This effectiveness factor relates the actual reaction rate that is happening to the rate that would occur if the particle was reacting using all its internal surface. The effectiveness factor of species k for a reaction of order n is given by:

$$\eta_{Thiele,k} = \frac{3}{\phi_{n,k}}\left(\frac{1}{\tanh\phi_{n,k}} - \frac{1}{\phi_{n,k}}\right), \tag{2.64}$$

with $\phi_{n,k}$ being the Thiele modulus:

$$\phi_{n,k} = \phi_k \sqrt{n+1/2} \tag{2.65}$$

$$\phi_k = r_p \sqrt{\frac{\widehat{P}_k \rho_p S_{gc}}{C_g X_k D_{eff,k}}} \tag{2.66}$$

For a second order reaction, the value of n in Eq. 2.65 is 2. The effective diffusion in this case is given by the harmonic mean of the bulk species diffusion coefficient

D_k and the Knudsen diffusion D_{Kn}:

$$D_{eff,k} = \frac{1}{D_k} + \frac{1}{D_{Kn,k}}, \tag{2.67}$$

where the Knudsen diffusion coefficient of species k is the diffusion speed where the pores inside a material are so small that molecules will collide with the wall instead of other molecules:

$$D_{Kn,k} = \frac{2r_{pore}\theta}{3\tau}\sqrt{\frac{8RT_p}{\pi\overline{M}_k}}. \tag{2.68}$$

The tortuosity factor τ takes into account the random direction of the pores and is a parameter. The porosity θ of the particle is given by $\theta = 1 - \frac{\rho_p}{\rho_c}$, where ρ_p is the density of the particle and ρ_c the density of solid carbon. To obtain the mean radius of the pores in the particle r_{pore}, the porosity θ, roughness factor f_r, the particle density and the internal area to mass ratio S_{gc} is used:

$$r_{pore} = \frac{2f_r\theta}{\rho_p S_{gc}}. \tag{2.69}$$

Since an effectiveness factor of zero represents no internal reactions, it can be used to describe the combustion zones, and the assumption

$$\alpha = \eta_{Thiele} \tag{2.70}$$

is made to calculate the burning mode of a particle.

Evolution of the particle total surface:

The total surface S_{tot} of a particle is given by $S_{tot} = S_{gc}m_p$, where S_{gc} is a mass specific surface area. The evolution of the particle surface area over the conversion $c = 1 - m_p(t)/m_{p,0}$ is given by:

$$S_{tot}(t) = (1-c)S_{tot,0}\sqrt{1 - \psi\ln\left(\frac{\rho_p}{\rho_{p,0}}\right)}, \tag{2.71}$$

where ψ is a structural parameter. This treatment allows for all kinds of combustion zones [93]. The ini tial particle density $\rho_{p,0}$ is then needed to be saved for each particle.

Evolution of the adsorbed species:

If reaction mechanisms with gas phase and adsorbed species are considered, the definition of the reaction rate from 2.43 in Subsection 2.3.2 has to be extended to account for the concentration of adsorbed reactants C_s:

$$\widehat{R}_j = k_{kin,j} \prod_k^{N_{species}} (C_g X_k)^{\upsilon'_{j,k}} \prod_l^{N_{adsorbed}} (C_s \Theta_l)^{\mu'_{j,l}}, \tag{2.72}$$

where C_s is the molar surface concentration of sites, Θ_l the site fraction of adsorbed species l and $\mu'_{j,l}$ the stoichiometric coefficient for adsorbed species l in reaction j. The evolution equation of the site fraction of adsorbed species l is:

$$\frac{d\Theta_l}{dt} = \frac{\widehat{R}_l}{\xi_n} + A_{mod} \widehat{R}_c \Theta_l, \tag{2.73}$$

where ξ_n is the surface concentration of all adsorption sites, occupied or not. This equation has to be solved for all adsorbed species except the free sites, which are calculated as:

$$\Theta_{free} = 1 - \sum_j^{N_{adsorbed}} \Theta_j. \tag{2.74}$$

The first term on the RHS in Eq. 2.73 is due to the desorption and adsorption rates of species l, $\widehat{R}_l$:

$$\widehat{R}_l = \sum_j^{N_{reactions}} (\mu''_{j,l} - \mu'_{j,l}) \widehat{R}_j. \tag{2.75}$$

The second term in Eq. 2.73 is due to the change in total sites present in the particle. It is composed of the modified surface area A_{mod}:

$$A_{mod} = \left(1 - \frac{S_{t,0}^2 (1 - c^2)}{2 S_t^2}\right) S_{gc} \overline{M}_c, \tag{2.76}$$

where the initial total surface area $S_{t,0}$ and the current total surface area S_t are taken from Eq. 2.71. The carbon loss rate R_c is the speed with which the char

particle is losing its constituent char:

$$\widehat{R}_c = M_c \sum_{k}^{N_{species}} \left(\sum_{j}^{N_{reations}} \widehat{R}_j (\upsilon''_{j,k} - \upsilon'_{j,k}) a_{c,k} \right), \tag{2.77}$$

where $a_{c,k}$ is the amount of carbon atoms in species k. Only the gaseous species are considered here because they are the only ones that are transferred to the gas phase.

Heat of reactions:

For reactions involving adsorbed species, the heat of reaction k, which is used in Eq. 2.50 in Subsection 2.3.2 is:

$$q_{reac,j} = \sum_{k}^{N_{species}} h_{0,k} (\upsilon'_{j,k} - \upsilon''_{j,k}) + \sum_{r}^{N_{adsorbed}} h_{0,r} (\mu'_{j,r} - \mu''_{j,r}), \tag{2.78}$$

where $h_{0,k}$ and $h_{0,r}$ are the heat of formation of the gaseous and adsorbed species, respectively. The absolute entropy of and enthalpy of formation of adsorbed species can be found in the article by Tilghman and Mitchell [122] and its supplementary material.

2.4 The Pencil Code and implementation details

”The Pencil Code” is a compressible DNS code mainly used in astrophysics, e.g. for hydrodynamics in magnetic fields [16]. Its development started 2001, and since 2008 it has been open, first via google code (now discontinued) and now via GitHub [17]. It is open source, fully customizable and has to date been used in over 400 research articles [99]. The spatial discretization is done by using compact sixth order schemes for the first and second derivative. For the time stepping, a memory efficient third order Runge-Kutta scheme of the 2N type [14] is used. The equations are advanced in time along a one dimensional pencil in the domain to use the processors cache most efficiently, hence the name ”The Pencil Code”. It shows excellent weak scaling for large simulations until up to 70.000 cores [14].

Setup:

The code is not one program that is loaded with different parameters to deal with different problems, but is rather compiled to solve exactly the problem it is defined for. Defining the problem is done by setting numerical values such as the resolution, number of processors to use, the domain distribution and number of particles in parameter files. Moreover, the code comes with several *modules*, that define the equations that are solved, for examples hydrodynamics with and without magnetic fields and shocks, particles that are agglomerating and condensating, dust particles that form into planets or are burning. By activating/deactivating modules, one is able to precisely build a software that just simulates what is required, with no overhead. Moreover, this made extension of the code to account for chemically reactive particles relatively straightforward, since it ”just” involved creating new modules that describes the governing equations.

After a choice of the resolution and the equations to be solved has been made, the preprocessor changes the code files of the base code accordingly and compiles a program that is optimized for exactly this problem. Start or run parameters are then set up in input files. These can then be changed as desired, and the code can be forced to reload some of the parameters while running.

The main work of this thesis was to add three modules to ”The Pencil Code”:

1. The surface species module holds the chemical species in the surface film around the particle and their properties in its array for each particle. It provides also all diagnostics relating the gaseous surface species.

2. The adsorbed species module holds the chemical properties storage space for adsorbed species on each particle. It holds also all diagnostic functionality considering the adsorbed species on each particle.

3. The particles chemistry module accesses the modules above and other modules to obtain information about the particles velocity, mass, temperature and further information. With all the information, the equations for evolving the particle properties are set up. While having nearly no diagnostic function on its own, it collects a lot of information from other modules to set up the equations. The mechanism file for determining the particle reactions is read here and the information is then send to other modules.

Special efforts were undertaken to make all the related modules communicate consistently and free of side effects, since some can use different interpolation methods and can switch between evolving a variable or the logarithm of it. Additionally, some effects, such as mass loss, can be switched to affect one property of the flow without affecting another. As an example, a particle can transfer mass to the flow, and the mass loss is saved as a diagnostic, all while the particles mass is held constant, which was essential for the studies conducted in Paper 5 [75].

Due to the massive calculations that a simulation of a highly turbulent combustion system would require, a range of methods have been implemented that potentially lessen the computational load on the particle side. Since they usually result in a slight loss of precision, it is possible to choose the ”exact” or ”fast” method for each process. As an example, the heat of reaction can either be calculated for each reaction for each particles temperature, or only for the integer range of temperatures that is defined by the minimum and maximum temperature of all particles in the current calculation. The heat of reaction of a particle is then not evaluated at its exact temperature, but rather the nearest integer value. This is especially helpful for a large number of particles, since the range of particle temperatures at one time is usually not too high. Another example is the diffusion of the back reaction of particles on the fluid grid. Instead of performing a high-order reverse interpolation to distribute the particles influence onto the grid, the particles influence is stored on a temporary grid using the Projection onto Neighboring Nodes (PNN) method [35] and this field is then diffused before it is applied to the fluid grid. This shifts the computational load from a per-particle basis to a per-field basis. On the other hand, the effect of the exact position of the particle on the particle-fluid transfer is lost due to the PNN method.

Chapter 3

Contributions

The contributions to the present thesis are five papers that are published in, or submitted to, peer-reviewed national and international journals. In order to obtain the results in the papers, three main tasks were performed:

1. The ”Stanford Code” was extended, a combustion model used and proposed in the paper of Haugen et al. [55]. It computes combustion of carbonaceous particles in a cloud of uniformly reacting particles. This software was extended to read reaction mechanisms. The extended ”Stanford Code” was used to investigate hydrogen inhibition during char gasification [77].

2. ”The Pencil Code”, an open source CFD code available on GitHub [16, 45] was extended. Before the extension, it could simulate inert particles in turbulent reacting flows. The extended ”Stanford Code” was implemented as a sub model to account for heterogeneously reacting particles and the associated transfers of mass, species, energy and momentum. The extended code was used to study the influence of turbulence on char particles reacting under oxy-fuel conditions [74].

3. To study relevant phenomena in turbulent reacting flows, simulations with appropriate boundary conditions were set up and run. This was followed by subsequent post processing and discussion of the results.

The papers were worked on during different stages of the Ph.D. studies. Figure 3.1 gives an overview about the changes made to the simulations software as well as the basic finding of the paper. Paper 1 and Paper 2 are studies of the

consumption of a passive reactant, which was already implemented into ”The Pencil Code”. Here simulations were set up and run, and data obtained from them investigated. Simulations with different particle numbers, different Stokes and mass diffusivity were performed.

Paper 1 and 2 argue for the existence of an upper limit to the reaction rate which is dependent on flow conditions and therefore could not be surpassed by adding more particles.

For Paper 2, simulations with different Stokes numbers were performed. A simple model connecting the reaction rate limit for low and high particle numbers was proposed and supported by reaction rates obtained from the simulations.

Paper 3 is an indirect result of the extension of the ”Stanford Code”. To facilitate re-usability, the ”Stanford Code” was extended to read Chemkin-like mechanism files [68] instead of inserting the reaction mechanism into the source files. This enabled the main author to easily activate and de-activate individual reactions without the need to re-compile, facilitating a parametric study of hydrogen inhibition on reactive particles. The ”Stanford Code” is able to handle detailed reaction mechanisms with adsorbed species and internal reactions, as well as different combustion regimes.

Paper 4 extends the analysis done in Paper 2 and accounts for slip velocity between the fluid and each individual particle by using a Ranz-Marshall correlation [107] for the mass transfer rate. Additionally, an expression for the mean slip velocity depending on the particles Stokes number is proposed.

In order to analyse the effect of turbulence on reaction rates for more realistic chemistry, the extended ”Stanford Code” was used for the implementation of chemically reacting particles into ”The Pencil Code”. Then, the study of the effect of turbulence on reacting particles was performed for Paper 5. Here, only one Stokes number and a one-step global reaction was studied.

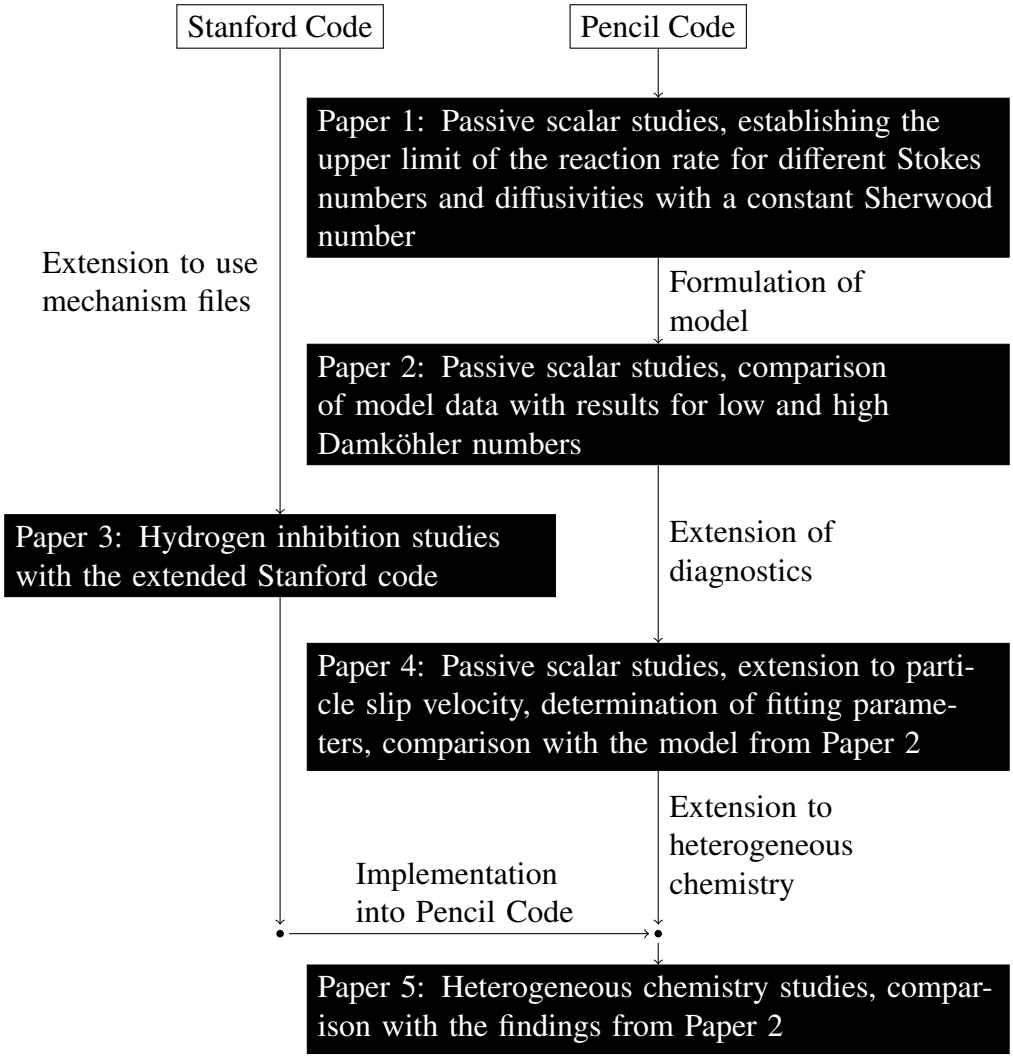

Figure 3.1: Structure of the contributions and published works, with tasks positioned in-between

3.1 Paper 1: A study on the coupling between isotropic turbulence and heterogeneous reactions

DNS studies are performed to shed light on the effect of turbulence on heterogeneous reaction rates using a Eulerian-Lagrangian approach, where the particles are much smaller than the grid size and therefore assumed to be point-particles.

The reacting system is modelled with a passive reactant which is convected and diffused by the flow field, but only consumed at the particles surface. The flow has a moderate Reynolds number and is isothermal, and the reaction unimolar, not affecting the flow field. Inertial particles with small or large Stokes numbers based on the flow integral scale are studied. Momentum coupling of the particulate and the fluid phase is two-way, meaning the drag force particles experience is transferred back to the fluid grid. The mass transfer coefficient to the particles is modelled with the Sherwood number assuming quiescent fluid. It is found that the unmixing of particles due to turbulence slows down the reaction rate for large particle numbers if the turbulent and chemical time scales are of comparable magnitude. The slow-down of reactions is stronger for particles with a time scale more comparable to the one of the fluid. Increasing the mass diffusivity increases the overall reaction rate, but a upper limit still exists.

This can be seen in Fig. 3.2. In the figure, the decay rate of the passive scalar as a function of the Damköhler number (which is varied by varying the number of particles in the domain) is shown for a particle Stokes number of 0.3 (upper panel) and 1.0 (lower panel). As the Damköhler number is increased, the resulting decay rate increases as well, but the increase is smaller for higher Damköhler numbers. Two limits appear: One is for small Damköhler numbers and is the limit signified by the dashed-dotted line for the homogeneous assumption, where the fluid would be perfectly mixed and each particle reacts without influence from other particles. The other limit is the flow dependent limit, which depends on the size and shape of the particle clusters that have formed because of the flow turbulence. These clusters are not influenced by more internal particles and therefore independent of the Damköhler number. Diffusive transport due to turbulent motion appears to be less important than the mass diffusivity of the fluid.

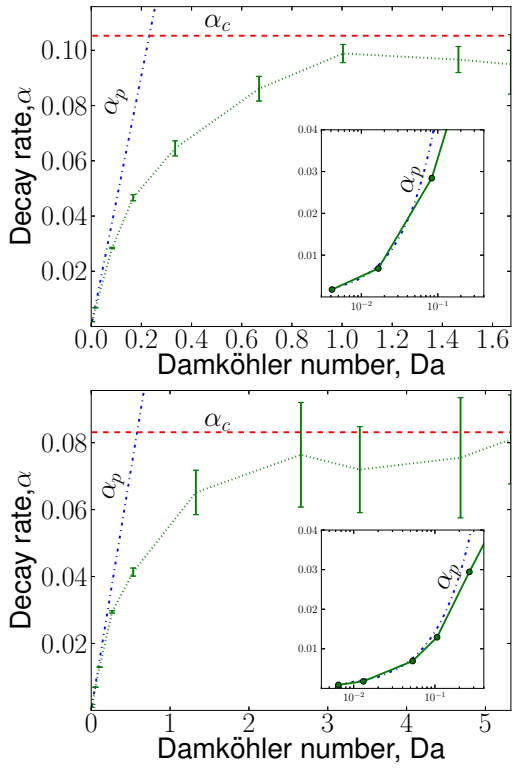

Figure 3.2: The mean decay rate of the passive reactant as a function of the Damköhler number (read: particle number) for two different particle Stokes numbers: 0.3 (upper panel) and 1.0 (lower panel). The dashed-dotted line is the limit for the ideal homogeneous assumption, the dashed line the flow dependent limit for the decay rate.

3.2 Paper 2: The effect of turbulent clustering on particle reactivity

Turbulent flows with reacting inertial particles are investigated with the help of DNS at intermediate Reynolds numbers. Akin to the studies in Paper 1, a passive reactant is transported by the fluid and consumed at particles that are placed in the flow. The particles are modelled as small, inertial point-particles that are suspected to the Stokes drag with a Schiller-Naumann correlation [111] for low to intermediate particle Reynolds numbers. Particle collisions are not considered. Two different particle sizes are considered, having different dynamics in the flow. Data from one particle size and mass diffusivity from earlier work [73] as well as new data was used. The particle clustering due to turbulence separates the

particle clusters from regions with remaining passive reactant, leading to a slow-down of the consumption of the reactant. This effect happens when the number of particles in the domain is high. For low particle numbers, the total reaction rates scales linear with the number of particles, but already for intermediate particle numbers this trend is abandoned. A model connecting the limit of particle number proportional reaction rate and the upper, particle number independent limit is proposed and compared against the reaction rates obtained from DNS.

The model and results obtained from simulations are shown in Fig. 3.3. The mean and variance of the decay rate for cases with varying Damköhler number is shown. The solid line is the proposed model, connecting the linear model of perfectly mixed particles and gas with the flow dependent upper limit of the decay rate with a harmonic mean. Already for low Damköhler numbers, a significant deviation from the assumption of perfect mixing is observed.

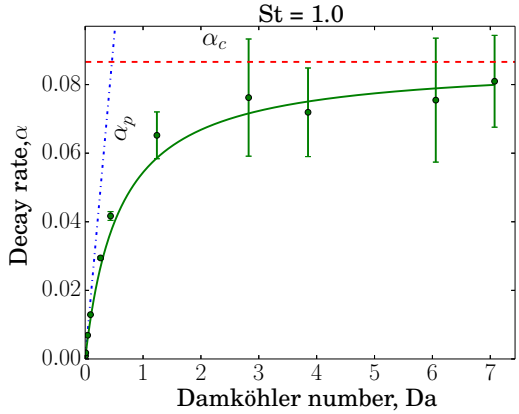

Figure 3.3: The mean and variance of the decay rate of the passive reactant as a function of the Damköhler number (read: particle number) for a particle Stokes number of 1.0. The dashed-dotted line is the limit for the ideal homogeneous assumption, the dashed line the flow dependent limit for the decay rate. The solid line shows the result of the proposed model.

3.3 Paper 3: Numerical Study of Hydrogen Inhibition of Char Gasification Using Detailed Hetero- and Homogeneous Chemical Kinetics

The effect of hydrogen present in the gas phase on char gasification rates for Wyodak coal is studied. The ”Stanford Code” [55] is used. It assumes cluster

of uniformly reacting char particles in a cloud of perfectly mixed gas. No spatial information is used. The particles are assumed to be spherical and only char is reacting with gas phase species. For heterogeneous combustion, the detailed chemical mechanism of Tilghman and Mitchell [122] and for homogeneous combustion, the propane mechanism GRI-Mech 3.0 [113] is used. The initial gaseous atmosphere contained 50 mole-% H_2O, 45 mole-% O_2 and 5 mole-% N_2 and a pressure of 24 bar is assumed. To study the impact of hydrogen on char conversion without altering the chemistry, the two heterogeneous reactions having hydrogen as a reactant are enabled or disabled at different gas temperatures, and the subsequent char conversion rates investigated. It is found that for temperatures below 2000 K, hydrogen present in the gas slows the conversion rate, while it slightly increases the conversion rate for temperatures above 2000 K. This can be seen in Fig. 3.4, where the normalized time to reach full conversion as a function of the temperature is shown for the different cases. The time is normalized by the time to full conversion of a base case, case A, where both reactions having hydrogen as a reactant are enabled. For low temperatures, case C with the second of the hydrogen reactions enabled reacts much slower than case A, while the cases where the first hydrogen reaction or both are disabled react faster than case A. At high temperatures, case C, with the second hydrogen reaction disabled reacts slightly faster than case A, while case B, with the first reaction disabled, or case D, with both reactions disabled, react much slower than case A.

The inhibition mechanism found for lower temperatures in this simulation is following: An adsorbed hydrogen reacts with an adsorbed oxygen atom to form an adsorbed OH complex on the surface. This complex then reacts with another adsorbed hydrogen to form steam. An adsorbed oxygen atom that most probably desorbs as carbon monoxide is converted to steam, and does not contribute to the removal of carbon from that particle surface. At higher temperatures, adsorbed hydrogen reacts with steam to produce an adsorbed oxygen atom on the surface that subsequently desorbs as carbon monoxide, increasing the conversion rate.

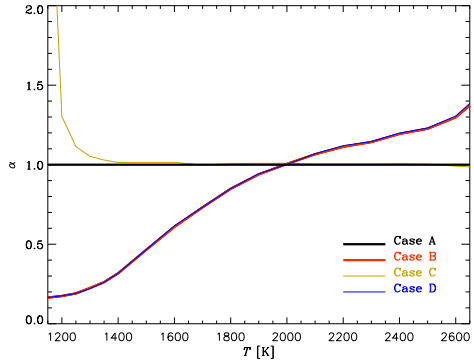

Figure 3.4: Normalized time to reach full conversion as a function of the temperature. The times are normalized by the time it takes case A, with both hydrogen reactions enabled, to reach full conversion. Disabling the hydrogen reactions can speed up of slow down conversion time, depending on the temperature.

3.4 Paper 4: The effect of turbulence on mass and heat transfer rates of small inertial particles

This work is an extension of Paper 2 [75]. It further investigates the effect of flow turbulence on reactive particles. Inertial particles are placed in a turbulent, isothermal fluid, where they consume a reactant that is transported by the fluid. The grid resolution is fine enough to resolve even the smallest scale of the flow, so no turbulence modelling is required. Flow turbulence is produced by a random forcing, yielding homogeneous, isotropic turbulence. Gravity is neglected and all domain boundaries are periodic. The particles are much smaller than the grid size and are treated as point-particles, tracked by a Lagrangian approach. The effect of turbulence is investigated for several particle sizes, particle number densities and turbulence intensities. The particle stopping time is calculated using the Schiller-Naumann correlation [111] for low to intermediate particle Reynolds numbers, and the particles are two-way coupled with the fluid. The effect of turbulence on each particles reaction rate is accounted for by a Ranz-Marshall correlation for the mass transfer rate, directly affecting how fast the particles consume the passive reactant. The particles are placed in the developing turbulence and allowed to cluster until a statistically steady state is reached, when the particle reactions are activated. The consumption rate of passive reactant was investigated to find the connection between the reaction rate of the reacting particles and particle clustering.

A correlation for the mean slip velocity between fluid and particles is proposed and compares well with data for particles of several sizes and flow turbulence intensities. Together with a correlation for parameters relating to the size and shape of particle clusters depending on the particle size, a model for a modified Sherwood number is found. This modified Sherwood number takes into account the positive influence of the particle-fluid slip velocity on the reaction rate, as well as the negative effect of particle clustering. In Fig. 3.5, the mean and variance of the normalized consumption rate is shown for particles with a Stokes number of 1 and different flow Reynolds numbers as a function of the Damköhler number. The reactant consumption rate is normalized by the consumption rate obtained by assuming perfect fluid mixing, no slip velocity and homogeneous distribution of particles. The proposed model agrees well with the simulation data for a wide range of Reynolds numbers. The positive influence of the slip velocity is evident from the speed up (normalized consumption rate > 1) for low Damköhler numbers. The decrease of the normalized consumption rate for higher Damköhler numbers is also well captured by the model.

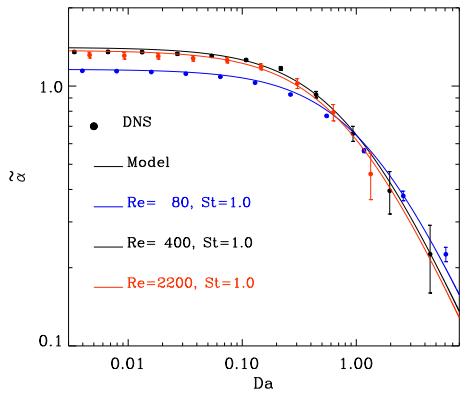

Figure 3.5: Mean mass loss rate normalized by the ideal mass loss rate assuming perfectly mixed fluid as a function of the Damköhler number. The lines show the predictions of the model from previous work [75], with both correlations for the slip velocity and the parameters relating to the shape and size of particle clusters in use.

3.5 Paper 5: Correlation effects between turbulence and the conversion rate of pulverized char particles

The effect of turbulent clustering on the combustion rates in an pulverized fuel flame with a Reynolds number of 40 is studied in DNS. The particles are assumed to consist of dried and devolatilized char, so only heterogeneous combustion reactions are considered. To further simplify the system, the oxidiser is an oxygen-carbon dioxide mixture and the combustion product is carbon dioxide, so no homogeneous reactions take place. Moreover, the particles are assumed to be everlasting, decreasing in neither size nor density. The turbulence is continuously forced, isotropic and homogeneous. Thermal effects, mass and species transfer are accounted two-way, while the momentum transfer is only modelled as being from the fluid to the particle. The particles are tracked with a Lagrangian approach, and both the Stokes drag as well as the mass transport coefficient of oxygen to the particle surface use empirical correlations to account for relative velocity between particle and fluid. A simple radiation model is assumed for the particles. If few particles are in the domain, the turbulence increases the combustion rate by speeding up the transport of fresh oxygen to the particle surface. It is, however, found that if the number of particles in the domain is increased, the total combustion rate scales only linear for low particle numbers and then begins to flatten out against a flow dependent combustion rate. This effect is due to the clustering of particles due to the flow turbulence, effectively separating them from clouds of unburned oxygen. Earlier studies of simplified reaction systems confirm this effect [75], and a model proposed by them is compared with the new results, with good agreement. Deviations are thought to come from thermal effects that have to be studied. The data from the simulations and the proposed model can be seen in Fig. 3.6. Shown is the mean mass loss rate of the char particles normalized by the ideal mass loss rate assuming perfectly mixed gas in the domain. Also observable is the speed up for low Damköhler numbers as a result of the increased mass transfer due to slip velocity between the fluid and the particles. For large Damköhler numbers, the decrease in mass loss rates due to spatial separation between particle clusters and oxidiser becomes dominant.

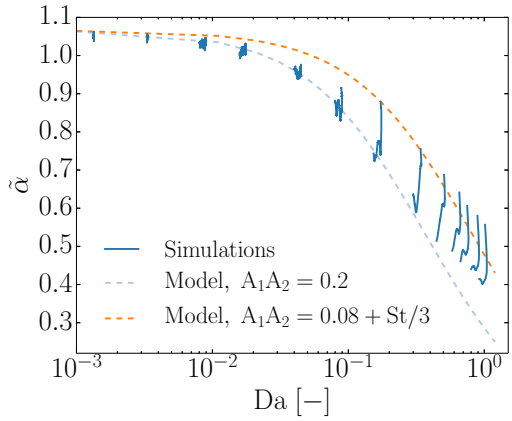

Figure 3.6: Mean mass loss rate normalized by the ideal mass loss rate assuming perfectly mixed fluid as a function of the Damköhler number. The dashed lines show the model from the previous work [75], with a fitting value obtained from the work of Haugen et al. [54] and a value of 0.2.

Chapter 4

Conclusions

From the studies conducted in this thesis, it is clear that turbulence influences the rates of heterogeneous reactions as they happen in and on fuel particles. This influence manifests itself differently, depending on the scale of focus. Two different effects of turbulence, occurring on two different scales, are identified: One, on small scales, with a positive influence on the reaction speed. The other, happening at intermediate and large scales, decreasing the speed of reactions.

On small scales, slip velocity between the fluid and particle increases the mass, species and energy transfer. This increases the transfer of reactant species to the particle, speeding up reactions, which is in accordance with accepted knowledge [107, 91].

On large scales, the picture is different. Depending on the inertia of the particles and the acceleration they are subjected to, particles concentrate in certain regions of the flow. This concentrating, or clustering of particles, leads to regions of high particle number density, separated by regions of low particle number density. If the oxidiser is in the gaseous phase and the particles contain the fuel, once all oxidiser close to the particles is consumed, the reaction rate slows down. This is because reactions are limited by the transfer rates between the fuel-rich and oxygen-rich regions. This effect of clustering and high particle number densities on heterogeneous reactions has already been analysed analytically by Annamalai and Ramalingam [4] for heterogeneous combustion and numerically by Reveillon and Demoulin [108] for evaporating droplets. For homogeneous combustion, a similar effect is seen in turbulent non-premixed combustion, where the combustion rate is limited by mixing [104]. The detrimental effect of clustering is, however dependent on the overall particle number density and their degree of clustering, and for one given flow, the range of particle number densities con-

tained can be very wide [32]. While this effect is counteracted by the *relatively* slow char reaction rates compared with devolatilization rates [118], the already long residence times in furnaces may not be sufficient to completely burn a dense particle cluster that has been formed by a vortex.

Simulations used to design industrial scale combustion systems need to use methods that rely on sub-grid scale modelling such as RANS or coarse LES. The effect of clustering of particles in turbulence is not resolved in these simulations. While there are a lot of models to account for subgrid scale turbulence effects for homogeneous reactions, there is none for heterogeneous reactions. For these models, in each grid cell, the gas and the particles are assumed perfectly mixed for heterogeneous reactions, which can, in extreme cases, over predict the reaction rate significantly [74]. The present study has worked towards a sub model that predicts the slow-down or speed-up of reactions due to turbulence from known flow and particle properties of small combustion systems. The combustion system in question featured homogeneous, isotropic turbulence and was gradually extended in complexity to get closer to a physically realistic description. While the starting point were reactions that left the fluid and particles unaffected, the current combustion system features real, temperature dependent chemistry and transfer of properties from particle to the fluid and back. For all stages of complexity, the observed effect is present and the proposed model agrees fairly well with the data obtained from the numerical experiments (DNS). The properties used by the sub model are particle size, inertia and number density, together with flow temperature, turbulence intensity and oxidiser content, which are all known in industrial scale simulations. The sub model shows good agreement with the DNS results. However, further connections and interactions between flow and particle properties have to be explored.

4.1 Future work

DNS is a powerful tool to develop such models, but a lot of questions have still to be answered to increase the predictive capabilities of the model. The areas requiring further investigation for the current system are:

- Simulations with higher Reynolds numbers are recommended. While the simulations employing the passive reactant system featured intermediate Reynolds numbers, for real chemistry only small Reynolds numbers were studied.

- The particles studied until now were everlasting. Knowledge is required on how the effects of the turbulence on the reaction rate change if the particles shrink or become less dense during combustion. Simulations for this study can be set up without extending the program, although the methodology for interpreting the data would need to be adapted.

- Thermal effects have to be investigated by studying the combustion system at different temperatures and fuel compositions. This could be achieved without expanding "The Pencil Code".

- All studies conducted until now had one particle diameter for all particles. Assigning each particle a random size according to a Rossin-Rammler distribution is already implemented. Thus, analysing a combustion system with several different radii is straightforward.

- Further investigations of the shape, size and volume-to-surface ratio of the particle clusters are recommended. The generation of particle cluster data can be accomplished with "The Pencil Code" as is, but new post processing scripts are required.

- Combustion systems featuring adsorbed species and adsorption/desorption processes on the surface and in the interior of a porous particle should be investigated. The use of mechanisms featuring adsorbed species and different burning modes is already implemented into "The Pencil Code", but needs validation. For entropies and enthalpies of adsorbed species, the work of Tilghman and Mitchell [122] can be used. Moreover, a new method to deduct a chemical time scale from the results would be required.

- Right now, all particles are assumed to be spherical. To investigate biomass particle combustion, the particle model would need to be extended to account for non-sphericity. This encompasses additional equations of motion (for the alignment and rotation), as well as particle properties such as sphericity would need to be evolved. This requires extensive work with "The Pencil Code".

Additionally, the effects found in the DNS studies need to be validated by experimental investigations of reactive particles in isotropic turbulent flows. A starting point of such an experiment could be the turbulence chamber described by Wood et al. [131], filled with dried and devolatilized fuel particles instead of glass or lycopodium. Sensor equipment similar to the one used to analyse the

CRIEPI flame [61] is recommended. This would potentially yield comparable conditions as in the simulation. Two significant problems are already evident. The transient nature of this "closed" combustion process makes the study of one set of chemical and particle time scales difficult, since both depend on the particle size and temperature among others. The other, more physical than methodical, is building and operating such a test rig, as the additional measurement devices add significant complexity to the device used by Wood et al. [131]. Alternatively, measurements of the CRIEPI flame further downstream would allow to capture more of the combustion process. Right now, particles that have gone through the CRIEPI have only emitted half their volatile matter [92]. This approach has the "disadvantage" of featuring non-isotropic turbulence, but this can be easily mirrored by simulations [85]. "The Pencil Code" has the potential to simulate systems that are more complex than the systems already investigated. To give an example, the current system features homogeneous isotropic turbulence. By changing the boundary conditions, a temporal evolving jet could be simulated and compared to experimental PCC flames (like the CRIEPI flame). This could be achieved without expanding "The Pencil Code". Results from these studies could be compared to existing experimental and numerical studies of the CRIEPI flame [61, 85, 118].

Finally, a different possible direction of research can focus on more detailed and complete reaction systems, incorporating drying, devolatilization and combustion. This needs to be done to shed light on the effect of turbulence on the whole combustion process. While potentially insightful, such a study is a major task: In addition to being computationally expensive, analysing a system with several processes running in parallel is hard to reduce to one time scale. Especially if reaction rates differ by some orders of magnitude. A new post processing method would be required, and the particle reaction module of "The Pencil Code" would need to handle different ways to calculate the reaction rates.

Bibliography

[1] Cardoon description on wikipedia, February 2017. Available at `https://en.wikipedia.org/wiki/Cardoon`.

[2] Audai Hussein Al-Abbas, Jamal Naser, and Emad Kamil Hussein. Numerical simulation of brown coal combustion in a 550 {MW} tangentially-fired furnace under different operating conditions. *Fuel*, 107:688 – 698, 2013.

[3] K Annamalai and Sc Ramalingam. Group combustion of char carbon particles. *Combustion and Flame*, 70(3):307–332, DEC 1987.

[4] K Annamalai and William Ryan. Interactive processes in gasification ii. *Progress in Energy and Combustion Science*, 19:383–446, 1994.

[5] Ansys Inc. Ansys 15.0 theory guide, Aug 2014. Available at `http://www.ansys.com/`.

[6] Ansys Inc. Ansys 17.2 capabilities, Dec 2016. Available at `http://www.ansys.com/`.

[7] Donald B. Anthony and Jack B. Howard. Coal devolatilization and hydrogasification. *AIChE Journal*, 22(4):625–656, 1976.

[8] N. Babkovskaia, N.E.L. Haugen, and A. Brandenburg. A high-order public domain code for direct numerical simulations of turbulent combustion. *Journal of Computational Physics*, 230(1):1 – 12, 2011.

[9] M. M. Baum and P. J. Street. Predicting the combustion behaviour of coal particles. *Combustion Science and Technology*, 3(5):231–243, 1971.

[10] Jérémie Bec. Fractal clustering of inertial particles in random flows. *Physics of Fluids*, 15(11):L81–L84, 2003.

[11] David A. Bell, Brian F. Towler, and Maohong Fan. *Coal Gasification and its Applications*. Elsevier, 2011.

[12] S. K. Bhatia and D. D. Perlmutter. A random pore model for fluid-solid reactions: I. isothermal, kinetic control. *AIChE Journal*, 26(3):379–386, 1980.

[13] R. W. Bilger. Conditional moment closure for turbulent reacting flows. *Physics of Fluids A: Fluid Dynamics*, 5(2):436–444, 1993.

[14] A. Brandenburg. *The pencil code manual - Numerical Methods*. NORDITA, July 2015. Available at `http://pencil-code.nordita.org/doc.php`.

[15] Axel Brandenburg. The inverse cascade and nonlinear alpha-effect in simulations of isotropic helical hydromagnetic turbulence. *The Astrophysical Journal*, 550(2):824, 2001.

[16] Axel Brandenburg. Pencil code homepage, July 2014.

[17] Axel Brandenburg. Pencil code homepage github page, January 2017.

[18] K.N.C. Bray and J.B. Moss and. A unified statistical model of the premixed turbulent flame. *Acta Astronautica*, 4(3):291 – 319, 1977.

[19] T Brosh and Nilan Chakraborty. Effects of equivalence ratio and turbulent velocity fluctuation on early stages of pulverized coal combustion following localized ignition: A direct numerical simulation analysis. *Energy and Fuels*, 28:6077–0688, 2014.

[20] David Tillman Bruce Miller. *Combustion Engineering Issues for Solid Fuel Systems*. Academic Press, 2008.

[21] S.P. Burke and T.E.W. Schumann. Diffusion flames. *Industrial & Engineering Chemistry*, 20:998–1004, 1928.

[22] S.P. Burke and T.E.W. Schumann. Kinetics of a type of heterogeneous reaction: the mechanism of combustion of pulverized fuel. *Industrial & Engineering Chemistry*, 23:406–413, 1931.

[23] Enrico Calzavarini, Martin Kerscher, Detlef Lohse, and Federico Toschi. Dimensionality and morphology of particle and bubble clusters in turbulent flow. *J. Fluid Mech.*, 607,:pp.13–24,, October 2007.

[24] M. Cencini, J. Bec, L. Biferale, G. Boffetta, A. Celani, A. S. Lanotte, S. Musacchio, and F. Toschi. Dynamics and statistics of heavy particles in turbulent flows. *Journal of Turbulence*, 7:N36, 2006.

[25] J H Chen, A Choudhary, B de Supinski, M DeVries, E R Hawkes, S Klasky, W K Liao, K L Ma, J Mellor-Crummey, N Podhorszki, R Sankaran, S Shende, and C S Yoo. Terascale direct numerical simulations of turbulent combustion using s3d. *Computational Science & Discovery*, 2(1):015001, 2009.

[26] Choeng Ryul Choi and Chang Nyung Kim. Numerical investigation on the flow, combustion and NOx emission characteristics in a 500 MWe tangentially fired pulverized-coal boiler. *Fuel*, 88(9):1720 – 1731, 2009.

[27] T.J. Chung. *Computational Fluid Dynamics*. Cambridge University Press, 2002.

[28] Clayton T. Crowe, John D. Schwarzkopf, Martin Sommerfeld, and Yutaka Tsuji. *Multiphase flows with droplets and particles*. CRC Press, 2012.

[29] Marcio L. de Souza-Santos. *Solid Fuels Combustion and Gasification*. CRC Press, 2010.

[30] N.G. Deen, M. Van Sint Annaland, M.A. Van der Hoef, and J.A.M. Kuipers. Review of discrete particle modeling of fluidized beds. *Chemical Engineering Science*, 62(12):28 – 44, 2007. Fluidized Bed Applications.

[31] Colomba Di Blasi. Modeling chemical and physical processes of wood and biomass pyrolysis. *Progress in Energy and Combustion Science*, 34:47–90, 2008.

[32] J. K. Eaton and J. R. Fessler. Preferential concentration of particles by turbulence. *International Journal of Multiphase Flow*, 20:169–209, 1994.

[33] A. Elfasakhany, X.-S. Bai, B.G. Espenas, L. Tao, and J. Larfeldt. Effect of moisture and volatile release on motion of pulverised wood particles. In *Proceedings of the 7th International Conference on Energy for a Clean Environment, Lisbon, Portugal*, 2003.

[34] A. Elfasakhany, L. Tao, B. Espenas, J. Larfeldt, and X.S. Bai. Pulverised wood combustion in a vertical furnace: Experimental and computational analyses. *Applied Energy*, 112:454 – 464, 2013.

[35] S. Elghobashi and G. C. Truesdell. On the two-way interaction between homogeneous turbulence and dispersed solid particles. i: Turbulence modification. *Physics of Fluids*, A 5:1790–1801, 1993.

[36] Gregory Falkovich and Alain Pumir. Intermittent distribution of heavy particles in a turbulent flow. *Physics of Fluids*, 16(7):L47–L50, 2004.

[37] T. Fallon and C. B. Rogers. Turbulence-induced preferential concentration of solid particles in microgravity conditions. *Experiments in Fluids*, 33(2):233–241, 2002.

[38] Zhi-Gang Feng and Efstathios E. Michaelides. Unsteady heat and mass transfer from a spheroid. *AIChE Journal*, 43(3):609–614, 1997.

[39] A. Ferrante and S. Elgobashi. On the physical mechanisms of two-way coupling in particle-laden isotropic turbulence. *Physics of Fluids*, 15, 2003.

[40] Joel. H. Ferziger. *Computational Methods for Fluid Dynamics*. Springer Berlin Heidelberg, 2002.

[41] M.A. Field. Rate of combustion of size-graded fractions of char from a low-rank coal between 1 200k and 2 000k. *Combustion and Flame*, 13(3):237 – 252, 1969.

[42] Thomas H. Fletcher, Alan R. Kerstein, Ronald J. Pugmire, and David M. Grant. Chemical percolation model for devolatilization. 2. temperature and heating rate effects on product yields. *Energy & Fuels*, 4(1):54–60, 1990.

[43] B.M. Franchetti, F. Cavallo Marincola, S. Navarro-Martinez, and A.M. Kempf. Large eddy simulation of a pulverised coal jet flame. *Proceedings of the Combustion Institute*, 34(2):2419 – 2426, 2013.

[44] D. Gera, M. P. Mathur, M. C. Freeman, and Allen Robinson. Effect of large aspect ratio of biomass particles on carbon burnout in a utility boiler. *Energy & Fuels*, 16(6):1523–1532, 2002.

[45] GitHub. The pencil code, 2017.

[46] R.A. Gore and C.T. Crowe. Effect of particle size on modulating turbulent intensity. *International Journal of Multiphase Flow*, 15(2):279 – 285, 1989.

[47] Martin Gräbner. *Industrial Coal Gasification Technologies Covering baseline and High-Ash Coal*. Wiley-VCH, 2015.

[48] P. Gualtieri, F. Picano, G. Sardina, and C.M. Casciola. Clustering and turbulence modulation in particle laden shear flows. *Particles in Turbulence*, 333, 2011.

[49] Mike Guidry. Algebraic stabilization of explicit numerical integration for extremely stiff reaction networks. *Journal of Computational Physics*, 231(16):5266 – 5288, 2012.

[50] Y.C. Guo, C.K. Chan, and K.S. Lau. Numerical studies of pulverized coal combustion in a tubular coal combustor with slanted oxygen jet. *Fuel*, 82(8):893 – 907, 2003.

[51] A. Habibi, B. Merci, and G.J. Heynderickx. Impact of radiation models in CFD simulations of steam cracking furnaces. *Computers & Chemical Engineering*, 31(11):1389 – 1406, 2007.

[52] Takumi Hara, Masaya Muto, Tomoaki Kitano, Ryoichi Kurose, and Satoru Komori. Direct numerical simulation of a pulverized coal jet flame employing a global volatile matter reaction scheme based on detailed reaction mechanism. *Combustion and Flame*, 162(12):4391 – 4407, 2015.

[53] Nozomu Hashimoto and Hiroaki Watanabe. Numerical analysis on effect of furnace scale on heat transfer mechanism of coal particles in pulverized coal combustion field. *Fuel Processing Technology*, 145:20 – 30, 2016.

[54] Nils E.L. Haugen, Jonas Krüger, Dhrubaditya Mitra, and Terese Løvås. The effect of turbulence on mass and heat transfer rates of small inertial particles. *J. Fluid Mech (submitted)*, 2017.

[55] Nils Erland L. Haugen, Reginald E. Mitchell, and Matthew B. Tilghman. A comprehensive model for char particle conversion in environments containing O2 and CO2. *Combustion and Flame*, 162(4):1455 – 1463, 2015.

[56] Nils Erland L. Haugen, Matthew B. Tilghman, and Reginald E. Mitchell. The conversion mode of a porous carbon particle during oxidation and gasification. *Combustion and Flame*, 161(2):612 – 619, 2014.

[57] Brian S. Haynes. A turnover model for carbon reactivity i. development. *Combustion and Flame*, 126(12):1421 – 1432, 2001.

[58] Ethan S. Hecht, Christopher R. Shaddix, Manfred Geier, Alejandro Molina, and Brian S. Haynes. Effect of CO2 and steam gasification reactions on the oxy-combustion of pulverized coal char. *Combustion and Flame*, 159(11):3437 – 3447, 2012.

[59] Ethan S. Hecht, Christopher R. Shaddix, Alejandro Molina, and Brian S. Haynes. Effect of CO2 gasification reaction on oxy-combustion of pulverized coal char. *Proceedings of the Combustion Institute*, 33(2):1699 – 1706, 2011.

[60] Mohammad M. Hossain and Hugo I. de Lasa. Chemical-looping combustion CLC for inherent separations-a review. *Chemical Engineering Science*, 63(18):4433 – 4451, 2008.

[61] Seung min Hwang, Ryoichi Kurose, Fumiteru Akamatsu, Hirofumi Tsuji, Hisao Makino, and Masashi Katsuki. Application of optical diagnostics techniques to a laboratory-scale turbulent pulverized coal flame. *Energy & Fuels*, 19(2):382–392, 2005.

[62] J. Hlie and A. Trouv. A modified coherent flame model to describe turbulent flame propagation in mixtures with variable composition. *Proceedings of the Combustion Institute*, 28(1):193 – 201, 2000.

[63] International Energy Agency. World energy outlook 2016, December 2016.

[64] International Monetary Fund. World economic outlook update, july 2016, July 2016 2016.

[65] W.P Jones and B.E Launder. The prediction of laminarization with a two-equation model of turbulence. *International Journal of Heat and Mass Transfer*, 15(2):301 – 314, 1972.

[66] Toshiaki Kabe, Atsushi Ishihara, Eika Weihua Qian, I Putu Sutrisna, and Yaeko Kabe. *Coal and Coal-Related Compounds Structures, Reactivity and Catalytic Reactions*, volume 150 of *Studies in Surface Science and Catalysis*. Elsevier, 2004.

[67] E. Karampinis, N. Nikolopoulos, A. Nikolopoulos, P. Grammelis, and E. Kakaras. Numerical investigation greek lignite/cardoon co-firing in a tangentially fired furnace. *Applied Energy*, 97:514 – 524, 2012. Energy

Solutions for a Sustainable World - Proceedings of the Third International Conference on Applied Energy, May 16-18, 2011 - Perugia, Italy.

[68] Robert J. Kee, Fran M. Rupley, and Ellen Meeks. *Chemkin-III: A Fortran chemical kinetics package for the analysis of gas- phase chemical and plasma kinetics*. Thermal and Plasma Processes Department, Sandia National Laboratories, Livermore, CA 94551-0969, 1996.

[69] Alan R. Kerstein, William T. Ashurst, and Forman A. Williams. Field equation for interface propagation in an unsteady homogeneous flow field. *Phys. Rev. A*, 37:2728–2731, Apr 1988.

[70] John Kim, Parviz Moin, and Robert Moser. Turbulence statistics in fully developed channel flow at low reynolds number. *J. Fluid Mech*, 177:133–166, 1987.

[71] A. Yu. Klimenko. Multicomponent diffusion of various admixtures in turbulent flow. *Fluid Dynamics*, 25(3):327–334, 1990.

[72] M. Komatina, V. Manovic, and A. Saljnikov. A model of coal particle drying in fluidized bed combustion reactor. *Energy Sources, Part A: Recovery, Utilization, and Environmental Effects*, 29(3):239–250, 2007.

[73] Jonas Krüger, Nils E.L. Haugen, Terese Løvås, and Dhrubaditya Mitra. A study on the coupling between isotropic turbulence and heterogeneous reactions. In Bjørn Skallerud and Helge I. Andersson, editors, *Proceedings of MekIT'15 Eighth National Conference on Computational Mechanics*, volume 8, pages 243–257, 2015.

[74] Jonas Krger, Nils E.L. Haugen, and Terese Lvs. Correlation effects between turbulence and the conversion rate of pulverized char particles. Submitted to *Combustion & Flame*, 2017.

[75] Jonas Krger, Nils E.L. Haugen, Dhrubaditya Mitra, and Terese Lvs. The effect of turbulent clustering on particle reactivity. *Proceedings of the Combustion Institute*, 36(2):2333 – 2340, 2017.

[76] J.A.M. Kuipers and W.P.M. van Swaaij. Computational fluid dynamics applied to chemical reaction engineering. In *Computational Fluid Dynamics Applied To Chemical Reaction Engineering*, volume 24 of *Advances in Chemical Engineering*, pages 227 – 328. Academic Press, 1998.

[77] Joanna Lazar, Nils Erland L. Haugen, Jonas Kruger, and Andrzej Szlek. Numerical study of hydrogen inhibition of char gasification using detailed hetero- and homogeneous chemical kinetics. *Energy & Fuels*, 30(6):4411–4418, 2016.

[78] Octave Levenspiel. *Chemical reaction engineering*. John Wiley & Sons, 1999.

[79] Tian Li, Manfred Geier, Liang Wang, Xiaoke Ku, Berta Matas Gell, Terese Lvs, and Christopher R. Shaddix. Effect of torrefaction on physical properties and conversion behavior of high heating rate char of forest residue. *Energy & Fuels*, 29(1):177–184, 2015.

[80] Andrei Lipatnikov. *Fundamentals of Premixed Turbulent Combustion*. CRC Press, 2013.

[81] F.C. Lockwood and C. A. Romo-Millanes. Mathematical modelling of fuel NO emissions from PF burners. *International Journal of Energy Research*, 65:144–152, 1992.

[82] Rainald Löhner. *Applied computational fluid dynamics techniques*. Wiley, 2008.

[83] Terese Løvås, Ehsan Houshfar, Mette Bugge, and Øyvind Skreiberg. Automatic generation of kinetic skeletal mechanisms for biomass combustion. *Energy & Fuels*, 27(11):6979–6991, 2013.

[84] Terese Løvås, Nadeem Malik, and Fabian Mauss. Global reaction mechanism for ethylene flames with preferential diffusion. *Combustion Science and Technology*, 182(11-12):1945–1960, 2010.

[85] Kun Luo, Haiou Wang, Jianren Fan, and Fuxing Yi. Direct numerical simulation of pulverized coal combustion in a hot vitiated co-flow. *Energy & Fuels*, 26(10):6128–6136, OCT 2012.

[86] L. Ma, M. Gharebaghi, R. Porter, M. Pourkashanian, J.M. Jones, and A. Williams. Modelling methods for co-fired pulverised fuel furnaces. *Fuel*, 88(12):2448 – 2454, 2009. 7th European Conference on Coal Research and Its Applications.

[87] L. Ma, J.M. Jones, M. Pourkashanian, and A. Williams. Modelling the combustion of pulverized biomass in an industrial combustion test furnace. *Fuel*, 86(1213):1959 – 1965, 2007.

[88] Bjørn Magnussen and Bjørn Hjertager. On mathematical models of turbulent combustion with special emphasis on soot formation and combustion. *Proceedings of the Combustion Institute*, 16(1):719729, 1979.

[89] Matthias Mand and Lasse Rosendahl. On the motion of non-spherical particles at high reynolds number. *Powder Technology*, 202(13):1 – 13, 2010.

[90] Martin R. Maxey and James J. Riley. Equation of motion for a small rigid sphere in a nonuniform flow. *The Physics of Fluids*, 26(4):883–889, 1983.

[91] E. E. Michaelides. *Particles, Bubbles, and Drops: Their Motion, Heat and Mass Transfer*. World Scientific, 2006.

[92] Seung min Hwang, Ryoichi Kurose, Fumiteru Akamatsu, Hirofumi Tsuji, Hisao Makino, and Masashi Katsuki. Observation of detailed structure of turbulent pulverized-coal flame by optical measurement. *JSME International Journal Series B Fluids and Thermal Engineering*, 49(4):1316–1327, 2006.

[93] Reginald E. Mitchell, Liqiang Ma, and BumJick Kim. On the burning behavior of pulverized coal chars. *Combustion and Flame*, 151(3):426 – 436, 2007.

[94] Alejandro Molina and Christopher R. Shaddix. Ignition and devolatilization of pulverized bituminous coal particles during oxygen/carbon dioxide coal combustion. *Proceedings of the Combustion Institute*, 31(2):1905 – 1912, 2007.

[95] Gordon E. Moore. Cramming more components onto integrated circuits. *Electronics*, 38, 1965.

[96] P. Nikrityuk and B. Meyer. *Gasification Processes*. Wiley, 2014.

[97] P.A. Nikrityuk, M. Grbner, M. Kestel, and B. Meyer. Numerical study of the influence of heterogeneous kinetics on the carbon consumption by oxidation of a single coal particle. *Fuel*, 114:88 – 98, 2013. Advances in Coal Science and Technology, ICCS&T 2011.

[98] Stephen Niksa and Alan R. Kerstein. Flashchain theory for rapid coal devolatilization kinetics. 1. formulation. *Energy & Fuels*, 5(5):647–665, 1991.

[99] NORDITA. Pencil Code research usage, February 2017. Available at `http://norlx51.nordita.org/~brandenb/tmp/citations/notes.pdf`.

[100] W. Nusselt. Der Verbrennungsvorgang in der Kohlenstaubfeuerung. *Zeitschrift des Vereins Deutscher Ingenieure*, 68:124, 1924.

[101] G. Olenik, O.T. Stein, and A. Kronenburg. Les of swirl-stabilised pulverised coal combustion in IFRF furnace no. 1. *Proceedings of the Combustion Institute*, 35(3):2819 – 2828, 2015.

[102] Bernhard Peters and Christian Bruch. Drying and pyrolysis of wood particles: experiments and simulation. *Journal of Analytical and Applied Pyrolysis*, 70(2):233 – 250, 2003.

[103] N. Peters. Laminar flame concepts in turbulent combustion. *Proceedings of the Combustion Institute*, 21:1231–50, 1986.

[104] Thierry Poinsot and Denis Veynante. *Theoretical and Numerical Combustion*. Poinsot and Veynante, 2012.

[105] S.B. Pope. The evolution of surfaces in turbulence. *International Journal of Engineering Science*, 26(5):445 – 469, 1988.

[106] Stephen B. Pope. *Turbulent Flows*. Cambridge University Press, 2000.

[107] W. E. Ranz and W. R. Marshall. Evaporation from drops. *Chemical Engineering Progress*, 48:141–146, 1952.

[108] J. Reveillon and F.X. Demoulin. Evaporating droplets in turbulent reacting flows. *Proceedings of the Combustion Institute*, 31(2):2319 – 2326, 2007.

[109] M. Rieth, A.G. Clements, M. Rabaal, F. Proch, O.T. Stein, and A.M. Kempf. Flamelet LES modeling of coal combustion with detailed devolatilization by directly coupled CPD. *Proceedings of the Combustion Institute*, pages –, 2016.

[110] Pierre Sagaut. *Large Eddy Simulation for Incompressible Flows: An Introduction*. Springer, 1998.

[111] Schiller and Naumann. Über die grundlegenden berechnungen bei der schwerkraftaufbereitung. *Verein Deutscher Ingenieure*, 77:318, 1933.

[112] L. Selle, G. Lartigue, T. Poinsot, R. Koch, K.-U. Schildmacher, W. Krebs, B. Prade, P. Kaufmann, and D. Veynante. Compressible large eddy simulation of turbulent combustion in complex geometry on unstructured meshes. *Combustion and Flame*, 137(4):489 – 505, 2004.

[113] Gregory P. Smith, David M. Golden, Michael Frenklach, Nigel W. Moriarty, Boris Eiteneer, Mikhail Goldenberg, C. Thomas Bowman, Ronald K. Hanson, Soonho Song, William C. Gardiner, Jr., Vitali V. Lissianski, and Zhiwei Qin. GRI-Mech 3.0 Homepage, August 2014. Available at `http://combustion.berkeley.edu/Combustion_Laboratory/gri-mech/overview.html`.

[114] I.W. Smith. The combustion rates of coal chars: A review. *Symposium (International) on Combustion*, 19(1):1045 – 1065, 1982. Nineteenth Symposium (International) on Combustion.

[115] Samuele Sommariva, Tiziano Maffei, Gabriele Migliavacca, Tiziano Faravelli, and Eliseo Ranzi. A predictive multi-step kinetic model of coal devolatilization. *Fuel*, 89(2):318 – 328, 2010.

[116] DB Spalding. Mixing and chemical reaction in steady confined turbulent flames. *Proceedings of the Combustion Institute*, pages 649–657, 1971.

[117] K. D. Squires and J. K. Eaton. Particle response and turbulence modification in isotropic turbulence. *Physics of Fluids*, 7:1191–12–3, 1990.

[118] O. T. Stein, G. Olenik, A. Kronenburg, F. Cavallo Marincola, B. M. Franchetti, A. M. Kempf, M. Ghiani, M. Vascellari, and C. Hasse. Towards comprehensive coal combustion modelling for les. *Flow, Turbulence and Combustion*, 90(4):859–884, 2013.

[119] G.G. Stokes. On the effect of internal friction of fluids on the motion of a pendulum. *Transactions of the Cambridge Philisophical Society*, 9:8, 1891.

[120] Shivshankar Sundaram and Lance R. Collins. Numerical considerations in simulating a turbulent suspension of finite-volume particles. *Journal of Computational Physics*, 124(2):337 – 350, 1996.

[121] Ernest W. Thiele. Relation between catalytic activity and size of particle. *Ind. Eng. Chem.*, 31:916–920, 1939.

[122] Matthew B. Tilghman and Reginald E. Mitchell. Coal and biomass char reactivities in gasification and combustion environments. *Combustion and Flame*, 162(9):3220 – 3235, 2015.

[123] G.L. Tufano, O.T. Stein, A. Kronenburg, A. Frassoldati, T. Faravelli, L. Deng, A.M. Kempf, M. Vascellari, and C. Hasse. Resolved flow simulation of pulverized coal particle devolatilization and ignition in air- and o2/co2-atmospheres. *Fuel*, 186:285 – 292, 2016.

[124] Markus Uhlmann. An immersed boundary method with direct forcing for the simulation of particulate flows. *Journal of Computational Physics*, 209:448–476, 2005.

[125] M.A. van der Hoef, M. van Sint Annaland, N.G. Deen, and J.A.M. Kuipers. Numerical simulation of dense gas-solid fluidized beds: A multiscale modeling strategy. *Annual Review of Fluid Mechanics*, 40:47–70, 2008.

[126] Martin A. van der Hoef, Daan Frenkel, and Anthony J. C. Ladd. Self-diffusion of colloidal particles in a two-dimensional suspension: Are deviations from fick's law experimentally observable? *Phys. Rev. Lett.*, 67:3459–3462, Dec 1991.

[127] M. Vascellari, H. Xu, and C. Hasse. Flamelet modeling of coal particle ignition. *Proceedings of the Combustion Institute*, 34(2):2445 – 2452, 2013.

[128] L. Vervisch, E. Bidaux, K. N. C. Bray, and W. Kollmann. Surface density function in premixed turbulent combustion modeling, similarities between probability density function and flame surface approaches. *Physics of Fluids*, 7(10):2496–2503, 1995.

[129] Denis Veynante and Luc Vervisch. Turbulent combustion modeling. *Progress in Energy and Combustion Science*, 28(3):193 – 266, 2002.

[130] K.M. Waananen, J.B. Litchfield, and M.R. Okos. Classification of drying models for porous solids. *Drying Technology*, 11(1):1–40, 1993.

[131] A. M. Wood, W. Hwang, and J. K. Eaton. Preferential concentration of particles in homogeneous and isotropic turbulence. *International Journal of Multiphase Flow*, 31:1220–1230, 2005.

[132] H. Yamashita, M. Shimada, and T. Takeno. A numerical study on flame stability at the transition point of jet diffusion flames. *Symposium (International) on Combustion*, 26(1):27 – 34, 1996.

[133] Chungen Yin, Lasse A. Rosendahl, and Sren K. Kr. Grate-firing of biomass for heat and power production. *Progress in Energy and Combustion Science*, 34(6):725 – 754, 2008.

[134] M.C. Yuen and L.W. Chen. On drag of evaporating liquid droplets. *Combustion Science and Technology*, 14:147, 1976.

[135] Lihao Zhao and Helge I. Andersson. Why spheroids orient preferentially in near-wall turbulence. *Journal of Fluid Mechanics*, 807:221–234, 11 2016.

[136] Lihao Zhao, Niranjan Reddy Challabotla, Helge I. Andersson, and Evan A. Variano. Rotation of nonspherical particles in turbulent channel flow. *Phys. Rev. Lett.*, 115:244501, Dec 2015.

Chapter 5

Papers

5.1 Paper 1

A study on the coupling between isotropic turbulence and heterogenous reactions

Jonas Krüger, Nils E. L. Haugen, Terese Løvås and Dhrubaditya Mitra
Published in the Proceedings of the 8th national conference on Computational Mechanics 2015:243-257

8. National Conference on Computational Mechanics
MekIT'15
B. Skallerud and H I Andersson (Eds)

A STUDY ON THE COUPLING BETWEEN ISOTROPIC TURBULENCE AND HETEROGENEOUS REACTIONS

Jonas Krüger[1], **Nils E. L. Haugen**[2], **Terese Løvås**[1] **and Dhrubaditya Mitra**[3]

[1] *NTNU EPT, Trondheim, Norway*
[2] *SINTEF Energy Research, NO-7465 Trondheim, Norway*
[3] *Nordita, KTH Royal Institute of Technology and Stockholm University, Roslagstullsbacken 23, SE-10691 Stockholm, Sweden*

Key words: DNS, Particle Clustering, Passive Scalar, Heterogeneous Reaction

Abstract. The effect of turbulence and particle clustering on the decay rate of a chemically reacting scalar is studied with direct numerical simulations (DNS). The scalar is consumed on the surface of the particles. When the chemical timescale is of the same order or less than the particle time scale, particle clustering slows down the scalar decay rate. This effect is present for all turbulence intensities and particle Stokes numbers, as long as the Damköhler number is sufficiently large. For the present studies, turbulent diffusivity plays a minor role in comparison to the molecular diffusivity.

1 Introduction

Coal based fossil energy production will continue to play a major role in the foreseeable future [1]. Therefore, strong efforts to improve its efficiency and decrease its environmental impact through computer aided design are required. This calls for a solid understanding of the multitude of processes involved. The main processes during fossil fuel energy production are flow turbulence, radiation and homogeneous and heterogeneous reactions. The industry already uses a wide span of models for flow turbulence of different levels of detail, and more sophisticated and costly models become usable as the available computers become cheaper and faster.
Reynolds-averaged Navier Stokes (RANS) studies using different submodels for the Reynolds stress term such as $k-\epsilon$ or Reynolds stress modeling (RSM) are used together with global homogeneous and heterogeneous mechanisms to simulate the performance of an actual gasifier [2]. Since the RANS approach does not compute the instantaneous velocities, the particles were dispersed using a stochastic tracking scheme. This scheme only influences the trajectory of the particle, having no direct effect on the reaction rate.
The group of Abani uses Large Eddy Simulation (LES) with a three-step heterogeneous mechanism to simulate coal gasification [3]. They account for the interaction between fluid and solid via a moving flame front model, where the overall heterogeneous reaction rate is a combination of a kinetic rate given

Corresponding author: jonas.kruger@ntnu.no

by an Arrhenius expression and a diffusion rate dependent on the temperature between the particle and the surrounding fluid. Results include temperatures, species mass fractions and particle distribution in a coal-oxygen jet which are then compared with lab-scale gasifier measurements. It has to be noted that the usage and sophistication of LES tools is expected to increase [4] [5]. Even a Direct Numerical Simulation (DNS) of pulverized coal flames with a three-step char reaction mechanism, Reynolds numbers up to 28,000 and accounting for devolatilization is reported by the group of Luo et al. [6]. They obtained for example heat release rates and particle distributions at different planes along a pulverized jet flame and compared against experiments.

Chemical mechanisms and models for homogeneous combustion in turbulent flows are widespread and cover the range of combustion regimes, from laminar to turbulent and from non-premixed to premixed flames [7], [8]. It is apparent that the field of heterogeneous combustion modeling has not seen as extensive development as its homogeneous counterpart.

In all of the studies mentioned, the effect of turbulence on the particles trajectory is accounted for, either by a model [2] or directly by the instantaneous velocity of the fluid [6]. The coupling of flow turbulence, resulting clustering and heterogeneous reaction rates at the surface of particles are not looked at due to the inability of the employed model to capture clustering (except in the work of Luo [6]). This study aims at providing some insight into how particles cluster depending on flow attributes in a flow with no preferential direction, and how this influences the fluid-solid interaction. Especially the resulting overall reaction rates when particles form dense clusters and rapidly consume fluid reactants inside are looked at and upper boundaries for these reaction rates are reported. This is done to work towards a heterogeneous combustion model for RANS or LES Computational Fluid Dynamics (CFD) that accounts for two-phase flows with varying particle number densities, particle compositions and turbulence intensities in one domain.

The system analysed is very simple to reduce computational cost and to avoid secondary effects from other flow attributes such as temperature, changing diffusivities and reaction paths. The complexity of the flow can be increased when the basic laws governing the heterogeneous reactions are better understood.

2 Theory

We look at a simple isothermal flow field with isotropic turbulence that is governed by the continuity equation

$$\frac{\mathrm{D}\rho}{\mathrm{D}t} = -\rho \boldsymbol{\nabla} \cdot \boldsymbol{u} \tag{1}$$

and momentum equation

$$\rho \frac{\mathrm{D}\boldsymbol{u}}{\mathrm{D}t} = -\boldsymbol{\nabla} P + \boldsymbol{\nabla} \cdot (2\mu \boldsymbol{S}) - \frac{1}{V} \sum_i \boldsymbol{F}_{p,i} \tag{2}$$

with ρ being the gas density, $\boldsymbol{u}$ the velocity, t time, μ viscosity, P pressure, V the volume of one grid cell and $\sum_i \boldsymbol{F}_{p,i}$ the sum of the friction forces of all particles in the grid cell. The traceless rate of strain tensor $\boldsymbol{S}$ evaluates to

$$\boldsymbol{S} = \frac{1}{2} \left(\boldsymbol{\nabla} \boldsymbol{u} + (\boldsymbol{\nabla} \boldsymbol{u})^T \right) - \frac{1}{3} \boldsymbol{\nabla} \cdot \boldsymbol{u}. \tag{3}$$

In isothermal conditions the pressure is connected to the density via the speed of sound, c_s, as:

$$P = c_s^2 \rho. \tag{4}$$

The evolution of the molar fraction X_∞ of a passive scalar θ is given by

$$\frac{\partial X_\infty C_g}{\partial t} + \nabla \cdot (X_\infty C_g \boldsymbol{u}) = \nabla \cdot (\rho D \nabla X_\infty) + \tilde{R}, \tag{5}$$

with D being the diffusivity, C_g the gas concentration in mole/cm^3 and $\tilde{R}$ a sink term, in this case only due to consumption of species θ on the surface of particles. Assuming constant gas concentration and rewriting the Lagrangian derivative $\frac{D}{Dt} = \frac{\partial}{\partial t} + \boldsymbol{u}\cdot$, (5) simplifies to

$$\frac{DX_\infty}{Dt} = \frac{1}{C_g} \nabla \cdot (\rho D \nabla X_\infty) + R, \tag{6}$$

where $R = \frac{\tilde{R}}{C_g}$.

2.1 Particle movement

The particles are assumed to be much smaller than a grid cell and therefore treated as point particles. Each particle is tracked using a Lagrangian approach, and changes in the particle velocity $\boldsymbol{v}$ due to the force $\boldsymbol{F}_p$ acting on the particles are given by

$$\frac{\mathrm{d}\boldsymbol{v}}{\mathrm{d}t} = \frac{\boldsymbol{F}_p}{m_p}, \tag{7}$$

with m_p being the particles mass. The particle position $\boldsymbol{x}$ is then calculated accordingly to

$$\frac{\mathrm{d}\boldsymbol{x}}{\mathrm{d}t} = \boldsymbol{v}. \tag{8}$$

In this study, the only force on the particle is the drag force

$$\boldsymbol{F}_p = \frac{1}{2} \rho C_D A |\boldsymbol{u} - \boldsymbol{v}| (\boldsymbol{u} - \boldsymbol{v}), \tag{9}$$

with A being the cross section of the particle and $|\boldsymbol{u} - \boldsymbol{v}|$ the particles velocity relative to the gas flow. The drag coefficient C_D is obtained following the Schiller-Naumann correlation [9]

$$C_D = \frac{24}{\mathrm{Re}_p}(1 + 0.15\mathrm{Re}_p^{0.687}) \tag{10}$$

which is valid for particle Reynolds numbers up to 800. The particle Reynolds number is $\mathrm{Re}_p = d_p|\boldsymbol{v} - \boldsymbol{u}|/\nu$, with $d_p = 2r_p$ being the particle diameter and ν the kinematic viscosity of the flow.

2.2 Heterogeneous reactions

We look at a simplified surface reaction system where a gas phase species θ is converted into the same amount of species γ at the particle surface, and only there. The reaction is isothermal, unimolar and only governed by the prescribed consumption rate. This can be seen as the isothermal oxygen consumption and carbon dioxide production at the surface of everlasting coal particles. The particle surface specific molar consumption rate $\dot{n}$ of species θ is

$$\dot{n} = -\lambda X_s C_g \tag{11}$$

with λ being the volumetric consumption rate of θ at the particles surface, C_g the overall gas concentration and X_s the molar fraction of species θ in the gas at the particles surface. This consumption is compensated by species θ diffusing to the particles surface from far away in the gas phase where θ has a molar fraction of X_∞. This diffusion rate is governed by

$$\dot{n} = -k(X_\infty - X_s). \tag{12}$$

The mass transfer coefficient is given by $k = C_g D\mathrm{Sh}/2r_p$, where Sh is the Sherwood number. The Sherwood number is set to a constant value of 2, assuming quiescent fluid around the particle. This results in a lower mass transfer coefficient for particles that have a high relative velocity in respect to the gas. In this study, it is found that the particles Reynolds number never exceeds 5, which yields an upper limit for the underprediction of mass transfer by 50% according to the Ranz-Marshall correlation in reference [9].
Eqs. (11) and (12) can be combined to give the surface concentration for steady state as

$$X_s = \frac{kX_\infty}{C_g + \lambda k} \tag{13}$$

which can be inserted back into (11) to yield

$$\dot{n} = \tilde{\lambda} X_\infty C_g, \tag{14}$$

with $\tilde{\lambda} = \frac{\lambda k}{\lambda C_g + k}$ being the adapted consumption rate taking into account diffusion and consumption of θ. The source term in (5) is now given by

$$\tilde{R} = \frac{1}{V_c} \sum_{i=1}^{N_p} \dot{n}_i A_{p,i}, \tag{15}$$

where $A_p = 4\pi r_p^2$ is the particle surface area, V_c the grid cell volume and N_p the number of particles present in the grid cell. Combining (14) and (15) yields

$$R = \frac{-1}{V_c} \sum_{i=1}^{N_p} \tilde{\lambda} X_\infty A_{p,i} \tag{16}$$

for the source term in (6).

2.3 Solution for homogeneous particle distribution

Averaging (6) over the entire volume of the domain for a homogeneous, non moving distribution of particles yields the following equation for the evolution of the mean mole fraction of θ in the flow field:

$$\frac{d\bar{X}_\infty}{dt} = -n_p \tilde{\lambda} \bar{X}_\infty \bar{A}_p \tag{17}$$

with n_p being the particle number density in the domain. Eq. (17) has the analytical solution

$$\bar{X}_\infty(t) = X_{\infty,0} \exp(-\alpha_p t), \tag{18}$$

with

$$\alpha_p = n_p \tilde{\lambda} \bar{A}_p \tag{19}$$

being the decay rate of the molar fraction X_∞ of θ.

2.4 The Stokes and Damköhler number

The Stokes number is the ratio of the particle time scale $\tau_p = S d_p^2 / 18\nu$ (also called particle stopping time) and the flow time scale $\tau_i = L_f / u_{rms}$. Particles are most efficiently captured by eddies of a similar time scale. For Stokes numbers < 1, the particles follow smaller eddies, leading to a clustering on smaller scales and therefore a smoother distribution in the flow field, while particles with Stokes numbers > 1 follow eddies larger than the integral scale. From τ_p and τ_i we can construct the particle Stokes number based on the scale of the energy containing eddies,

$$\mathrm{St}_i = \frac{\tau_p}{\tau_i} = \frac{S d_p^2 u_{rms}}{18 \nu L_f}. \tag{20}$$

The particle stopping time is composed of the density ratio $S = \rho_{particle} / \rho_{fluid}$, the particles diameter d_p and the flow viscosity ν. The flow time scale τ_i is here defined with u_{rms} being the root mean square velocity of the flow field in statistically steady state and L_f the integral scale of the flow turbulence.
The chemical time scale τ_c (in which a significant change in the amount of θ is experienced) is given by the inverse of the decay rate for homogeneous particle distributions from (19),

$$\tau_c = \frac{1}{\alpha_p} = \frac{1}{n_p \tilde{\lambda} A_p}. \tag{21}$$

In order for the particle clustering to have a significant effect on the consumption rate, it is required that $\tau_c \leq \tau_p$. Based on the above, we define the relevant Damköhler number Da, which is the ratio of a flow time scale and the chemical time scale [10]. In our case the relevant flow time scale is the time scale of the particles τ_p, since this is the scale at which particle reactions occur. The chemical time scale is still the inverse of the decay rate α. This is a significant difference from the case of homogeneous reactions, where usually the small (and fast) turbulence scales are responsible for mixing the reactants ([7], [10]).

The Damköhler number is now

$$\mathrm{Da} = \frac{\tau_p}{\tau_c} = \frac{Sd^2 n_p \tilde{\lambda} A_p}{18\nu} = \frac{2}{3}\frac{\overline{V}_p \tilde{\lambda} r_p S}{\nu}, \tag{22}$$

where $\overline{V}_p = \frac{4}{3}\pi r_p^3 n_p$ is the volume fraction of the particles. For the diffusion controlled regime (i.e. $\lambda C_g \gg k$), where the surface consumption rate is magnitudes higher than the diffusion rate, the Damköhler number can also be written as

$$\mathrm{Da}_{\mathrm{diff.}} = \lim_{\lambda\to\infty} \mathrm{Da} = \frac{4Sr_p^2 n_p k A_p}{18\nu\overline{C_g}} = \frac{1}{3}\frac{\overline{V}_p S\mathrm{Sh}}{\mathrm{Sc}} = \frac{2\pi r_p n_p D\mathrm{ShSt}_i}{u_{\mathrm{rms}} k_f}, \tag{23}$$

where Sc is the Schmidt number defined as the ratio ν/D of the viscosity ν and the molecular diffusion coefficient D [11]. For the present study, there are two possibilities to increase the Damköhler number to higher values while holding the Stokes number constant. The most straightforward is increasing the particle number density, i.e. increasing the number of particles. Another possibility is to increase the particles radius while decreasing the particle density by the quadratic amount. In this way, the particle stopping time and the particle Stokes number is held constant, while the Damköhler number from (23) is changed. This approach is chosen for the highest Damköhler numbers. Since $m_{particle} \sim d^3\rho$, an increase in particle diameter results in a linear increase in mass loading, similar to the increase in the number of particles, so both ways of increasing the Damköhler number have the same effect on the mass loading. Increasing the diameter over a certain amount means violating the assumption of point particles for a small number of cells which is discussed in the results section 4.

3 Study setup and studied parameters

In this study, the influence of the Damköhler number on the decay rate of a passive scalar is analysed. To do this, cases are set up where a particle-laden flow field is simulated using the open-source CFD software Pencil Code [12]. This code uses a sixth-order central difference scheme for spatial derivatives and a third-order, two stage Runge-Kutta scheme for time stepping [13].
Kinetic energy is inserted into the fully periodic domain of the simulations at large scales (close to the domain size) through a forcing function with a wavenumber of k_f. This yields turbulence without dominant directions. To compare the cases against each other, a number of non-dimensional parameters are defined, some of whom are varied while holding the others constant. The flow Reynolds number is defined as

$$\mathrm{Re} = \frac{u_{\mathrm{rms}} L_f}{\nu}. \tag{24}$$

The same forcing is used in all cases, holding the flow Reynolds number at around 300. Here, cases with two different Stokes numbers, 0.33 and 1.0 based on (20) are simulated. Table 1 shows the initial and boundary conditions used in the study. The grid spacing Δx divided by the Kolmogorov length scale $\eta = (\nu^3/\epsilon)^{\frac{1}{4}}$ and the particle diameter d_p can be found in table 2. The Kolmogorov scale for this flow is

of the order of $2 \cdot 10^{-4}$m, while the grid spacing is $\Delta x \approx 10^{-3}$m for the cases with the lowest resolution. An overview over the study setup can be found in tables 1 and 2. This grid spacing resolves all the the energy containing scales and all but the very smallest dissipative scales. However, since the lowest resolution is used for cases where the particle loading of the flow is low, no secondary effects of the small scale turbulence are expected, making an imperfect representation of the flow turbulence feasible. Figure 2 shows the turbulent energy spectrum of runs with different resolutions. All resolutions resolve the relevant scales of the flow.

Table 1: Boundary and initial conditions

Flow attribute	Value	Unit
$L_x = L_y = L_z$	6.28	[cm]
$N_x = N_y = N_z$	64,128,256	[-]
D	1x10^{-3}	[cm^2/s]
ν	2x10^{-4}	[cm^2/s]
N_{part}	50k-1.25M	[-]
d_{part}	30-120	[μm]
$\rho_{\text{part}}/\rho_{\text{fluid}}$	14-220	[-]
Δt	10-50	[ms]
τ_η	2.5x10^{-1}	[s]

Table 2: Grid spacing Δx divided by the Kolmogorov scale η and the default particle diameter $d_p = 50\mu$m

Resolution	$\frac{\Delta x}{\eta}$	$\frac{\Delta x}{d_p}$
64^3	5.0	32
128^3	2.5	16
256^3	1.25	8

All cases are initialized and then allowed to reach a statistically steady state, at which point the concentration of the passive scalar θ is set to 1.0 throughout the domain. The mean concentration X_∞ of species θ is sampled after that. Figure 1 shows the root mean square velocity over time for cases that are only different in resolution. Data is collected 600 seconds after initialization, which is deemed sufficient to reach quasi steady state for all resolutions, as all simulations show no signs of the startup behaviour after 200 seconds. Resulting energy spectra can be seen in figure 2. The spectra are identical in the energy containing scales with slight differences in regions of high wave numbers. In the wave numbers of the scales where clustering is analysed, there is only slightly more dissipation in cases with the coarsest resolution at high wave numbers. Together with the smooth transport of turbulent energy down the cascade without any filtering, all resolutions are deemed sufficient to resolve the relevant scales for the flow phenomena studied in this work.

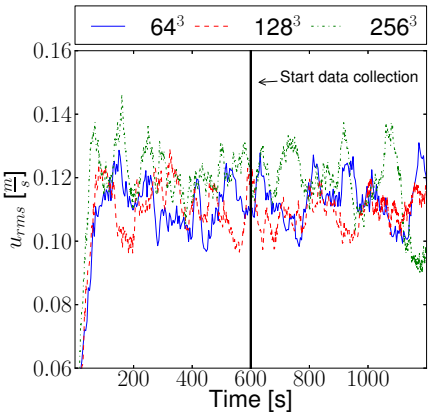

Figure 1: Root mean square of velocity in the domain for different resolutions plotted over time. At the start of data collection, all flows have reached statistically steady state.

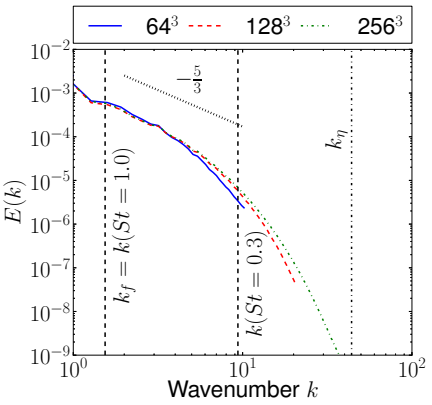

Figure 2: Turbulent energy spectra plotted for three cases with different resolution. All cases have sufficient resolution for the flow attributes studied.

3.1 Decay rate

The passive scalar decay rate can be obtained from the evolution of the averaged concentration of θ from the simulations. For all simulations, a fit using an exponential decay corresponds well with the data for all times. The volume averaged values of θ over time and its fit using a exponential function for different cases with a Stokes number of 1 and $D = 10^{-3}m^2/s$ can be seen in figure 3. A higher Damköhler number results in a faster decay rate and stronger divergence from the exponential decay.

3.2 Decay rate for small Damköhler numbers

In the range of small Damköhler numbers, the particle clustering has no effect on the decay rate, since the particle number density inside the clusters is low. Accordingly, the rate can be calculated directly with (19). This can be inserted into (22) to yield

$$\alpha_p = \frac{\mathrm{Da}}{\tau_p}, \tag{25}$$

which means that for sufficiently small Damköhler numbers, the decay rate will scale linearly with Da, i.e. number of particles present in the domain.

3.3 Decay rate for large Damköhler numbers

For large Damköhler numbers, meaning a high number of particles, the particle number density inside the clusters is very high, so that internal θ is rapidly consumed. The decay rate of θ will then be limited

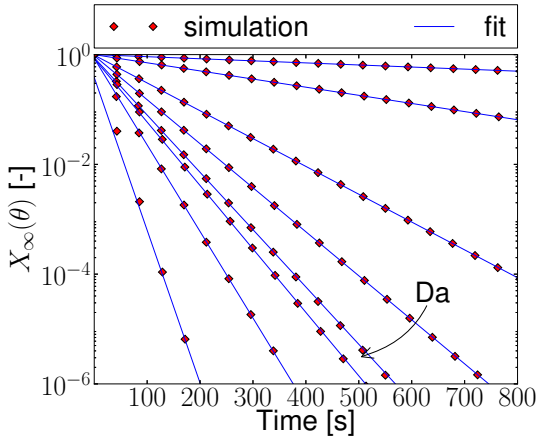

Figure 3: The evolution of the molar fraction of θ plotted over time for different Damköhler numbers. A higher Damköhler number results in a faster decay of passive scalar molar fraction over time.

by the diffusion of θ to the surface of the particle clusters, and the decay rate can be calculated using

$$\alpha_c = n_c \tilde{\lambda}_c \overline{A}_c, \tag{26}$$

with n_c being the number density of particle clusters in the domain. This n_c is depending on flow parameters such that

$$n_c = \left(\frac{L_x}{A_1 l} \right)^d \tag{27}$$

where the length scale of the clusters responsible for particle clustering is given by

$$l = \left(\tau_p \mathrm{u}_{rms}\right)^{3/2} \sqrt{k_f}. \tag{28}$$

Here L_x is the main length of the domain and d the dimensionality of the problem (here: 3). The size of particle clusters is an area of ongoing research [14]. How l is obtained in this study can be found in appendix A, it is the scale of the eddies with the same time scale as the particles. A_1 is a fitting parameter to account for the non-sphericity of the superparticles, for space-filling spherical superparticles it would be 1. In the cases present in this study, A_1 is $\approx 9 \ldots 11$. This corresponds to highly elongated and twisted particle clusters. Since a single particle is smaller than a grid cell, and the size of the particle clusters is of the order of the domain, the consumption rate of θ is controlled by diffusive processes, i.e.

$$\tilde{\lambda}_c = \frac{k_c}{C_g} = \frac{D_t \mathrm{Sh}}{2l}, \tag{29}$$

with D_t being the turbulent diffusivity. D_t is the sum of molecular diffusivity and convective transport of θ by eddies smaller than the eddies responsible for clustering. In our cases D_t is approximated by

$$D_t = D + \frac{u_l l}{3} \tag{30}$$

with u_l being the velocity of the eddies on the clustering length scale

$$u_l = \frac{l}{\tau_l} = u_{\mathrm{rms}}^{3/2} \sqrt{k_f \tau_p}. \tag{31}$$

For the present cases the molecular diffusivity has a larger impact than the turbulent one, as can be seen when comparing figures 7 and 8. The mean particle cluster surface area can be approximated by $\overline{A}_c = 4\pi l^2$ so that the decay rate for large Damköhler numbers becomes

$$\alpha_c = n_c 2\pi l D_t \mathrm{Sh}, \tag{32}$$

which scales no longer with the number of particles and is controlled by flow field parameters.

4 Results

The high Damköhler numbers can only be achieved through a high mass loading $M_{particles,tot}/M_{fluid,tot}$ of up to 1.6. Gore [15] and Kenning [16] describe how high mass loading through small particles reduces the intensity of turbulence. This effect can be seen in figures 4 and 6. Particles decrease the velocity fluctuations so that the mean u_{rms} is lower. Figure 6 shows the turbulent energy spectrum for increasing mass loading. For high mass loading, the overall turbulent energy is lower for the forcing wavenumbers and the slope of the energy cascade is slightly straitened out. Figure 5 shows the fraction of cells that contain a number of particles over the total number of cells for a simulation with 256^3 cells and 1.25 million particles with the default diameter of 50μm. There are a number of cells were the assumption of non interacting point particles no longer holds, but this number is very small compared to the total number of cells and doesn't affect the flow simulation negatively, as can be seen in the turbulent energy spectrum in figure 6.

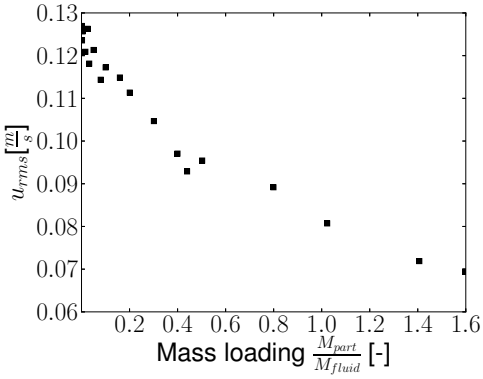

Figure 4: Mass loading decreases turbulent intensity. Turbulent velocity plotted over the mass loading parameter.

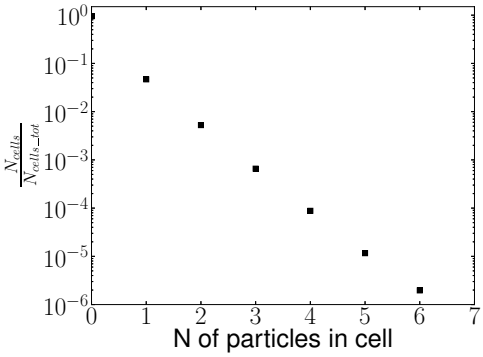

Figure 5: The fraction of cells with a high number of particles is insignificant. Fraction of cells plotted over number of particles in each cell for 1.25 million particle run

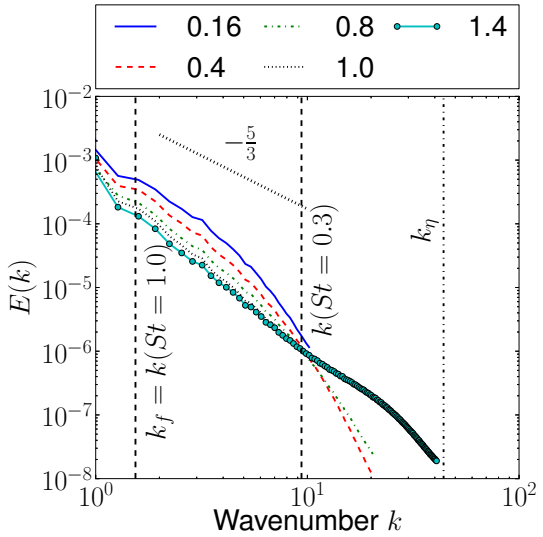

Figure 6: urbulent energy spectra plotted for increasing mass loading $\frac{M_{particles}}{M_{fluid}}$. Increasing the mass loading decreases the turbulent energy.

The fitted decay rate over the Damköhler number for different particle Stokes numbers and molecular

diffusivities can be seen in figures 7 and 8. Two distinct regimes with a transition in between can be observed: The linear scaling of the decay rate for small Damköhler numbers, and the decay rate controlled by the particle clusters as an asymptote for high Damköhler numbers. The error bars show how the decay rate deviates from the mean fitted decay rate during each simulation. A high variance is observed when the particle number density and the resulting decay rate is high. For both diffusivities, the maximum decay rate (dashed red) is lower for the higher Stokes number. Increasing the molecular diffusivity of the passive scalar increases the overall decay rate, where a tripling of the diffusivity roughly doubles the achieved decay rate.

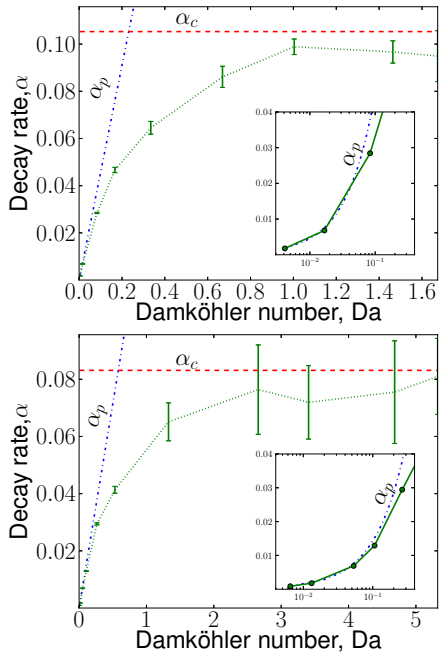

Figure 7: Decay rate plotted over Damköhler number for St=0.3 (upper panel) and St=1.0 (lower panel). For high Damköhler numbers, the decay rate approaches a set value. The diffusivity is $D = 10^{-3}\text{m}^2/\text{s}$.

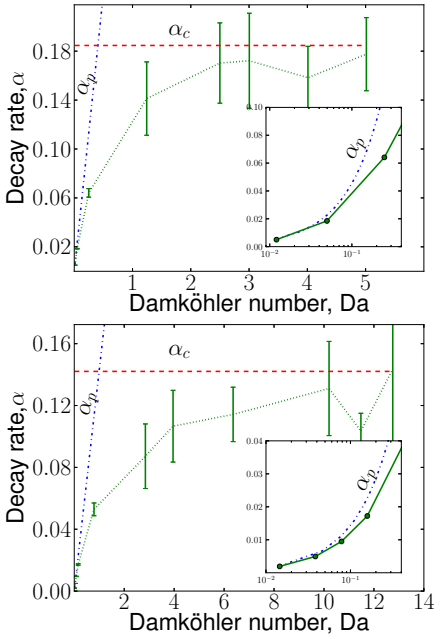

Figure 8: Decay rate plotted over Damköhler number for St=0.3 (upper panel) and St=1.0 (lower panel). For high Damköhler numbers, the decay rate approaches a set value. The diffusivity is $D = 3 \cdot 10^{-3}\text{m}^2/\text{s}$.

5 Conclusions and future work

Particle laden turbulent flow fields with different Damköhler numbers, particle Stokes numbers and molecular diffusivities have been simulated. A gas phase species, which is here referred to as a passive scalar, is consumed at the surface of the particles, causing its concentration to decay with time. In flows

with a high Damköhler number, the particle number density inside the clusters produced by the flow turbulence is so high that all gaseous reactants inside the particle clusters are rapidly consumed, but the transport of reactants from the flow into the particle clusters is slow, severely slowing down the reaction rate. The actual reaction rate is much smaller than the reaction rate predicted by the assumption of homogeneous distribution. Furthermore, the deviation from the reaction rate assuming homogeneous particle distribution sets in at quite moderate Damköhler numbers ($\sim 10^{-1}$). Hence, if clustering is not accounted for when modeling e.g. char surface reactions, the reaction rates will be grossly overestimated for intermediate and large Damköhler numbers. This effect seems to be larger for particles that have a time scale similar to the integral scale. A possible explanation is that particles with this time scale are trapped most effectively in the eddies of the integral scales, creating very stable particle clusters, effectively separating pockets of particles from pockets of high passive scalar concentration. For all diffusivities and Stokes numbers studied, it has been found that the decay rate of the scalar scales with the Damköhler number for small Damköhler numbers, while the decay rate is independent of the Damköhler number for large Damköhler numbers.

Wether particles are concentrated in a cluster or evenly distributed has an impact on the resulting reaction rates. For simulations with models that do not account for local clustering, the lifetime of a char particle could be severely underpredicted. This can lead to huge difference in the simulated char burnout time compared to the burnout time in the real application. Industrial CFD tools that employ RANS or LES models, such as e.g. Ansys Fluent [17], can be affected by this. The next goal is now to develop a robust model for RANS and LES simulation tools that accounts for the effect of turbulence on the heterogeneous reactions. Working towards this model, the effect of a variable Sherwood number based on the reaction rate has to be studied and the range of analysed particle Stokes numbers expanded. Additionally, further studies looking at different flow Reynolds numbers are needed. Furthermore the studies will be extended to analyse the effect of clustering on more complex reaction mechanisms, where each reaction rate (and therefore chemical time scale) depends on the local temperature and activation energy.

Acknowledgements

The research leading to these results has received funding from the Polish-Norwegian Research Programme operated by the National Centre for Research and Development under the Norwegian Financial Mechanism 2009-2014 in the frame of Project Contract No Pol-Nor/232738/101/2014 (NELH). NELH also acknowledges the Research Council of Norway under the FRINATEK grant 231444.

A On the scale of the clustering eddies

From Kolmogorovs theory [11] we know that the eddy dissipation rate is given by

$$\epsilon = \frac{u_l^2}{\tau_l} = \frac{l^2}{\tau_l^3} = \text{constant} \tag{33}$$

with u_l being the velocity of an eddy with scale l and turnover time $\tau_l = l/u_l$. Setting up (33) for the eddy scale i and integral scale l and solving for the eddy scale, we get:

$$\tau_l = \tau_i \left(\frac{l}{L_i}\right)^{2/3} = \frac{l^{2/3}}{k_f^{1/3} u_{\mathrm{rms}}}, \tag{34}$$

because from our approach in section 3 we have

$$\tau_i = \frac{1}{k_f u_{\mathrm{rms}}}. \tag{35}$$

Combining (34) and (35) and solving for l yields

$$l = (u_{\mathrm{rms}} \tau_l)^{3/2} \sqrt{k_f}, \tag{36}$$

when $k_f = 1/L_i$ and $\tau_l = \tau_p$.

REFERENCES

[1] International Energy Agency. World energy outlook 2013 November 2013.

[2] Silaen, A. and Wang, T. Effect of turbulence and devolatilization models on coal gasification simulation in an entrained-flow gasifier. *Int. J. Heat Mass Transf.* APR 2010 **53**:2074–2091.

[3] Abani, N. and Ghoniem, A. F. Large eddy simulations of coal gasification in an entrained flow gasifier. *Fuel* FEB 2013 **104**:664–680.

[4] Ansys Inc. Ansys 15.0 capabilities Aug 2014. Available at `http://www.ansys.com/`.

[5] Ferziger, J. H. *Computational Methods for Fluid Dynamics*. Springer Berlin Heidelberg 2002.

[6] Luo, K., Wang, H., Fan, J. and Yi, F. Direct Numerical Simulation of Pulverized Coal Combustion in a Hot Vitiated Co-flow. *Energy & Fuels* OCT 2012 **26**:6128–6136.

[7] Veynante, D. and Vervisch, L. Turbulent combustion modeling. *Prog. Energy Combust. Sci*. 2002 **28**:193 – 266.

[8] Lipatnikov, A. *Fundamentals of Premixed Turbulent Combustion*. CRC Press 2013.

[9] Tsuji, C. T. C. J. D. S. M. S. Y. *Multiphase Flows Droplets*. CRC Press 2012.

[10] Warnatz, J., Maas, U. and Dibble, R. *Combustion: Physical and Chemical Fundamentals, Modelling and Simulation, Experiments, Pollutant Formation.* Springer 2001.

[11] Pope, S. B. *Turbulent Flows*. Cambridge University Press 2000.

[12] Brandenburg, A. Pencil code homepage July 2014. Available at `http://pencil-code.nordita.org/`.

[13] Brandenburg, A. *The pencil code manual - Numerical Methods*. NORDITA July 2015. Available at `http://pencil-code.nordita.org/doc.php`.

[14] Calzavarini, E., Kerscher, M., Lohse, D. and Toschi, F. Dimensionality and morphology of particle and bubble clusters in turbulent flow. *J. Fluid Mech*. Oct. 2007 **607,**:pp.13–24,.

[15] Gore, R. and Crowe, C. Effect of particle size on modulating turbulent intensity. *Int. J. Multiph. Flow* 1989 **15**:279 – 285.

[16] Kenning, V. and Crowe, C. On the effect of particles on carrier phase turbulence in gas-particle flows. *Int. J. Multiph. Flow* 1997 **23**:403 – 408.

[17] Ansys Inc. Ansys 15.0 theory guide Aug 2014. Available at `http://www.ansys.com/`.

[18] Baum, M. M. and Street, P. J. Predicting the combustion behaviour of coal particles. *Combust. Sci. Technol*. 1971 **3**:231–243.

5.2 Paper 2

The effect of turbulent clustering on particle reactivity

Jonas Krüger, Nils E. L. Haugen, Dhrubaditya Mitra and Terese Løvås
Published in the Proceedings of the Combustion Institute 2017;36:2333-2340

Available online at www.sciencedirect.com

ScienceDirect

Proceedings of the Combustion Institute 36 (2017) 2333–2340

Proceedings of the Combustion Institute

www.elsevier.com/locate/proci

The effect of turbulent clustering on particle reactivity

Jonas Krüger [a,*], Nils E.L. Haugen [a,b], Dhrubaditya Mitra [c], Terese Løvås [a]

[a] *EPT, NTNU, Kolbjørn Hejes vei 1B, Trondheim N-7491, Norway*
[b] *SINTEF Energy Research, Kolbjørn Hejes vei 1A, Trondheim N-7465, Norway*
[c] *NORDITA, KTH Royal Institute of Technology and Stockholm University, Roslagstullsbacken 23, Stockholm SE-10691, Sweden*

Received 3 December 2015; accepted 29 June 2016
Available online 11 July 2016

Abstract

The effect of turbulence on the heterogeneous (solid–fluid) reactions of solid particles is studied numerically with Direct Numerical Simulations (DNS). A simplified reaction system is used, where the solid–fluid reaction is represented by a single isothermal reaction step. It is found that, due to the clustering of particles by the isotropic turbulence, the overall reaction rate is entirely controlled by the turbulence for large Damköhler numbers. The particle clustering significantly slows down the reaction rate for increasing Damköhler numbers which reaches an asymptotic limit that can be analytically derived. This implies that the effect of turbulence on heterogeneously reacting particles should be included in models that are used in CFD simulations of e.g. char burnout in combustors or gasifiers. Such a model, based on the chemical and turbulent time scales, is here proposed for the heterogeneous reaction rate in the presence of turbulence.

Keywords: Turbulent reacting multiphase flow; Char oxidation; Clustering

1. Introduction

Particles that are exchanging mass with a surrounding turbulent flow are found in a wide range of situations, both in nature and industrial applications. Examples of these are pulverized coal combustion in large power plants and fluidized beds in the process industry. A general feature among all these systems is their multi-scale nature, where the smallest scale is typically the size of the particle, or even the internal structure of the particle, while the largest scale is the much larger size of the entire combustion chamber or reactor. In the intermediate range between these two extremes, one finds the scales of the turbulence, which go from the Kolmogorov scale to the energy containing scale (the integral scale). Another common feature is that the particles exchange mass with the surrounding fluid through chemical reactions on the surface of the particles, as e.g. during the oxidation or gasification of char.

The effect of turbulence on different large scale properties of the flow, such as turbulent viscosity, diffusivity and conductivity has been known for a long time. A relatively large number of models have been developed in order to account for these effects,

* Corresponding author.
E-mail address: jonas.kruger@ntnu.no (J. Krüger).

http://dx.doi.org/10.1016/j.proci.2016.06.187
1540-7489 © 2016 by The Combustion Institute. Published by Elsevier Inc.

such as e.g. the k-ε model [1] and different versions of the Reynolds Stress Model [2]. When homogeneous combustion is considered, relatively good models such as the Eddy Dissipation Model [3], different variants of Probability Density Function models [4] or models based on conditioned parameters such as Conditional Moment Closure models [5] are being used. Veynante and Vervisch [6] review the current state of homogeneous combustion modeling, where they link distinctive homogeneous combustion regimes to different Damköhler numbers, which is the ratio of turbulent and chemical timescales. A perfectly stirred reactor system is used for low Damköhler numbers while reactions take place in thin wrinkled reaction zones for high Damköhler numbers. In essence, the regimes differ in the degree of spatial separation of reactants; while in the homogeneous case all reactants are gaseous, the heterogeneous case contains solid particles embedded in a fluid. However, spatial separation and its effect persists, as inertial particles cluster in turbulence, leading to regions of high or low particle concentration. Experimental and numerical studies of this phenomenon are reviewed in the work of Eaton and Fessler [7]. A detailed numerical investigation can be found in the work of Squires and Eaton [8] and for photos and statistics of preferential concentration of particles in isotropic turbulence in an experiment, the reader is referred to the work of Wood et al. [9]. Annamalai and Ramalingam [10] investigated the combustion modes for particles in a frozen gas phase dependent on their concentration and found that for densely clustered particles, the combustion behavior deviates from individual particle combustion. The present study aims to extend this analysis to heterogeneous combustion regimes in turbulent flows with particles that are clustered by the flow.

A range of efforts to simulate heterogeneous conversion systems under turbulent conditions have been made. Among recent work one can mention that of Silaen and Wang [11] who simulated an existing gasifier with Reynolds-averaged Navier Stokes (RANS) using different turbulence models for the continuum phase and compared their results with measurements. The turbulence effect on particles was included using a stochastic tracking scheme for the particles position, hence turbulence was not taken into account for the heterogeneous reaction rate or transport of gas phase species to the particles. Vascellari et al. [12] ran 2D RANS simulations with kinetics calibrated to experiments and a detailed description of the heterogeneous reactions inside the particle via an effectiveness factor and solving directly for the species partial pressure at the particles surface by assuming local equilibrium. They compare their simulations with measurements from an industrial-scale gasifier and achieve good agreement. Yet, to the knowledge of the authors, only very few studies of combustion or gasification, where account is made for the effect of turbulence on the heterogeneous char conversion, are published, among these are the papers of Luo et al. [13], Brosh and Chakraborty [14] and Brosh et al. [15]. Here, the Direct Numerical Simulations (DNS) approach is utilized, where all turbulence scales are explicitly resolved on the computational grid, and hence the effect of the turbulence is implicitly accounted for.

Despite all the effort that has been put into the development of models for turbulent homogeneous combustion or gasification, no good model has been proposed for turbulent heterogeneous combustion or gasification. This means that when particles that react with the surrounding fluid, such as during char oxidation (i.e. gas phase species react with the solid part of the particle, not the volatile part) are embedded in a turbulent flow, the turbulence is typically never taken into account in the simulations. The goal of this paper is to highlight the effect of turbulence on solid particles using DNS, and to develop a simple model for the influence of turbulence on reactive particles.

2. Implementation

The direct numerical simulations are performed with the Pencil Code [16], a finite difference code for compressible reactive flows that is fully parallelizable and shows good weak scaling behavior. It uses a sixth-order finite difference scheme for spatial discretization and a memory-efficient third-order Runge–Kutta scheme [17] for temporal discretization. The particles are treated in a Lagrangian manner and a cloud-in-cell method [16] is used both to interpolate the fluid phase variables at the particles position and for the back reaction from the particles to the fluid. To achieve a system that is independent of direction, all boundaries are periodic and gravity forces are neglected for particles and fluid alike.

2.1. Fluid phase equations

In order to isolate the effect of turbulence on reactivity alone, we consider a simplified case with only one reactive species, which is treated as a scalar field advected and diffused by the carrier fluid. This reactant is passive for the fluid flow and is assumed to react only with the solid phase in a catalytic manner. As a result, the reactant is converted on the surface of the particle, but no mass and energy is exchanged with the particle. For simplicity, the reaction is further assumed to be neither endothermic nor exothermic. It proceeds at a constant rate λ, which only depends on the surface area of the solid phase. The equation describing the

conservation of mass for the isothermal flow is

$$\frac{\mathrm{D}\rho}{\mathrm{D}t} = -\rho\nabla\cdot\boldsymbol{u}, \tag{1}$$

with ρ and $\boldsymbol{u}$ being the fluid density and velocity, respectively, and the advective derivative is given by

$$\frac{\mathrm{D}}{\mathrm{D}t} = \frac{\partial}{\partial t} + \boldsymbol{u}\cdot\nabla. \tag{2}$$

The equation for the conservation of momentum is

$$\rho\frac{\mathrm{D}\boldsymbol{u}}{\mathrm{D}t} = \nabla\cdot(2\mu\boldsymbol{S}) + \rho\boldsymbol{f} + \boldsymbol{F}, \tag{3}$$

where viscous effects are accounted for by the traceless rate of strain tensor $\boldsymbol{S}$ and the dynamic viscosity μ. To obtain statistically stationary isotropic turbulence, we employ a forcing function $\boldsymbol{f}$ equivalent to that of Babkovskaia et al. [18]. The force is acting on the wavevectors lying on a shell in Fourier space with a radius of k_f, accelerating the flow at low wavenumbers. The flow integral scale is given by $L_f = L_x k_1/k_f$ when L_x is the size of the simulation box and $k_1 = 1\ \mathrm{m}^{-1}$ is the wave number of the box size. Since some cases simulated here have significant mass loading, influencing the turbulence field [19,20] and the focus of the current work is not on turbulence statistics that are distorted by two-way coupling [21], the term $\boldsymbol{F}$ represents the drag force the particle exerts on the fluid phase.

The conservation equation for the molar fraction X of the reactant reads:

$$\frac{\partial X}{\partial t} + \nabla\cdot(X\boldsymbol{u}) = -D\nabla^2 X + \frac{\hat{R}}{\rho}, \tag{4}$$

with D being the diffusivity of the reactant and $\hat{R}$ the source term due to the conversion of the reactant at the particles surface. Thus the reactant can be thought of as oxygen reacting with the carbon of a long lasting char particle without any thermal or flow effects.

2.2. Particle equations

The particles are modeled using a Lagrangian approach. They are spherical and treated as point particles as the typical particle size of $\approx 30\ \mu$m is significantly smaller than the grid size. As the density of the particle is magnitudes higher than the fluid phase, we assume that the only force acting on the particle is the Stokes drag. The velocity $\boldsymbol{v}$ of the particle is evolved as

$$\frac{d\boldsymbol{v}}{dt} = \frac{1}{\tau_p}(\boldsymbol{u}-\boldsymbol{v}) = \frac{\boldsymbol{F}}{m_p}, \tag{5}$$

with the particle stopping time given as $\tau_p = Bd_p^2/18\nu(1+f_c)$ when $f_c = 0.15\mathrm{Re}^{0.687}$ is due to the Schiller–Naumann correlation [22]. Here B stands for the density ratio between particle and fluid, d_p is the particles diameter and m_p the particles mass.

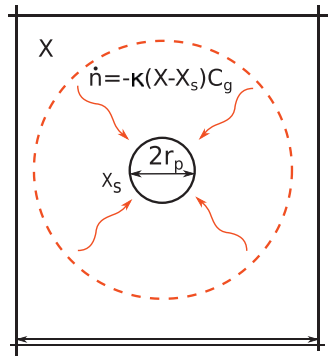

Fig. 1. Visualization of the flux to the particles surface.

The reactant that is carried by the fluid phase is converted at the particle surface at a rate of $\hat{R} = A_p\dot{n}\bar{M}/V_{cell}$, where A_p is the particles surface area, $\dot{n}$ is the reactant conversion rate per surface area, $\bar{M}$ the molar mass of the carrier fluid and V_{cell} the volume of one grid cell. By letting the reactant molar fraction be denoted by X_s at the particles surface and X at a large distance from the surface, one can express the reactant conversion at the surface by $\dot{n} = -\lambda X_s C_g$, where λ is the surface specific molar conversion rate. This is illustrated in Fig. 1. Assuming that the conversion at the surface is in equilibrium with the diffusive flux from the fluid phase to the particles surface $\dot{n} = -\kappa(X - X_s)C_g$, and solving for the surface mole fraction X_s of the reactant, a modified reaction rate $\tilde{\lambda}$ for the reactant conversion is defined as

$$\dot{n} = -\tilde{\lambda}XC_g \tag{6}$$

when

$$\tilde{\lambda} = \lambda/(1+\lambda/\kappa) \tag{7}$$

is obtained following the ideas of Baum and Street [23]. The adapted reaction rate $\tilde{\lambda}$ for the conversion rate will be important when formulating a model for the effect of turbulent clustering on the reactivity. The mass transfer coefficient is here given by

$$\kappa = D\mathrm{Sh}/2r_p \tag{8}$$

where the Sherwood coefficient Sh is set to two for all particle sizes representing quiescent flow around the particles for simplicity as the focus in this work is on macroscopic effects.

2.3. The limits of the decay rate

In order to study the effect of turbulent clustering on the reactant conversion it is useful to identify the governing chemical and turbulent time and length scales.

The integral flow time scale $\tau_L = L_f/\boldsymbol{u}_{\mathrm{RMS}}$ is based on the root mean square of the velocity u_{RMS} and the scale of the forcing L_f. It is often claimed

that the highest value of the preferential concentration for particles is found for particles with a Stokes number around unity based on the Kolmogorov scale η [7,9]. Since for the current study it is the large scale clusters that are interesting, the Stokes number is here, however, defined based on the integral time scale τ_L such that $\mathrm{St} = \tau_p/\tau_L$. Assuming homogeneously distributed particles, the instantaneous value of the reactant molar fraction X is given by:

$$X(t) = X_0 e^{-n_p \tilde{\lambda} A_p t} = X_0 e^{-\alpha_{th} t}. \tag{9}$$

If the initial molar fraction of the reactant X_0 is set to unity, and the particle number density n_p is given, the maximum theoretical decay rate $\alpha_{th} = n_p \tilde{\lambda} A_p$ can thus be estimated. Its inverse $1/\alpha_{th} = \tau_{th}$ is the theoretical reactive time scale.

By defining a Damköhler number $\mathrm{Da} = \tau_L/\tau_{th}$, the evolution of the decay rate α with Damköhler number can be studied. For low particle number densities, and therefore small Damköhler numbers, the macroscopic clustering of particles can be neglected, and $\mathrm{Da} = \tau_L/\tau_{th} = \tau_L \alpha_{th}$ can be formed to yield the *particle* dependent decay rate $\alpha_{th} = \alpha_p = \mathrm{Da}/\tau_L$, which implies that the decay rate increases linearly with the Damköhler number. For higher particle number densities, the macroscopic clusters have high internal particle number densities, which are rapidly converting the reactant within the cluster. This is due to the fact that the chemical timescale inside the cluster is much shorter than the timescale of the cluster itself. Now the decay rate is controlled by the transport of reactant to the surface of these macroscopic clusters, and it is reasonable to consider the particle clusters as single bodies, or super-particles, that the reactants are converted at. One can then formulate a *cluster* dependent decay rate as $\alpha_c = n_c \tilde{\lambda}_c \bar{A}_c$, which is based on the cluster number density n_c the modified conversion rate $\tilde{\lambda}_c$ and cluster surface area $\bar{A}_c$, which are constants dependent on the macroscopic flow field. The typical cluster size is obtained by assuming constant dissipation rate ε for the integral scale and the scale of the clustering eddies l and applying Kolmogorovs theory:

$$\varepsilon = \frac{l^2}{\tau_l^3} = \frac{L_f^2}{\tau_L^3} \tag{10}$$

when u_l is the velocity of an clustering eddy with scale l and turnover time $\tau_l = l/u_l$. The coupling between the integral scale L_f and the eddy scale l is now given as

$$\tau_l = \tau_L \left(\frac{l}{L_f} \right)^{2/3} = \frac{l^{2/3}}{k_f^{1/3} u_{\mathrm{RMS}}}, \tag{11}$$

since $\tau_L = L_f/u_{\mathrm{RMS}} = 1/k_f u_{\mathrm{RMS}}$. Solving Eq. (11) for l and assuming that the eddy timescale is similar to the timescale of the particles that it captures ($\tau_l = \tau_p$) yields

$$l = (u_{\mathrm{RMS}} \tau_p)^{3/2} \sqrt{k_f}. \tag{12}$$

The particle cluster number density $n_c = (A_1 l)^{-3}$ and surface area $\bar{A}_c = A_2 l^2$ can now be computed using A_1 and A_2, where $\mathrm{A_1}$ is of order one for all simulations, while A_2 relates to the shape of the clusters and is currently set to 4π, assuming spherical clusters. Predicting A_1 and A_2 is the topic of ongoing work. The modified conversion rate $\tilde{\lambda}_c$ is obtained by using the cluster size l in the mass transfer coefficient calculation Eq. (8) and inserting the resulting κ into Eq. (7).

One can now estimate values for n_c, $\tilde{\lambda}_c$ and $\bar{A}_c$, to find α_c. The following proposed formulation of $\alpha(\mathrm{Da})$ then satisfies the limits as derived at high and low values of the Damköhler number:

$$\alpha(\mathrm{Da}) = \frac{\alpha_c \mathrm{Da}}{\alpha_c \tau_L + \mathrm{Da}}. \tag{13}$$

This formulation will be compared directly to results from direct numerical simulations in the following section.

2.4. Damköhler numbers in real combustion systems

The Damköhler and Stokes numbers investigated in this study can also be found in real combustion systems. An example, the Damköhler number of the International Flame Research Foundation (IFRF) furnace #1 as used in the work of Olenik et al. [24] is approximated in the following. A coal particle with a mean diameter d_p of 45 μm and a density ρ_p of 800 kg/m^3 in a flow with a density of 0.35 kg/m^3 and a viscosity of $1.17 \cdot 10^{-4}$ m^2/s has a stopping time of $\tau_p = 22 \cdot 10^{-4}$ s. The integral time scale of a system with a quarl size of ≈ 0.23 m and a u_{RMS} of 7 m/s is $\tau_L = 32 \cdot 10^{-3}$ s. This leads to an integral scale based Stokes number of $\mathrm{St} = 0.066$. The coal and air feed rate together with the particles diameter yield a mean particle number density n_p of $1.445 \cdot 10^9$ particles/m^3. The chemical time scale, assuming diffusion limited reactions, is $\tau_{ch} = 1/(n_p \tilde{\lambda} A_p) = 21 \cdot 10^{-3}$ s, leading to a Damköhler number $\mathrm{Da} = \tau_L/\tau_{ch} \approx 1.57$, which is within the range of the current study. Due to the large range in turbulent scales and particle diameters typically found in real combustion systems, a wider range of Damköhler and Stokes numbers is also common.

3. Results and discussion

The computational domain for the DNS is a cube with an edge length of 2π cm, discretized with 64, 128 or 256 cells which results in grid cell sizes of 981, 490 and 245 μm, respectively with increasing particle numbers. The strength of the forcing is chosen such that a u_{RMS} of 0.1 m/s and a

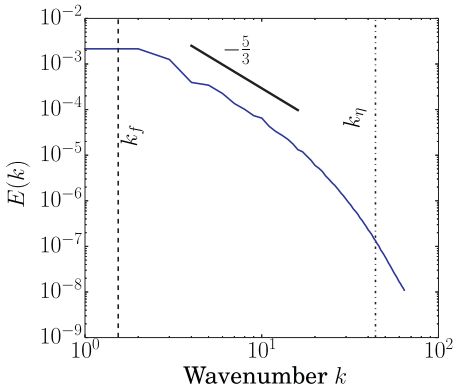

Fig. 2. Power spectrum over the wavenumber for a case with a $\mathrm{Re} \approx 250$ and a resolution of 128 cells. Shown are the forcing wavenumber k_f, the wave number of the Kolmogorov scale k_η and the Kolmogorov scaling.

turbulent Reynolds number $\mathrm{Re} = u_{\mathrm{RMS}} L_f / \nu$ of approximately 250 is obtained for all cases. Furthermore, the size and density of the particles are chosen to give particle Stokes numbers of $\mathrm{St} = 0.1$ and $\mathrm{St} = 1.0$. The particles are initialized at random positions with zero velocity at startup.

Figure 2 shows the energy spectrum for a case with a Reynolds number of 250. The energy inserted into the domain at the forcing wavenumber k_f (1.5 times the lowest wavenumber of the domain) is indeed transported to the higher wavenumbers via the inertial subrange, which can be identified by its $-5/3$ slope, before it is dissipated around the Kolmogorov wavenumber k_η.

The simulations are run until the turbulence is statistical stationary, which is determined by a stabilization of the mean u_{RMS}. The molar fraction of the reactant is then re-initialized to unity. The decay rate is obtained by fitting an exponential function to the reactant molar fraction from the start of data sampling to later times.

The resulting decay rates as function of Damköhler numbers are shown in Fig. 3 for the particle Stokes numbers $\mathrm{St} = 0.1$ and $\mathrm{St} = 1.0$. The deviation of decay rates around the mean are shown by the error bars. The Damköhler number is increased by increasing the number of particles. Furthermore, the proposed modeled decay rate of the reactant molar fraction over the Damköhler number according to Eq. (13) is shown as the solid curve, with the two limiting decay rates α_p and α_c for small and large Damköhler numbers respectively included as dashed-dotted and dashed lines. In Fig. 3 it can be seen that for cases with low Damköhler numbers, the decay rate as predicted by DNS is indeed proportional to the Damköhler number and follows α_p, but significant deviations from the linear increase are observed quite early.

The decay rate begins to deviate from the linear increase (as given by α_p) for Damköhler numbers as small as 0.1 for the given cases. For higher Damköhler numbers the decay rate approaches the flow field dependent decay rate α_c asymptotically. The modeled decay rate $\alpha(\mathrm{Da})$ as defined by Eq. (13) fits the decay given by DNS rather well. Moreover, it is observed that the value of α_c is lower for a higher particle Stokes number. The variance in the decay rates is higher for higher Stokes numbers, and this effect increases in strength for higher Damköhler numbers.

Figure 4 shows a snapshot of the position of every 300th particle (dots) and the upper 90% percentile of the reactant concentration (shaded areas) for particle Stokes numbers $\mathrm{St} = 0.1$ and $\mathrm{St} = 1.0$. For a Stokes number of 0.1 the particles tendency to cluster is not visible and the pockets of high reactant concentration are small. Larger areas devoid of particles can be seen at the higher Stokes

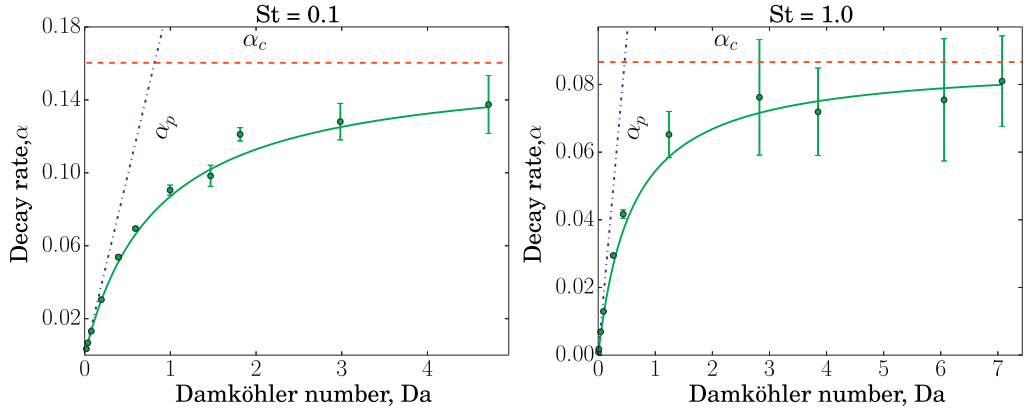

Fig. 3. Decay rate over Damköhler number. The left plot is for $\mathrm{St}_i \approx 0.1$, and the right for $\mathrm{St}_i \approx 1$. Filled circles represent the decay rates of the numerical simulations, while the solid lines are fits to the numerical results as given by Eq. (13). The dashed-dotted lines correspond to α_p while the dashed lines represent α_c.

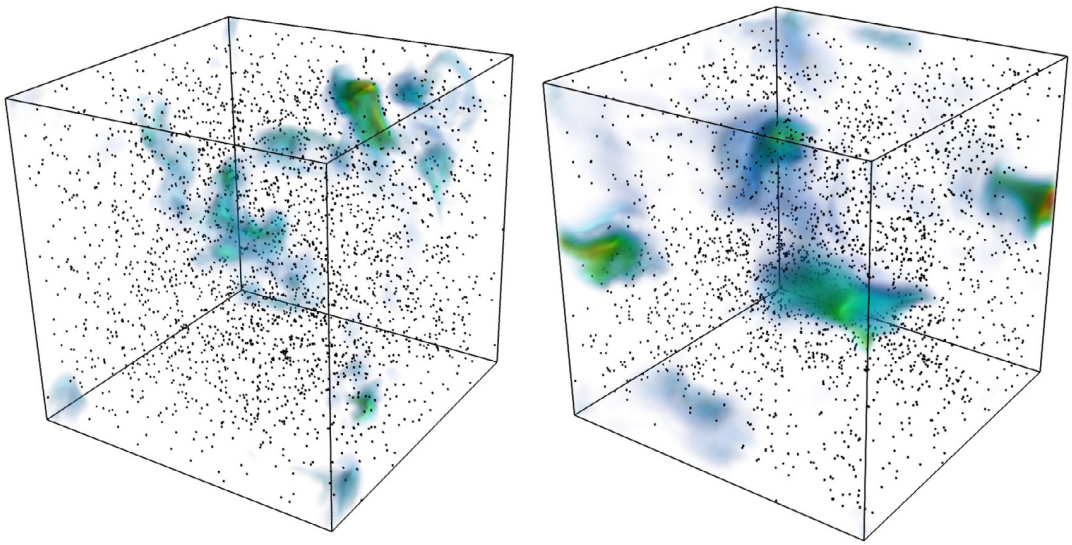

Fig. 4. 3D plot of the domain with every 300th particle and the 90th percentile of the reactant concentration: $St = 0.1$ (left) and $St = 1.0$ (right).

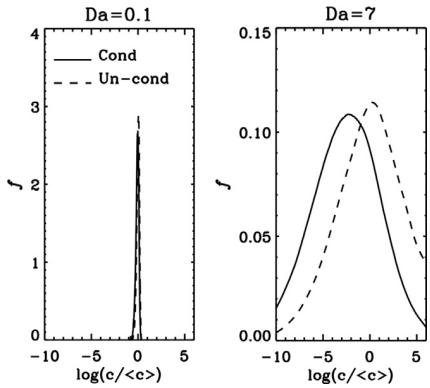

Fig. 5. Probability density function of the logarithm of the reactant concentration c.

number, as well as larger volumes of remaining reactant. Overall, the particles in the St = 1.0 runs show stronger large scale clustering than for the St = 0.1 runs.

The probability density, f, for a given reactant concentration c is shown for two different Damköhler numbers in Fig. 5. The dashed lines represent the probability averaged over the entire domain, while the solid lines represent the probability at the position of the particles. For a small Damköhler number of 0.1, it is seen that the distribution is very narrow, and that the probability constraint on the particle position is nearly identical to the probability of all the fluid elements. This means that the reactant concentration is fairly homogeneous, and that it is not affected by the instantaneous position of the particles, i.e. that particle clustering does not influence the reactant distribution in a significant way. For higher Damköhler numbers the distribution is broadening, which means that the reactant distribution is becoming less homogeneous as the importance of the particle clustering is increasing. One can conclude that for large Damköhler numbers the reactions inside the particle clusters are so fast compared to the lifetime of the cluster that the interior of the clusters is essentially always drained of reactants. The domain is essentially divided into two distinct zones, the particle clusters with high particle and low scalar concentration and the scalar pockets with opposite attributes. This means that the reactions are happening at the external surface of the clusters, which resembles how reactants are converted at the external surface of solid objects. This in turn supports the assumption underlying the derivation of the asymptotic limit of α_c.

The mass loading M_l in the simulations is defined as the ratio of the total mass of the particles $M_p = \sum_i m_{p,i}$ to the total mass of the fluid $M_f = V\overline{\rho}$ such that $M_l = M_p/M_f$. The influence of the mass loading on the turbulent velocities is shown in Fig. 6.

In the left panel the turbulent velocity u_{RMS} is shown as a function of mass loading. The mass loading does not seem to have any significant effect on the turbulent velocity for low mass loadings, but for larger values of mass load the turbulent velocity is significantly affected. This change in turbulent intensity will affect the cluster shape and in turn the surface area $\bar{A}_c$. For very high Damköhler numbers, this may reduce the reactivity of the

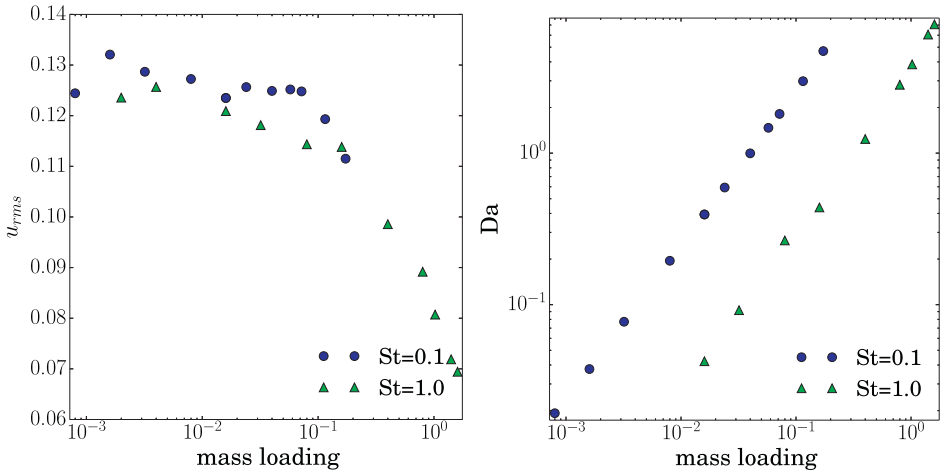

Fig. 6. Root mean square of velocity and Damköhler number as function of mass loading $M_l = M_p/M_f$ for two different Stokes numbers.

cluster even more than estimated by α_c. In the right panel of Fig. 6, the Damköhler number is plotted as a function of the mass loading for the two different Stokes numbers. It can be observed that the larger Stokes numbers require higher mass loadings in order to obtain the same Damköhler number.

4. Conclusions

The effect of particle clustering due to flow turbulence on the reaction rate of heterogeneous reactions is studied in a simplified setup. The particles are assumed to act like catalysts, and a simple one step reaction with the gas phase reactant on the particle surface is assumed to be fast and isothermal. With this simplified setup it is possible to analytically show that for small Damköhler numbers the overall reactivity is found not to be affected by turbulent clustering. However, for large Damköhler numbers, the reaction rates are fast compared to the lifetime of the particle clusters. Hence, the effect of the clusters on the overall reaction rate in the domain becomes important decreasing the overall reaction rate. This effect is stronger for higher Stokes numbers.

A simplified model that gives the reactant decay rate as a function of the turbulent and chemical time scales (see Eq. (13)) is proposed. The predictive quantitative abilities of the presented model depend on a good representation of the shape, size and number density of the particle clusters. These aspects of the cluster formation are generally not yet properly understood and further work to understand the shape and number density of particle clusters depending on flow field variables is needed [25]. Furthermore, equivalent investigations using more realistic heterogeneous reaction schemes and fluid phase physics will have to follow.

Acknowledgments

The research leading to these results has received funding from the Polish-Norwegian Research Programme operated by the National Centre for Research and Development under the Norwegian Financial Mechanism 2009–2014 in the frame of Project Contract No. Pol-Nor/232738/101/2014. This work was supported by the grant Bottlenecks for particle growth in turbulent aerosols from the Knut and Alice Wallenberg Foundation, Dnr. KAW 2014.0048 and by grant from Swedish Research Council (Dnr. 638-2013-9243). NELH and DM also acknowledge the Research Council of Norway under the FRINATEK grant 231444.

References

[1] W. Jones, B. Launder, *Int. J. Heat Mass Transf.* 15 (2) (1972) 301–314.
[2] S.B. Pope, *Turbulent Flows*, Cambridge University Press, 2000.
[3] B. Magnussen, B. Hjertager, *Proc. Combust. Inst.* 16 (1) (1979) 719729.
[4] C. Dopazo, *Turbulent Reacting Flows*, Academic Press, London, 1994.
[5] A.Y. Klimenko, R. Bilger, *Progr. Energy Combust. Sci.* 25 (1999) 595–687.
[6] D. Veynante, L. Vervisch, *Progr. Energy Combust. Sci.* 28 (3) (2002) 193–266.
[7] J.K. Eaton, J.R. Fessler, *Int. J. Multiph. Flow* 20 (1994) 169–209.
[8] K.D. Squires, J.K. Eaton, *J. Fluid Mech.* 226 (1991) 1–35.
[9] A.M. Wood, W. Hwang, J.K. Eaton, *Int. J. Multiph. Flow* 31 (2005) 1220–1230.

[10] K. Annamalai, S. Ramalingam, *Combust. Flame* 70 (3) (1987) 307–332.
[11] A. Silaen, T. Wang, *Int. J. Heat Mass Transf.* 53 (9-10) (2010) 2074–2091.
[12] M. Vascellari, D.G. Roberts, S.S. Hla, D.J. Harris, C. Hasse, *Fuel* 152 (2015) 58–73.
[13] K. Luo, H. Wang, J. Fan, F. Yi, *Energy Fuels* 26 (10) (2012) 6128–6136.
[14] T. Brosh, N. Chakraborty, *Energy Fuels* 28 (2014) 6077–6088.
[15] T. Brosh, D. Patel, D. Wacks, N. Chakraborty, *Fuel* 145 (2015) 50–62.
[16] A. Brandenburg, The Pencil Code, Pencil Code Homepage, http://pencil-code.nordita.org/, 2013 (accessed 03.06.16).
[17] J. Williamson, *J. Comput. Phys.* 35 (1) (1980) 48–56.
[18] N. Babkovskaia, N. Haugen, A. Brandenburg, *J. Comput. Phys.* 230 (1) (2011).
[19] K.D. Squires, J.K. Eaton, *Phys. Fluids* 7 (1990) 1191–12–3.
[20] R. Gore, C. Crowe, *Int. J. Multiph. Flow* 15 (2) (1989) 279–285.
[21] A. Ferrante, S. Elgobashi, *Phys. Fluids* 15 (2003) 315–329.
[22] Schiller, Naumann, *Ver. Deutsch. Ing.* 77 (1933) 318.
[23] M.M. Baum, P.J. Street, *Combust. Sci. Technol.* 3 (5) (1971) 231–243.
[24] G. Olenik, O. Stein, A. Kronenburg, *Proc. Combust. Inst.* 35 (3) (2015) 2819–2828. http://dx.doi.org/10.1016/j.proci.2014.06.149.
[25] E. Calzavarini, M. Kerscher, D. Lohse, F. Toschi, *J. Fluid Mech.* 607 (2007) 13–24.

5.3 Paper 3

Numerical Study of Hydrogen Inhibition of Char Gasification Using Detailed Hetero- and Homogeneous Chemical Kinetics

Joanna Lazar, Nils Erland. L. Haugen, Jonas Krüger, and Andrzej Szlek
Published in Energy & Fuels 2016;30:4411-4418

energy&fuels

Article

pubs.acs.org/EF

Numerical Study of Hydrogen Inhibition of Char Gasification Using Detailed Hetero- and Homogeneous Chemical Kinetics

Joanna Lazar,[†,‡] Nils Erland L. Haugen,[*,‡,§] Jonas Kruger,[‡] and Andrzej Szlek[†]

[†]Silesian University of Technology, Konarskiego 22, 44-100 Gliwice, Poland

[‡]Norwegian University of Science and Technology, 7491 Trondheim, Norway

[§]SINTEF Energy Research, 7465 Trondheim, Norway

ABSTRACT: It has been known for a long time that hydrogen in the gas phase tends to inhibit gasification of char at low and intermediate temperatures. At higher temperatures, however, there are indications that hydrogen may speed up gasification. The mechanisms behind these effects are currently not understood. In this work, a newly developed detailed chemical kinetics model for char has been used to study the mechanisms behind the hydrogen inhibition and speed up of char gasification. For conditions assumed in this work, the hydrogen inhibition is found for $T < 2000$ K, while for $T > 2000$ K, hydrogen in the gas phase speeds up the char conversion. By studying the species reaction rates together with the individual rate of every heterogeneous reaction, the reasons for hydrogen influence on char gasification are attempted to be explained for a wide range of different temperatures in this paper. The focus is not on investigating a real gasifier but rather to understand the fundamental mechanism behind hydrogen inhibition of char.

INTRODUCTION

For many applications, it is not feasible or just not economical to use solid fuels directly. It is therefore often useful to convert the solid fuel to either a gaseous or liquid fuel before it is used. Solid fuels, such as, e.g., coal, biomass, or pet coke, can be converted to a synthesis gas (syngas) through reactions with oxygen, steam, or carbon dioxide in a gasifier. The syngas can then be used for, e.g., electricity production in an integrated gasification combined cycle (IGCC), production of liquid fuels for the transportation sector, or production of hydrogen for fuel cells or use in the chemical industry.

The newly developed detailed heterogeneous chemical kinetics model of Tilghman and Mitchell,[1] with 18 reversible reactions for char reactions with oxygen, steam, and carbon dioxide, has been used in the current work. Hecht et al.[2] have shown that, in oxygen-fired systems, it is important to include the effects of CO_2 gasification. The chemical mechanism is used to study the mechanism behind the hydrogen inhibition of char gasification at low and intermediate temperatures. The effect of a speed up of the gasification process at higher temperatures has also been studied. To check the impact of hydrogen on the char gasification, without changing the thermodynamics of the fluid, the heterogeneous reactions that have gaseous molecular hydrogen as a reactant are turned on and off; i.e., the impact of a given reaction where hydrogen is a reactant is investigated by comparing the results obtained when that specific reaction is turned off with the results obtained when all reactions are turned on. In this way, the impact of hydrogen on the gasification process can be studied in great detail. The respective reactions are turned off by setting their pre-exponential factors to zero.

For low temperatures or small char particles, the conversion rate is kinetically controlled and the pore surface of the entire particle volume is reacting. This, which is known as zone I conversion, yields a constant particle radius, where the particle mass is reduced by a decrease in density. For very high temperatures or large particles, the reactants are consumed at the external surface of the particles. This decreases the particle radius while keeping the density constant and is known as zone III conversion. Zone II conversion, on the other hand, is observed for intermediate temperatures and particle sizes. For this regime, both particle radius and density are decreased and the relative fraction of decrease is described by Haugen et al.[3]

The effect of hydrogen inhibition on surface reactions was also recently studied by Pineda and Chen.[4] Here, the authors use a heterogeneous reaction mechanism consisting of eight reaction steps in a perfectly stirred reactor to find that the inhibition of hydrogen is due to the adsorbed molecular hydrogen filling up a significant fraction of all of the free sites on the carbon surface.

Hydrogen inhibition has previously been studied under many different gasifying conditions. One of the earlier discussions on the reaction mechanism behind hydrogen inhibition is found by Laurendeau.[5] In previous experimental work, inhibition has been observed at low (1 atm) and moderate (10 atm) steam pressures and moderate temperatures (950−1250 K)[6−10] as well as at high pressures (40−50 atm).[11,12] For gasification of a natural graphite at temperatures between 960 and 1120 °C and low pressures, Biederman et al.[8] found that hydrogen inhibition was caused by dissociative chemisorption of hydrogen on active carbon sites. For graphite−CO_2 reactions, they found that the inhibition was due to hydrogen chemisorbing on impurity catalyst sites. Barrio et al. studied the steam gasification of wood at atmospheric pressure and in the temperature range from 750

Special Issue: International Symposium on Combustion Processes

Received: March 2, 2016
Revised: April 6, 2016
Published: April 6, 2016

DOI: 10.1021/acs.energyfuels.6b00502
Energy Fuels 2016, 30, 4411−4418

Table 1. Intrinsic Heterogeneous Reaction Mechanism[a]

number	reaction	A_k	E_k	σ_k
R1	$2C_f + H_2O \leftrightarrow C(OH) + C(H)$	2.1×10^6	105	0
R2	$C(OH) + C_f \leftrightarrow C(O) + C(H)$	4.1×10^{11}	80	0
R3	$C(H) + C(H) \leftrightarrow H_2 + 2C_f$	1.4×10^{11}	67	0
R4	$C(O) + C_b \rightarrow CO + C_f$	1.0×10^{13}	353	28
R5	$C(OH) + C_b \leftrightarrow HCO + C_f$	1.0×10^{13}	393	28
R6	$C_b + C_f + C(H) + H_2O \leftrightarrow CH_3 + C(O) + C_f$	1.0×10^{13}	300	0
R7	$C_b + C_f + C(H) + H_2 \leftrightarrow CH_3 + 2C_f$	1.0×10^{13}	300	0
R8	$C_f + C(H) + CO \rightarrow HCO + 2C_f$	1.0×10^{13}	300	0
R9	$C(H) + C(H) \rightarrow CH_2 + C_f$	3.0×10^{11}	426	0
R10	$CO_2 + C_f \leftrightarrow C(O) + CO$	3.7×10^3	161	0
R11	$C_b + CO_2 + C(O) \rightarrow 2CO + C_f$	1.26×10^8	276	0
R12	$C(CO) \leftrightarrow CO + C_f$	1.0×10^{13}	455	53
R13	$CO + C(CO) \rightarrow CO_2 + 2C_f$	9.8×10^6	270	0
R14	$2C_f + O_2 \rightarrow C(O) + CO$	5.0×10^{10}	150	0
R15	$2C_f + O_2 \rightarrow C_2(O_2)$	4.0×10^7	93	0
R16	$C_f + C_b + C(O) + O_2 \rightarrow CO_2 + C(O) + C_f$	1.5×10^7	78	0
R17	$C_f + C_b + C(O) + O_2 \rightarrow CO + 2C(O)$	2.1×10^7	103	0
R18	$C_b + C_2(O_2) \rightarrow CO_2 + 2C_f$	1.0×10^{13}	304	33

[a]The units of both the activation energy E_k and the distribution width σ_k are kJ/mol, while the units of A_k are such that the units of $R_{reac,c}$ in eq 9 are mol m^{-2} s^{-1}.

to 950 °C.[10] In their work, it is concluded that the hydrogen inhibition effect can be described on the basis of Langmuir–Hinshelwood kinetics. The aim of the work of Tay et al.[13] was to investigate the role of hydrogen during the gasification of a Victorian brown coal at 800 °C in a fluidized-bed/fixed-bed reactor. Here, it was found that the inhibiting effects of hydrogen were not limited to its chemisorption on the char surface. The presence of hydrogen also changed the aromatic structure of char during gasification, which is most likely due to the ability of hydrogen radicals to penetrate into the char matrix. In the work of Fushimi et al.[14] on steam gasification of woody biomass char, it was observed that hydrogen inhibition was due to reverse oxygen exchange reactions in the first period and dissociative hydrogen adsorption on the char particle in the second period.

In the current work, the focus is on gasification of char from Wyodak coal, which is a sub-bituminous coal from Wyoming, U.S.A. It is expected, however, that the results should also be similar for other fuels, such as, e.g., other coal qualities or biomass.

MODEL DESCRIPTION

In this section, the essentials of the numerical model used to simulate the char gasification are described. The implementation of the numerical model has been verified by Haugen et al.[3] against the particle-resolved simulation tool (DNS) of the Stanford group. For more information on the model, the reader is referred to the study by Haugen et al.[15]

In the following, particles are assumed to be spherical and uniform in composition and morphology, while the ash is uniformly distributed throughout the particle volume. In addition, ash in the char cannot react or be evaporated, and there is no exchange of mineral matter between the particle and the gas phase.

The calculations are made on a single particle in the particle cloud. It is assumed that all other particles behave in the same way as the considered particle. The carbon in the particle will react with the hot reactive gases (O_2, H_2O, and CO_2), causing the mass, apparent density, and size of the particle to change with time. The heterogeneous chemical kinetics were developed by Tilghman and Mitchell[1] based on the work of Haynes[16] and are presented in Table 1, while the homogeneous chemical kinetic mechanism used is GRI-Mech 3.0.[17] The ultimate and proximate analyses of the coal are presented in Tables 2 and 3. In the heterogeneous reaction scheme,

Table 2. Proximate Analysis of Wyodak Coal

property	amount (wt %)
fixed carbon	35.06
volatile matter	33.06
moisture	26.30
ash	5.58

Table 3. Ultimate Analysis of Wyodak Coal

property	amount (wt %)
carbon	69.8
hydrogen	5.65
oxygen (by difference)	15.6
nitrogen	0.94
total sulfur	0.43
ash	7.57

the adsorbed species C(H), C(O), C(CO), and C(OH) represent a hydrogen atom, oxygen atom, carbon monoxide, and OH group adsorbed on a carbon site, respectively, while $C_2(O_2)$ represent two adjacent carbon sites that have adsorbed one oxygen atom each. The bulk carbon site, C_b, is a carbon atom bonded to four other carbon atoms. As a result of chemical reactions, the bulk carbon site can become a free carbon site. The free carbon site, C_f, is a carbon atom that is available for adsorption of gas-phase species. As a result of the particle–gas reactions, the oxygen, carbon, and hydrogen compounds desorb from the carbonaceous matrix and leave the particle surface. As a result of this process, an underlying carbon atom becomes a free carbon site.

Arrhenius parameters shown in Table 1 were obtained for Wyodak coal[1] based on thermogravimetric analysis (TGA). The obtained activation energies where found to be within expected ranges when compared to values for chars and activated carbon from the literature. In the experiments, the char conversion was limited only by the chemical reaction rates; i.e., the experiments were kinetically controlled. The pressure was held at 1 atm, and the testing temperatures were selected according to the reacting gases: 700–900 °C for environments containing H_2O, 800–1000 °C for

DOI: 10.1021/acs.energyfuels.6b00502
Energy Fuels 2016, 30, 4411–4418

environments containing CO_2, and 400−550 °C for environments containing O_2. The char specific surface area was measured with the Brunauer−Emmett−Teller (BET) method. Because the heterogeneous reaction mechanism is intrinsic, the surface area is required to calculate the total reaction rate of the char particle.

In this paper, the focus is on the two reactions that have molecular hydrogen as a reactant. This corresponds to reaction R3 backward (R3b) and reaction R7 forward (R7f). Hydrogen inhibition of char gasification is studied by investigating the effect of deactivating these two reactions.

The exchange of matter between the particles and the ambient gas is caused by reactions between the gas and the solid phase. The species production rate can be symbolized by $\omega_{pg,i}$ for the particle−gas reactions and $\omega_{gg,i}$ for the gas−gas reactions. These two terms determine the change of the mass fraction of species i in the gas phase.

Governing Gas-Phase Equations. In the following, a brief overview of the most important equations will be presented. For a full description of all relevant equations, the reader is referred to the study by Haugen et al.[15]

The gas phase is defined by three governing equations describing the evolution of mass, species, and temperature in the gas phase. The first equation describes the evolution of the mass of the gas phase m_g

$$\frac{dm_g}{dt} = \frac{m_g}{\rho_g}\sum_{i=1}^{N_{s,gas}} \omega_{pg,i} M_i \tag{1}$$

where ρ_g is the mass density of the gas phase, M_i is the molar mass of species i, and $\omega_{pg,i}$ is the molar production rate of species i as a reactions between the solid and the gas phase (heterogeneous reactions). The second equation describes the mass fraction Y_i of species i in the gas phase

$$\rho_g \frac{dY_i}{dt} + Y_i \sum_{k=1}^{N_{s,gas}} \omega_{pg,k} M_k = (\omega_{gg,i} + \omega_{pg,i}) M_i \tag{2}$$

where $\omega_{gg,i}$ is the molar production rate of species i as a result of gas-phase (homogeneous) reactions. The third equation is the energy equation, which is represented here by the temperature

$$\rho_g c_{p,g} \frac{dT_g}{dt} + \sum_{i=1}^{N_{s,gas}} h_i(\omega_{gg,i} + \omega_{pg,i}) M_i = n_p(Q_h + Q_c) \tag{3}$$

where $c_{p,g}$ is the heat capacity of the gas mixture at a constant pressure, T_g is the temperature of the gas, h_i is the enthalpy of species i, Q_h is the energy transfer from the solid phase to the gas phase as a result of heterogeneous reactions, and Q_c is the heat transfer from the particle to the gas mixture as a result of convection and conduction.

Governing Solid-Phase Equations. In this subsection, the governing equations describing mass transport and chemical reactions in the solid phase (the char) are presented.

Particle Mass. The evolution of the carbonaceous part of the char particle mass m_c is described by

$$\frac{dm_c}{dt} = -S_t M_c R_{reac,c} \tag{4}$$

where M_c is the molar mass of carbon and $R_{reac,c}$ is the molar reaction rate of carbon. Because the heterogeneous reaction mechanism is intrinsic, the total surface area of the carbonaceous part of the particle, S_t, is required. This is in contrast to apparent reaction mechanisms, where the effect of the surface area is implicitly included in the reaction kinetics.

Particle Temperature. The temperature evolution of the char particle is given by

$$\frac{dT_p}{dt} = \frac{1}{m_p c_{p,p}}(Q_{reac} - Q_c + Q_{rad}) \tag{5}$$

where T_p is the particle temperature, $c_{p,p}$ is the specific heat capacity of the particle, Q_{reac} is the heating as a result of the heterogeneous reaction, Q_c is the heat transfer from the char particle to the gas phase via convection and conduction, and Q_{rad} is the heating as a result of radiation.[18]

Adsorbed Species. The number of moles of adsorbed species j is given by

$$N_j = C_{s,j} S_t \tag{6}$$

where $C_{s,j}$ is the concentration of adsorbed species j on the surface of the char particle. The rate of change in the site fraction of adsorbed species j is given by

$$\frac{d\Theta_j}{dt} = \frac{R_{spec,j}}{\xi_n} + A R_{reac,c} \Theta_j \tag{7}$$

where $\Theta_j = C_{s,j}/\xi_n$ is the adsorbed species site fraction and ξ_n is the total surface concentration of carbon sites (both free and occupied). The molar rate of adsorbed species production is given by $R_{spec,j}$, while A is an active surface area.[15]

Species Concentrations at the Particle Surface. The relationship between the flux of gas-phase species i through the boundary layer to the external particle surface and the net production of species i via particle−gas reactions, in steady state, is given by

$$\dot{n}_i - X_{i,s}\dot{n}_{total} = -k_{im}(X_{i,\infty} - X_{i,s}) \tag{8}$$

where $X_{i,\infty}$ is the mole fraction of species i in the ambient gas phase and $X_{i,s}$ is the mole fraction of species i at the particle surface. The species mass transfer coefficient is represented by k_{im}. The molar flux of species i, $\dot{n}_i$, is defined as positive in the direction away from the particle surface, such that the total molar flux away from the particle is given by $\dot{n}_{total} = \sum \dot{n}_i$. A Newton method is used to solve eq 8.

Internal Particle Burning and the Effectiveness Factor. The molar rate of reaction k is given by

$$R_{reac,k} = k_k \prod_{i=1}^{N_{s,gas}+N_{s,ads}} C_i^{\nu_{i,k}} \tag{9}$$

where k_k is the rate coefficient of reaction k. The concentration of species i is represented by C_i, while $\nu_{i,k}$ is the stoichiometric coefficient. This equation is valid when the concentration of reactants of reaction k inside the particle is uniform. In a situation where the mass transport rates are slower than the chemical reaction rates, the gas does not penetrate the particle completely. As a result, the concentration of reactants inside the particle is not uniform and the rate of reaction k is lower than what is found from eq 9. The reduced rate of reaction k can be written as

$$R_{reac,k} = \eta_k k_k \prod_{i=1}^{N_{s,gas}+N_{s,ads}} C_i^{\nu_{i,k}} \tag{10}$$

where

$$\eta_k = \frac{3}{\phi}\left[\frac{1}{\tanh(\phi)} - \frac{1}{\phi}\right] \tag{11}$$

is the effectiveness factor of reaction k and ϕ is the Thiele modulus.[19]

The evolution of the particle radius versus density is also handled on the basis of the effectiveness factor, as described by Haugen et al.[3]

RESULTS

To investigate the effect of molecular hydrogen in the gas phase on the heterogeneous reactions, the heterogeneous reactions containing molecular hydrogen as a reactant are either activated or deactivated. The reactions are deactivated by setting their reaction rates to zero. All other conditions are kept unchanged. The first relevant reaction is the reverse part of reaction R3, which in the following is referred to as R3b:

$$H_2 + 2C_f \rightarrow C(H) + C(H) \tag{12}$$

DOI: 10.1021/acs.energyfuels.6b00502
Energy Fuels 2016, 30, 4411−4418

where two free carbon sites on the particle surface and a hydrogen molecule react to become two adjacent carbon sites that each have an adsorbed hydrogen atom. The other relevant reaction is the forward part of reaction R7 (R7f)

$$C_b + C_f + C(H) + H_2 \rightarrow CH_3 + 2C_f \quad (13)$$

where the free carbon site adsorbs the hydrogen molecule from the gas phase. During the process of reaction, the hydrogen molecule moves, binds to the hydrogen atom adsorbed on the carbon site C(H), and desorbs and leaves the particle as CH_3. An underlying bulk carbon becomes a free carbon site.

By turning on and off reactions R3b and R7f, four different test cases can be defined, as presented in Table 4. The purpose of this paper is to investigate the impact of H_2 in the gas phase on the time that is needed to reach full conversion of the char particle and to understand the reasons of this impact. It is assumed that full conversion of a particle is reached when 99% of the solid carbon has been converted.

Table 4. Studied Cases A, B, C, and D[a]

case	R3b	R7f
case A	on	on
case B	off	on
case C	on	off
case D	off	off

[a]Reaction R3b, $H_2 + 2C_f \rightarrow C(H) + C(H)$, and reaction R7f, $C_b + C_f + C(H) + H_2 \rightarrow CH_3 + 2C_f$, are simulated to be active or not active.

In the following, the impact of hydrogen in the gas phase on char gasification at low, intermediate, and high temperatures is studied. It is assumed that the temperatures of the fluid and the particles inside the reactor during the conversion process is constant. Small char particles, with Stokes numbers less than unity, are used. Furthermore, the reactor is assumed to be perfectly stirred within a small sub-volume following the particles, such that both species and particles are homogeneously distributed within this sub-volume. This means that the char particles stay within the fluid element into which they where injected throughout the course of conversion. As such, the process can be thought of as a batch process for each particle, even though the reactor itself is continuous. The exception from the homogeneity of the simulation domain is the thin boundary layer around each char particle, where gradients in gas-phase species exist as described by eq 8. It is clear that the assumption of a constant gas temperature is not valid in a real application; this assumption is nevertheless made to more clearly see the effect of the temperature on the reactions and, correspondingly, also on the amount of hydrogen inhibition.

It should also be noted that in real gasification of coal, the properties of the char will depend upon the conditions under which the char was formed. This effect is not accounted for here, and all char samples have been formed under the same conditions.

Conversion of the char particle exposed to the conditions shown in Table 5 and reacting according to the set of reactions presented in Table 1 describe the base case simulation (case A). See Table 4 for a description of the other cases (B, C, and D).

The time to reach full conversion as a function of the temperature is shown in Figure 1. The time to reach full conversion is symbolized by τ. At high temperatures ($T > 1900$ K), it takes less than 1 s to reach full conversion. It can also be seen that, in the temperature range of 1150−2000 K, the full conversion is reached faster for cases B and D than for cases A and C. At low temperatures ($T < 1400$ K), it can be observed that τ is longer for case C than for case A. In the temperature range of 2000−2650 K, it takes longer to reach full conversion for cases B and D than for cases A and C. On the basis of this, it is clear that the impact of hydrogen on the char gasification strongly depends upon the gasification temperature.

Table 5. Properties for the Simulation at a Constant Temperature Inside the Reactor

property	value	unit
carbon/gas mole ratio	0.5	
reactor wall temperature	700	K
pressure	2.4×10^6	Pa
initial particle radius	5.0×10^{-5}	m
initial particle density	1300	kg/m^3
initial mole fraction of H_2O	0.50	
initial mole fraction of O_2	0.45	
initial mole fraction of N_2	0.05	

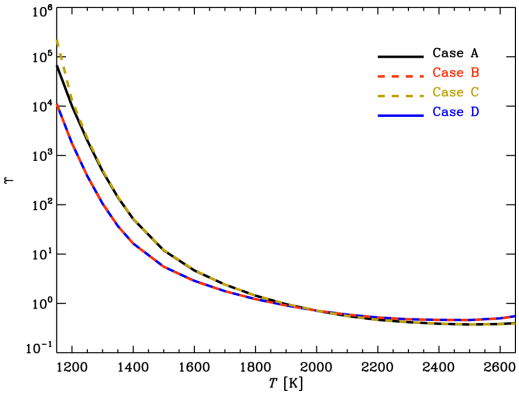

Figure 1. Time to reach full conversion of the char as a function of the temperature.

Let us now compare the time that it takes for the char to reach full conversion in each case, where one of the hydrogen reactions (cases B and C) or both of them (case D) are deactivated, with the time it takes to reach full conversion in the base case (case A), in different temperatures. This relationship can be expressed by the ratio of the time to reach full conversion in cases B, C, and D, respectively, to the time to reach full conversion in case A. These ratios are symbolized by α and can be written as

$$\alpha_B = \frac{\tau_B}{\tau_A}, \quad \alpha_C = \frac{\tau_C}{\tau_A}, \quad \text{and} \quad \alpha_D = \frac{\tau_D}{\tau_A} \quad (14)$$

when τ_A, τ_B, τ_C, and τ_D represent the time to reach full conversion in cases A, B, C, and D, respectively.

In Figure 2, the relative time to reach full conversion of the char as a function of the temperature for cases with (black line) and without (colored lines) hydrogen reactions is shown. It can be seen that α_B and α_D increase with an increasing temperature, reach unity at about 2000 K, and continue to increase. It is also seen that α_C decreases with an increasing temperature, reaches unity at about 1400 K, and remains equal to unity at higher temperatures.

DOI: 10.1021/acs.energyfuels.6b00502
Energy Fuels 2016, 30, 4411−4418

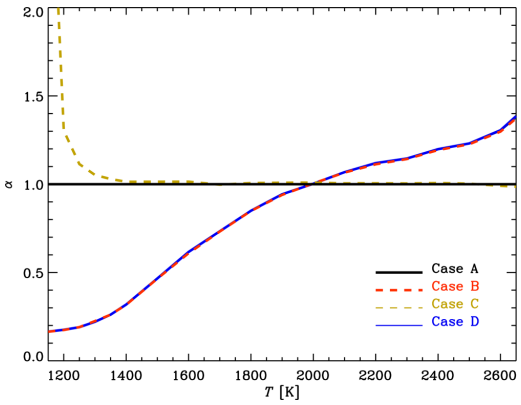

Figure 2. Relative time to reach full conversion of the char as a function of the temperature.

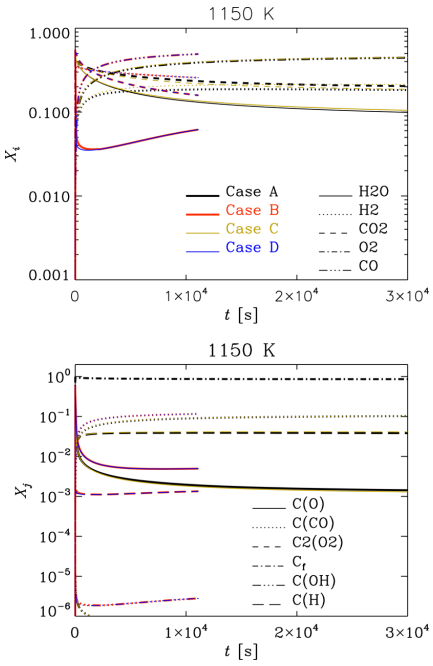

Figure 3. Gas-phase species fraction X_i (top panel) and surface fraction X_j of adsorbed species (bottom panel) as a function of time at a temperature of 1150 K.

By comparison of cases A and B, it is seen that hydrogen in the gas phase inhibits char gasification at low and intermediate temperatures (T < 2000 K), while hydrogen speeds up the gasification process at high temperatures (T > 2000 K). By comparison of cases B and D, it also seems clear that reaction R7f does not have a significant impact on the results and, hence, that the hydrogen inhibition is primarily due to reaction R3b.

To study the exact mechanism behind the impact of hydrogen on char gasification, the gasification process has been studied in detail for three selected temperatures. The lowest temperature (1150 K) corresponds to the lowest temperature for which full conversion could be reached; the intermediate temperature (2000 K) corresponds to the temperature where the time to reach full conversion both with and without the hydrogen reactions turned on are equal; and the higher temperature (2650 K) corresponds to the highest temperature where a numerical result could be obtained.

The mechanism employed in this work is designed to study the process of gasification at low and intermediate temperatures. However, in this section, the mechanism has been used to simulate char gasification in a much wider temperature range. It will later become evident when studying the species production rates that the heterogeneous mechanism is "unstable" at very high temperatures of ∼2600 K. This clearly means that the mechanism cannot be fully trusted at these high temperatures. These problems do not, however, seem to have any substantial impact on the overall results. By "unstable", it is meant that the simulation code is not able to identify one single solution but rather jumps between two neighboring possible solutions.

Gasification at 1150 K. At a temperature of 1150 K, turning off reaction R3b slows the overall production of C(H), which is seen by comparing cases A and B in Figure 3. Because C(H) is a reactant in reaction R1b, $2C_f + H_2O \leftrightarrow C(OH) + C(H)$, and reaction R2b, $C(OH) + C_f \leftrightarrow C(O) + C(H)$, the molar rate of both reactions R1 and R2 is higher when reaction R3b is deactivated. The net result of this is that more C(O) is produced, which leads to higher molar rates of reaction R4, $C(O) + C_b \rightarrow CO + C_f$, reaction R10b, $CO_2 + C_f \leftrightarrow C(O) + CO$, and reaction R11, $C_b + CO_2 + C(O) \rightarrow 2CO + C_f$. In reactions R4 and R11, a carbon atom is removed from the solid surface, and as such, these reactions have a positive impact on the conversion rate of the char. Because reaction R10 is neutral with respect to its impact on the conversion, the increased conversion rate of the char when reaction R3b is turned off is due to the higher amount of adsorbed oxygen on the surface when there is less adsorbed hydrogen present.

When reaction R7f is deactivated, we see from eq 2 that the time to reach full conversion increases for very low temperatures. The reason for this is 2-fold: first, the deactivation of reaction R7f yields a higher concentration of adsorbed hydrogen, which, as described in the previous paragraph, has a negative effect on the rate of conversion. It can, however, be seen from Figure 3 that the levels of adsorbed hydrogen and oxygen are rather similar for cases A and C, such that this effect is not expected to be significant. Second, because reaction R7f removes one carbon from the solid surface, the deactivation of this reaction will also reduce the rate of conversion directly. This is probably the main reason for the longer times to reach full conversion when reaction R7f is turned off for temperatures less than 1400 K.

Gasification at Higher Temperatures. In this section, the gasification characteristics at temperatures of 2000 and 2650 K are presented. It should be noted that, at these high temperatures, the assumption that the ash cannot evaporate is no longer valid.

From Figure 2, it can be seen that the deactivation of reaction R3b, at a temperature of 2000 K, does not influence the net rate of conversion. The main reason that the deactivation of reaction R3b does not have an effect at this

DOI: 10.1021/acs.energyfuels.6b00502
Energy Fuels 2016, 30, 4411−4418

temperature, even though the effect was substantial at 1150 K, is that the deactivation of reaction R3b no longer has an effect on the amount of adsorbed oxygen on the particle surface. This can be seen by comparing cases A and B in the lower panel of Figure 4.

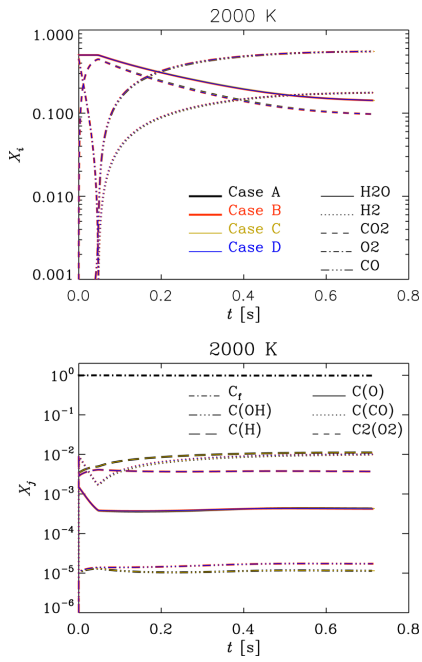

Figure 4. Gas-phase species fraction X_i (top panel) and surface fraction X_j of adsorbed species (bottom panel) as a function of time at a temperature of 2000 K.

As a result of the lower concentration of C(H), reaction R8 slows. This does not have an effect on the char conversion rate, because reaction R8 does not change the number of carbon atoms on the surface, but it does affect the net production rate of CO and HCO. This can be seen by comparing cases A and B in Figure 5. On the basis of the above, it may at first glance seem surprising that the molar concentrations of CO and HCO in the gas phase are still unchanged. This is however due to the fact that these species are converted through the homogeneous reactions to obtain chemical equilibrium in the gas phase. At these high temperatures, gas-phase chemical equilibrium is obtained at a time scale significantly shorter than the time scale for char conversion.

In Figure 4, the gas-phase species concentration X_i and surface species concentration X_j as a function of time at a temperature of 2000 K is shown. The gas phase reaches chemical equilibrium because the difference between the fractions of each species cannot be seen. The important difference is between cases A and B for the concentration of hydrogen adsorbed on the particle surface, which is higher in case A, because C(H) is not produced as a result of reaction R3b.

By studying Figure 6, it can be seen that several of the adsorbed species fractions make abrupt and seemingly

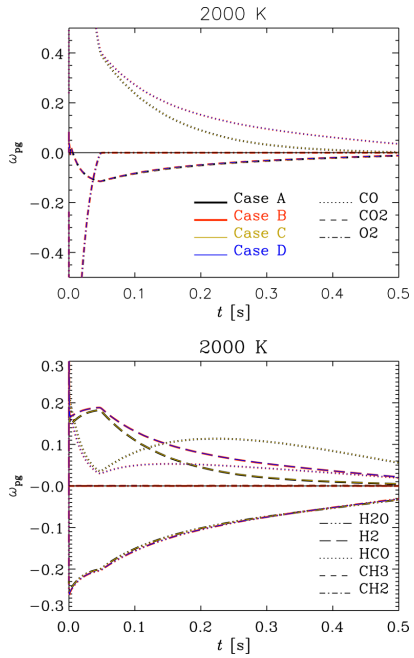

Figure 5. Species production rate ω_{pg} as a result of the gas−particle reactions as a function of time at a temperature of 2000 K.

unphysical jumps. Because smooth numerical results are no longer obtained, this indicate that a temperature of 2650 K is outside the temperature range for which the heterogeneous mechanism can be used. The reason for these jumps in adsorbed species fractions is probably that there exist two different solutions that both satisfy the governing equations at these rather extreme conditions. The numerical solver then ends up jumping between these two solutions, which yields the observed jumps in adsorbed species fractions.

Gasification at Very Low Temperatures. At low temperatures, global chemical equilibrium dictates that full conversion of the char will not be obtained. For the conditions presented in Table 5, it is found that the char is fully converted for $T > 1150$ K. Below this temperature, only a fraction of the char will be converted as $t \rightarrow \infty$.

The fraction of the char that becomes converted is visualized by the solid lines in Figure 7. Here, it is seen that the amount of conversion decreases with the temperature for all cases but that the cases when reaction R3b is turned off always yield more conversion. The explanation for this is the same as before, namely, that less adsorbed hydrogen on the surface yields more adsorbed oxygen and, hence, more char conversion through reaction R4. The conversions shown here are obtained as time goes toward infinity, i.e., at chemical equilibrium. Hence, these results can be compared to results from chemical equilibrium solvers. Here, GASEQ[20] and Cantera[21] have been used to simulate the equilibrium condition. These results are visualized by the deep red dashed−dotted line and the black dashed line in Figure 7. From this, it is seen that the results for the two equilibrium solvers are almost identical, as expected, and that the trends obtained from the equilibrium solvers are similar to

DOI: 10.1021/acs.energyfuels.6b00502
Energy Fuels 2016, 30, 4411−4418

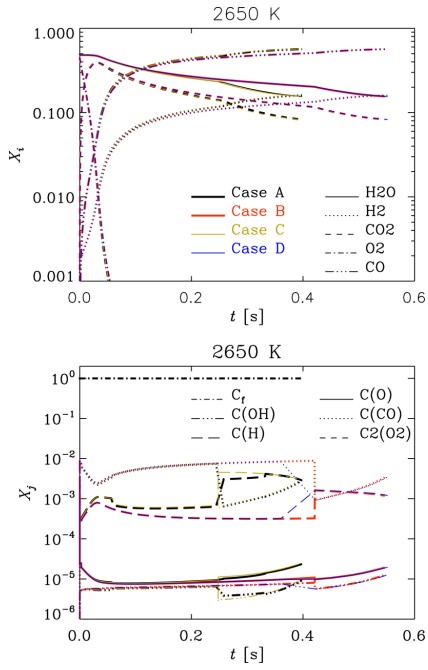

Figure 6. Gas-phase species fraction X_i (top panel) and surface fraction X_j of adsorbed species (bottom panel) as a function of time at a temperature of 2650 K.

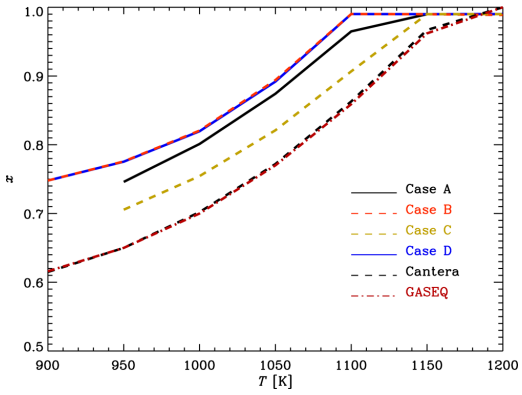

Figure 7. Conversion as a function of the temperature for different cases and two different equilibrium solvers.

what is found for cases A–D. The equilibrium solvers do, however, always yield a slightly lower conversion. Because one or more of the reactions are turned off in cases B–D, these cases are not expected to yield results similar to the equilibrium solvers. This is not true for case A, however. The reason for the discrepancy between the equilibrium solvers and case A is the fact that the equilibrium solvers do not take the adsorbed species into account. This means that the enthalpies and entropies of the char in the equilibrium solvers are not the same as in our main solver; hence, the Gibbs free energy and, correspondingly, also the equilibrium condition are different.

SUMMARY

In this work, the newly developed detailed chemical kinetics model of Tilghman and Mitchell[1] has been used to study the mechanisms behind hydrogen inhibition and speed up of char gasification. For the conditions studied here, it is clearly seen that hydrogen inhibition is found for $T < 2000$ K, while for $T > 2000$ K, hydrogen in the gas phase speeds up the char conversion. By studying the species reaction rates together with the individual rate of every single reaction, it is shown that hydrogen inhibition at low and intermediate temperatures is due to atomic hydrogen adsorbed on the char surface interacting with atomic oxygen on the surface to form an adsorbed OH molecule. The adsorbed OH molecule combines with another adsorbed hydrogen atom to form gaseous water. The outcome of this is that adsorbed atomic oxygen, which would normally desorb as gaseous CO while removing a carbon atom from the surface, only takes part in the production of steam, which does not yield any char conversion, and hence, the time to reach full conversion is increased as a result of the presence of hydrogen. This conclusion differs from the findings of Pineda and Chen,[4] who found that hydrogen inhibition is mainly due to the blocking of active sites by adsorbed hydrogen. This discrepancy may be explained by the fact that adsorbed OH was not a part of of their mechanism.

It has also been shown that, at higher temperatures, the presence of hydrogen results in a speed up of the char conversion. This is primarily due to reaction 6f, where adsorbed hydrogen reacts with steam to produce oxygen adsorbed on the surface. As a result of the higher concentration of C(O), the process of removing carbon from the surface is faster.

AUTHOR INFORMATION

Corresponding Author

*E-mail: nils.e.haugen@sintef.no.

Notes

The authors declare no competing financial interest.

ACKNOWLEDGMENTS

This work forms part of the CAMPS project supported by the Research Council of Norway (215707). The work has additionally been produced with support from the BIGCCS Centre, performed under the Norwegian Research Program Centres for Environment-Friendly Energy Research (FME). The author acknowledges the following partners for their contributions: Aker Solutions, ConocoPhillips, Gassco, Shell, Statoil, TOTAL, GDF SUEZ, and the Research Council of Norway (193816/S60). The research leading to these results has received funding from the Polish–Norwegian Research Programme operated by the National Centre for Research and Development under the Norwegian Financial Mechanism 2009–2014 in the frame of Project Contract Pol-Nor/232738/101/2014. Nils Erland L. Haugen also acknowledges the Research Council of Norway under the FRINATEK Grant 231444. This work has also benefitted from the WoodCFD project, which is funded by: Dovre AS, Norsk Kleber AS, Jøtulgruppen and Morsø AS together with the Research Council of Norway through the ENERGIX program (243752/E20).

DOI: 10.1021/acs.energyfuels.6b00502
Energy Fuels 2016, 30, 4411–4418

REFERENCES

(1) Tilghman, M. B.; Mitchell, R. E. Coal and biomass char reactivities is gasification and combustion environments. *Combust. Flame* **2015**, *162*, 3220−3235.

(2) Hecht, E. S.; Shaddix, C. R.; Molina, A.; Haynes, B. S. Effect of CO_2 gasification reaction on oxy-combustion of pulverized coal char. *Proc. Combust. Inst.* **2011**, *33*, 1699−1706.

(3) Haugen, N. E. L.; Mitchell, R. E.; Tilghman, M. B. The conversion mode of a porous carbon particle during oxidation and gasification. *Combust. Flame* **2014**, *161*, 612.

(4) Pineda, D. I.; Chen, J.-Y. Modeling hydrogen inhibition in gasification surface reactions. *Int. J. Hydrogen Energy* **2015**, *40*, 6059.

(5) Laurendeau, N. M. Heterogeneous kinetics of coal char gasification and combustion. *Prog. Energy Combust. Sci.* **1978**, *4*, 221−270.

(6) Gadsby, J.; Hinshelwood, C. N.; Sykes, K. W. The Kinetics of the Reactions of the Steam-Carbon System. *Proc. R. Soc. London, Ser. A* **1946**, *187*, 129−151.

(7) Johnstone, H. F.; Chen, C. Y.; Scott, D. S. Kinetics of the steam-carbon reaction in porous graphite tubes. *Ind. Eng. Chem.* **1952**, *44* (7), 1564−1569.

(8) Biederman, D. L.; Miles, A. J.; Vastola, F. J.; Walker, P. L., Jr. Carbon-carbon dioxide reaction: kinetics at low pressures and hydrogen inhibition. *Carbon* **1976**, *14*, 351−356.

(9) Hüttinger, K. J.; Merdes, W. F. The carbon-steam reaction at elevated pressure: formations of product gases and hydrogen inhibitions. *Carbon* **1992**, *30* (6), 883−894.

(10) Barrio, M.; Gøbel, B.; Rimes, H.; Henriksen, U.; Hustad, J. E.; Sørensen, L. H. Steam gasification of wood char and the effect of hydrogen inhibition on the chemical kinetics. In *Progress in Thermochemical Biomass Conversion*; Bridgwater, A. V., Ed.; Blackwell Science, Ltd.: Oxford, U.K., 2001; Chapter 2, pp 32−46, DOI: 10.1002/9780470694954.ch2.

(11) Mühlen, H.-J.; van Heek, K. H.; Jüntgen, H. Kinetic studies of steam gasification of char in the presence of H_2, CO_2 and CO. *Fuel* **1985**, *64* (7), 944−949.

(12) Moilanen, A.; Mühlen, H.-J. Characterization of gasification reactivity of peat char in pressurized conditions effect of product gas inhibition and inorganic material. *Fuel* **1996**, *75* (11), 1279−1285.

(13) Tay, H.-L.; Kajitani, S.; Zhang, S.; Li, C.-Z. Inhibiting and other effects of hydrogen during gasification: Further insights from FT-Raman spectroscopyl. *Fuel* **2014**, *116*, 1−6.

(14) Fushimi, C.; Wada, T.; Tsutsumi, A. Inhibition of steam gasification of biomass char by hydrogen and tar. *Biomass Bioenergy* **2011**, *35* (1), 179−185.

(15) Haugen, N. E. L.; Mitchell, R. E.; Tilghman, M. B. A comprehensive model for char particle conversion in environments containing O_2 and CO_2. *Combust. Flame* **2015**, *162*, 1455−1463.

(16) Haynes, B. S. A turnover model for carbon reactivity I. development. *Combust. Flame* **2001**, *126*, 1421−1432.

(17) *GRI-Mech 3.0*; http://combustion.berkeley.edu/gri_mech/overview.html (accessed Aug 2014).

(18) Haugen, N. E. L.; Mitchell, R. E. Modeling radiation in particle clouds: On the importance of inter-particle radiation for pulverized solid fuel combustion. *Heat Mass Transfer* **2015**, *51*, 991−999.

(19) Thiele, E. W. *Ind. Eng. Chem.* **1939**, *31*, 916.

(20) GASEQ. http://www.gaseq.co.uk/.

(21) *Cantera*; https://en.wikipedia.org/wiki/Cantera.

DOI: 10.1021/acs.energyfuels.6b00502
Energy Fuels 2016, 30, 4411−4418

5.4 Paper 4

The effect of turbulence on mass and heat transfer rates of small inertial particles

Nils Erland. L. Haugen, Jonas Krüger, Dhrubaditya Mitra and Terese Løvås
Submitted to Journal of Fluid Mechanics

The effect of turbulence on mass and heat transfer rates of small inertial particles

Nils Erland L. Haugen[1,2], Jonas Krüger[1], Dhrubaditya Mitra[3] and Terese Løvås[1]

[1]Department of Energy and Process Engineering, Norwegian University of Science and Technology, Kolbjørn Hejes vei 1B, NO-7491 Trondheim, Norway
[2]SINTEF Energy Research, N-7465 Trondheim, Norway
[3]Nordita, KTH Royal Institute of Technology and Stockholm University, Roslagstullsbacken 23, SE-10691 Stockholm, Sweden

(Received)

The effect of turbulence on the mass and heat transfer between small heavy inertial particles (HIP) and an embedding fluid is studied. Two effects are identified. The first effect is due to the relative velocity between the fluid and the particles, and a model for the relative velocity is presented. The second effect is due to the clustering of particles, where the mass transfer rate is inhibited due to the rapid depletion of the consumed species inside the dense particle clusters. This last effect is relevant for large Damköhler numbers and it may totally control the mass transfer rate for Damköhler numbers larger than unity. A model that describes how this effect should be incorporated into existing particle simulation tools is presented.

Key words: Reacting multiphase flow, Particle/fluid flow, Combustion, Turbulent reacting flows, Turbulence simulations

1. Introduction

Both in nature and in industrial applications, one regularly finds small inertial particles embedded in turbulent flows. By small inertial particles, we mean particles that are smaller than the smallest scales of the turbulence and have significantly higher material density than the fluid. For such particles, there will be momentum exchange between the particles and the turbulent fluid, and, depending on the conditions, there may also be heat and mass transfer. This is particularly so for chemically reacting particles, but there are also a large number of other applications where heat and mass transfer between particles and fluid are important. Here, the main focus will be on reacting particles that consume one or more of the species in the embedding gas through surface reactions. Relevant examples are; chemical reactions on the surface of a catalytic particle, fuel oxidation on the surface of a oxygen carrying particle in a Chemical Looping Combustion (CLC) reactor, condensation of water vapor on cloud droplets and combustion or gasification of char.

The presence of turbulence in a fluid will enhance the transport properties of the flow. This means that the mean-field viscosity, diffusivity and conductivity may be drastically increased from their laminar values. This effect has been studied for many years, and a large number of different models exist in the literature, such as the k-ϵ model (Jones & Launder (1972)) and different versions of the Reynolds Stress Models (e.g. Pope (2003)). Turbulence may also modify gas phase combustion, and even though this is somewhat more complicated, a significant number of models have been developed during the last decades. Some examples are the Eddy Dissipation Model (Magnussen & Hjertager (1976)), the Eddy Dissipation Concept (Ertesvåg & Magnussen (2000)) and variations of Probability Density Function (e.g. Dopazo (1994)) models.

With the above knowledge in mind, it is interesting to realize that, except for the recent work

of Kruger et al. (2016), there is currently no model describing the effect of turbulence on the heat and mass transfer of small inertial particles. When a reacting particle is embedded in a turbulent flow, the turbulence can potentially influence the mass transfer, and hence the surface reaction rates in two ways. The first way is through particle clustering, where particles form dense clusters due to turbulence, and where the gas phase reactants within the cluster are quickly consumed while there are no particles that can consume the reactants in the particle voids outside the clusters. The main effect of the clustering is to *decrease* the overall mass transfer rate. The second way turbulence influence the mass transfer rate is by increasing the mean velocity difference between the particle and the gas. This effect will *increase* the mass transfer rate.

The same two effects are also active for the heat transfer. The similarity between heat and mass transfer can be seen by considering the expressions for the transfer coefficients of mass

$$\kappa = \frac{\mathrm{Sh}D}{d_p} \tag{1.1}$$

and heat

$$\kappa_{\mathrm{th}} = \frac{\mathrm{Nu}D_{\mathrm{th}}}{d_p}, \tag{1.2}$$

where d_p is the particle radius, Sh and Nu are the Sherwood and Nusselt numbers and D and D_{th} are the mass and thermal diffusivities. For single spherical particles in flows with low and medium particle Reynolds numbers, the Sherwood and Nusselt numbers can be approximated by the empirical expressions of Ranz & Marshall (1952)

$$\begin{aligned} \mathrm{Sh}_{\mathrm{RM}} &= 2 + 0.69\mathrm{Re}_p^{1/2}\mathrm{Sc}^{1/3} \\ \mathrm{Nu}_{\mathrm{RM}} &= 2 + 0.69\mathrm{Re}_p^{1/2}\,\mathrm{Pr}^{1/3}. \end{aligned} \tag{1.3}$$

A well known example where reacting particles are consumed in a turbulent fluid is the case of pulverized coal combustion, where turbulence influences the process in several ways that are understood to varying degrees. The combustion of coal can be divided into four separate processes; 1) drying, 2) devolatilization, 3) combustion of volatiles and 4) burnout of the remaining char. Processes 1 and 2 involve the evaporation of fluids and thermal cracking of hydrocarbons, while process 3 involves homogeneous reactions. In process 4, gas phase species diffuse to the particle surface and react with the solid carbon. This happens via adsorption of e.g. an oxygen radical to a carbon site on the particle surface and a subsequent desorption of carbon monoxide into the gas phase. This makes process 4 dominated by heterogeneous chemical reactions. Many published studies utilize RANS based simulation tools that describe simulations of pulverized coal conversion in the form of combustion or gasification with an Eulerian-Eulerian approach (Gao et al. (2004) and Zhang et al. (2005)) or a Lagrangian-Eulerian approach (Silaen & Wang (2010); Vascellari et al. (2014, 2015); Klimanek et al. (2015); Chen et al. (2012, 2000)). However, none of these papers take the effect of turbulence on the heterogeneous char reactions into account. To the knowledge of the authors, the only studies where account is made for this effect are the papers of Luo et al. (2012); Brosh & Chakraborty (2014); Brosh et al. (2015) and Hara et al. (2015) where the Direct Numerical Simulations (DNS) approach is used. In a DNS, all turbulence scales are explicitly resolved on the computational grid, such that the effect of turbulence is implicitly accounted for. However, the DNS approach is extremely costly and can therefore only be used for small simulation domains. For simulations of large scale applications, the RANS or LES based simulation tools will therefore be the only applicable tools for the foreseeable future.

In the current paper, the same framework as was developed by Kruger et al. (2016) has been used and extended. The aim of the paper is to identify the effect of turbulence on the mass and

heat transfer of solid particles, and to develop models that describe this effect for all Damköhler numbers.

2. Mathematical model and implementation

In the current work, the so called point-particle direct numerical simulation (PP-DNS) approach is used. Here, the turbulent fluid itself is solved with the direct numerical simulation (DNS) methodology, where all turbulent scales are resolved and no modelling is needed. The particles are however not resolved, but rather treated as point particles where the fluid-particle momentum, mass and heat interactions are modelled. The point particle approach is a simplification that relies heavily on the quality of the models. The alternative approach, which is to resolve the particles and their boundary layer, is extremely CPU intensive and can currently not be done for more than a few hundred particles, even on the largest computers (Deen & Kuipers (2014)).

A number of simplifications are made in this paper. This has been done in order to make the simulations less CPU intensive, and, even more importantly, to isolate the dominating physical mechanisms. The particles are considered to be ever lasting, i.e. they are not consumed. The reaction on the particle surface is converting reactant A to product B;

$$A \rightarrow B \tag{2.1}$$

isothermally, i.e.; there is no production or consumption of heat, such that only the mass transfer effect is considered. As explained above, the effect on the heat transfer rate will be similar to the effect on the mass transfer rate. As reactant A is converted product B, the thermodynamical and transport properties are not changed.

2.1. *Fluid equations*

The equations determining the motion of the carrier fluid is give by the continuity equation

$$\frac{\partial \rho}{\partial t} + \nabla \cdot (\rho \boldsymbol{u}) = 0, \tag{2.2}$$

and the Navier–Stokes equation

$$\rho \frac{\mathrm{D}\boldsymbol{u}}{\mathrm{D}t} = -\boldsymbol{\nabla} P + \boldsymbol{\nabla} \cdot (2\mu \boldsymbol{S}) + \rho \boldsymbol{f} + \boldsymbol{F}. \tag{2.3}$$

Here, ρ, $\boldsymbol{u}$, $\mu = \rho\nu$ and ν are the density, velocity and dynamic and kinematic viscosities of the carrier fluid, respectively. The pressure P and the density ρ are related by the isothermal sound speed c_s, i.e.,

$$P = c_\mathrm{s}^2 \rho, \tag{2.4}$$

while the trace-less rate of strain tensor is given by

$$\boldsymbol{S} = \frac{1}{2}\left(\boldsymbol{\nabla u} + (\boldsymbol{\nabla u})^T\right) - \frac{1}{3}\boldsymbol{\nabla} \cdot \boldsymbol{u}. \tag{2.5}$$

Kinetic energy is injected into the simulation box through the forcing function f, which is solenoidal and non-helical and injects energy and momentum perpendicular to a random wave vector whose direction changes every time-step (Haugen et al. 2012; Kruger et al. 2016). Similar kinds of forcing has also previously been used for particle laden flows by other groups (Bec et al. 2007). The energy injection rate is maintained at a level such that the maximum Mach number is always below 0.5. The domain is cubic with periodic boundaries in all directions. The momentum exchange term, $\boldsymbol{F}$, is chosen to conserve momentum between the fluid and the solid particles, i.e.,

$$\boldsymbol{F} = -\frac{1}{V_\mathrm{cell}} \sum_\mathrm{k} m^k \boldsymbol{a}^k \tag{2.6}$$

when V_{cell} is the volume of the grid cell of interest and m^k and $\boldsymbol{a}^k$ are the mass and acceleration (due to fluid drag) of the k'th particle within the grid cell.

The equation of motion of the reactant has the well-known advection-reaction-diffusion form:

$$\frac{\partial X}{\partial t} + \nabla \cdot (X\boldsymbol{u}) = D\bar{M}_{\text{c}}\nabla \cdot (\nabla X) + \tilde{R}, \tag{2.7}$$

where X, $\bar{M}_{\text{c}}$ and D are the mole fraction, the mean molar mass and the diffusivity of the reactant, respectively. The last term in Eq. (2.7), $\tilde{R}$, is the sink term due to the gas-solid reactions on the surface of the solid particles.

2.2. *Particle equations*

The N_p particles that are embedded in the flow are treated as point particles, which means that they are assumed to be significantly smaller than the viscous scale of the fluid and the diffusive scale of the reactant. The motion of the k'th particle is described by the equations for position

$$\frac{d\boldsymbol{X}^{\text{k}}}{dt} = \boldsymbol{V}^{\text{k}} \tag{2.8}$$

and velocity

$$\frac{d\boldsymbol{V}^{\text{k}}}{dt} = \boldsymbol{a}^k \tag{2.9}$$

when the particle acceleration due to fluid drag is given by $\boldsymbol{a}^k = \frac{1}{\tau}\left[\boldsymbol{u}(\boldsymbol{X}^{\text{k}}) - \boldsymbol{V}^{\text{k}}\right]$. Note that gravity is neglected in this work. The particle response time is given by (Schiller & Naumann (1933))

$$\tau = \frac{\tau_{\text{St}}}{1 + f_c} \tag{2.10}$$

when $\tau_{\text{St}} = S\,d_p^2/18\nu$ is the Stokes time, $f_c = 0.15\text{Re}_p^{0.687}$ is a Reynolds number correction term to the classical Stokes time, $S = \rho_p/\rho$ is the density ratio, ρ_p is the material density of the particles,

$$\text{Re}_p = \frac{|\boldsymbol{u}(\boldsymbol{X}^{\text{k}}) - \boldsymbol{V}^{\text{k}}|d_p}{\nu} = \frac{u_{\text{rel}}d_p}{\nu} \tag{2.11}$$

is the particle Reynolds number and d_p is the particle diameter.

2.3. *Surface reactions*

Let us now model the reactive term. We assume that the reactions are limited to the surface of the particles and that the reactions are diffusion controlled, i.e. that all reactant that reaches the particle surface is consumed immediately†. The reactive term can then be written as

$$\tilde{R} = \frac{1}{V_{\text{cell}}}\sum_{\text{k}} A_p^k \kappa X_\infty^K \tag{2.12}$$

where $A_p = 4\pi r_p^2$ is the external surface area of the particle, the mass transfer coefficient is given by

$$\kappa = \frac{D\text{Sh}}{d_p} \tag{2.13}$$

and Sh is the Sherwood number.

To couple the reactive particle with the continuum equations we use the following prescription; for the k-th particle, which is at position $\boldsymbol{X}^{\text{k}}$, we set

$$X_\infty^k = X(\boldsymbol{X}^{\text{k}}), \tag{2.14}$$

† It is possible to relax the assumption of diffusion controlled reactions by also accounting for chemical kinetics at the particle surface, see Kruger et al. (2016).

i.e.; the far field reactant mole fraction is set equal to the reactant mole fraction of the fluid cell where the particle is. In the current work, the particle Sherwood number is determined by the expression of Ranz & Marshall (1952) (see Eq. (1.3) in the introduction), which is in contrast to the work of Kruger et al. (2016) where the Sherwood number was set to a constant value of 2, which corresponds to the Sherwood number in a quiescent flow. The particle Reynolds number is given by Eq. (2.11) and the Schmidt number, $\mathrm{Sc} = \nu/D$, is the ratio of the fluid viscosity and the mass diffusivity.

2.4. *The reactant consumption rate*

It is useful to define a reactant consumption rate as

$$\alpha = -\overline{\left(\frac{\tilde{R}}{X_\infty}\right)} = \overline{n_p A_p \kappa}, \tag{2.15}$$

when $\overline{O}$ represents the volume average of flow property O and n_p is the particle number density. If everything is assumed to be homogeneously distributed over the volume, the reactant consumption rate is given by

$$\alpha_{\mathrm{hom}} = n_p A_p \kappa = n_p A_p \frac{\mathrm{Sh} D}{d_p} \tag{2.16}$$

for a given particle size and number density.

In many RANS based simulation tools, where the local fluid velocity is not resolved, it is common to neglect the relative velocity difference between the turbulent eddies and the particles. This implies that $\mathrm{Sh} = 2$. Since the effect of particle clustering is also neglected in such models, the modelled reactant consumption rate becomes;

$$\alpha_{\mathrm{Sh,Da}} = \lim_{\mathrm{Sh}\to 2, \mathrm{Da}\to 0} \alpha = n_p A_p \frac{2D}{d_p}. \tag{2.17}$$

In the following, $\alpha_{\mathrm{Sh,Da}}$ will be used for normalization.

It is useful to define the Damköhler number, which is the ratio of the typical turbulent and chemical time scales, as

$$\mathrm{Da} = \frac{\tau_L}{\tau_c} \tag{2.18}$$

where $\tau_L = L/u_{\mathrm{rms}}$ is the integral time scale of the turbulence, L is the turbulent forcing scale, u_{rms} is the root-mean-square turbulent velocity and the chemical time scale is

$$\tau_c = 1/\alpha_{\mathrm{Sh,Da}}. \tag{2.19}$$

Particles in a turbulent flow field will tend to form clusters with higher particle number density than the average (Squires & Eaton 1991; Eaton & Fessler 1994; Toschi & Bodenschatz 2009; Wood et al. 2005). If the chemical time scale is short compared to the life-time of the clusters, the reactant concentration within the clusters will be much lower than outside the clusters. On the other hand, if the particle number density is low, the particle clusters will not have enough time to consume a significant fraction of the reactant during the life-time of the cluster, and hence, the reactant concentration will be roughly the same inside as it is outside the clusters. By assuming that the life-time of the clusters is of the order of the turbulent time scale, it is clear that the reactant concentration of particle flows with low Damköhler number will behave as if the particles were homogeneously distributed over the volume, i.e.; for small Damköhler numbers there is no effect of particle clustering on the reactant consumption.

From Eqs. (2.16) - (2.19) it can be deduced that for the homogeneous case, and then also for all cases with low Damköhler numbers, the reactant consumption rate will scale linearly with the

Damköhler number for a given turbulent flow field, such that

$$\alpha_{\text{hom}} = \frac{\text{Da}}{\tau_L}\frac{\text{Sh}}{2}. \tag{2.20}$$

When relaxing the restriction to small Damköhler numbers, the effect of particle clustering eventually comes into play. Kruger et al. (2016) have shown that the reactant consumption rate is given by

$$\alpha = \frac{\alpha_c \alpha_{\text{hom}}}{\alpha_c + \alpha_{\text{hom}}} \tag{2.21}$$

when α_c is a cluster dependent decay rate. (Note that since Kruger et al. assumed the Sherwood number to be 2, their α_{hom} equals our $\alpha_{\text{Sh,Da}} = \text{Da}/\tau_L$.) From this expression, the following normalized reactant consumption rate is found

$$\tilde{\alpha}_{\text{Sh}} = \frac{\alpha_{\text{Sh}}}{\alpha_{\text{Sh,Da}}} = \frac{\alpha_c \tau_L}{\alpha_c \tau_L + \text{DaSh}/2}\frac{\text{Sh}}{2}. \tag{2.22}$$

when Sh is given by Eq. (1.3) and the corresponding relative velocity between the particle and the fluid is determined by a model (which will be obtained in the next subsection). For diffusion controlled reactions, the modified reaction decay rate, as given by Eq. (2.22), is a measure of the relative modification to the mass transfer rate due to the effect of turbulence. This means that a modified Sherwood number can now be defined that accounts for the effect of turbulence;

$$\text{Sh}_{\text{mod}} = 2\tilde{\alpha}. \tag{2.23}$$

In the limit of small Damköhler numbers, this expression reduces to $\text{Sh}_{\text{mod}} = \text{Sh}$, as expected.

By employing the modified Sherwood number given by Eq. (2.23), one can now use the common expression for the reactant consumption rate, as given by Eq. (2.16), to find the real reactant consumption rate. In most cases, however, one needs the particle conversion rate $\dot{n}_{\text{reac}}$ for individual particles, which is closely connected to the reactant decay rate. For diffusion controlled mass transfer, the particle conversion rate is given by $\dot{n}_{\text{reac}} = -\kappa X_\infty C_g$, where C_g is the molar concentration of the gas phase and the mass transfer coefficient is now found by using the modified Sherwood number (as given by Eq. (2.23)) in; Eq. (1.1)

$$\kappa = \frac{D\text{Sh}_{\text{mod}}}{d_p}. \tag{2.24}$$

In many applications, the mass transfer rate is not purely diffusion controlled. This can be accounted for by including the effect of reaction kinetics at the particle surface. The corresponding particle conversion rate can then be expressed as (Kruger et al. 2016)

$$\dot{n}_{\text{reac}} = -\frac{\lambda\kappa}{\lambda + \kappa} X_\infty C_g, \tag{2.25}$$

where λ is the surface specific molar conversion rate. Since the reaction kinetics is only dependent on the conditions at the particle surface, the surface specific molar conversion rate is not affected by the turbulence. This is, as we have already seen, not the case for the mass transfer coefficient, which is now given by Eq. (2.24). In this way, all the common machinery for calculating particle reaction rates can still be used since the effects of the turbulence are incorporated into the modified Sherwood number.

3. Results

In all of the following, statistically stationary homogeneous and isotropic turbulence is considered. The Reynolds number is varied by changing the domain size while maintaining constant

TABLE 1. Summary of the simulations. The fluid density is unity while the Schmidt number is 0.2 and the viscosity is 2×10^{-4} m^2/s for all the simulations. For every simulation listed here, a range of identical simulations with different Damköhler numbers have been performed.

Label	L (m)	N_{grid}	d_p	ρ_p	Re	Sh	St	τ_L	α_c	$\alpha_c \tau_L Sh/St$
1A	$\pi/2$	64^3	3.4×10^{-3}	50	80	2.5	1.0	1.6	0.9	0.63
2A	2π	128^3	19×10^{-3}	50	400	2.8	1.0	5	0.23	0.43
3A	8π	256^3	11×10^{-3}	500	2200	2.8	1.0	15	0.07	0.41
2AB	2π	128^3	19×10^{-3}	25	400	2.7	0.5	5	0.26	0.25
3AB	8π	256^3	11×10^{-3}	250	2200	2.6	0.5	15	0.09	0.26
2B	2π	128^3	11×10^{-3}	50	400	2.5	0.3	5	0.21	0.13
3B	8π	256^3	11×10^{-3}	150	2200	2.6	0.3	15	0.09	0.18
2C	2π	128^3	19×10^{-3}	5	400	2.4	0.1	5	0.55	0.12
3C	8π	256^3	11×10^{-3}	50	2200	2.4	0.1	15	0.20	0.13
2D	2π	128^3	19×10^{-3}	1.5	400	2.3	0.03	5	1.20	0.08
3D	8π	256^3	11×10^{-3}	16	2200	2.3	0.03	15	0.45	0.10
2E	2π	128^3	19×10^{-3}	0.5	400	2.2	0.001	5	4.10	0.10

viscosity and turbulent intensity. The Damköhler number is varied by changing the number density of particles, while keeping everything else the same. All relevant simulations are listed in table 1.

3.1. *The mean relative particle velocity*

In order to predict a representative value of the particle Sherwood number from Eq. (1.3), the particle Reynolds number Re_p is required. From Eq. (2.11) it is clear that this also requires the relative particle velocity u_{rel}, which will be found in this subsection.

Given a particle with a response time that equals the Stokes time;

$$\tau_p = \frac{S d_p^2}{18\nu}, \tag{3.1}$$

such that $\tau_k < \tau_p < \tau_L$, where τ_k is the Kolmogorov time scale and τ_L is the integral time scale. With respect to the particle-turbulence interactions, the turbulent power spectrum may be divided into three distinct regimes, based on the relation between the particle response time and the turbulent eddy turnover time τ_{eddy}. The first regime is defined as the section of the turbulent power spectrum where the turbulent eddies have turnover times that are much larger than the response time of the particles, i.e. where $\tau_{\text{eddy}} \gg \tau_p$. All the turbulent eddies in this regime will see the particles as passive tracers, which follow the fluid perfectly. I.e., there will be no relative velocity between the particles and the eddies. The third regime is defined as the part of the power spectrum where the turbulent eddies have much shorter time scales than the particles, i.e. where $\tau_{\text{eddy}} \ll \tau_p$. The eddies in regime three will see the particles as heavy bullets that move in straight lines, without being affected by the motion of the eddies. Hence, the velocity of these eddies will contribute to the relative particle-fluid velocity. The second regime is now defined as the relatively thin band in-between regimes one and three, where $\tau_{\text{eddy}} \approx \tau_p$. These are the eddies that are responsible for particle clustering, since they are able to accelerate the particles

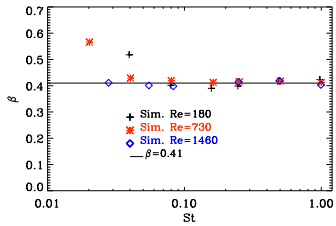

FIGURE 1. The parameter β, relating the relative particle velocity to the subscale velocity as defined in Eq. (3.9), is shown as a function of Stokes number.

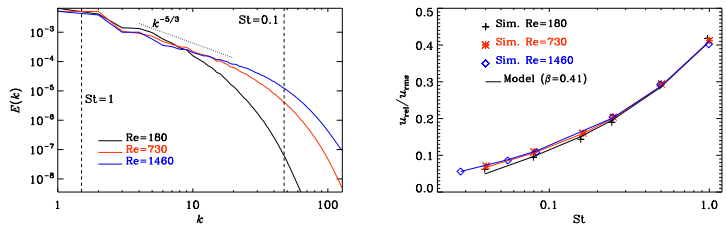

FIGURE 2. Left panel: kinetic energy spectrum for different Reynolds numbers. Right panel: relative particle velocity as a function of Stokes number.

to a level where they are thrown out of the eddy due to their inertia. In the following, we will refer to a typical eddy in regime two as a *resonant eddy*, and we define the scale of this eddy as ℓ. The resonant eddies are identified by their time scale, τ_ℓ, which is of the order of the particle response time, τ_p. For convenience, we set the two time scales equal, such that

$$\tau_\ell = \tau_p. \tag{3.2}$$

Based on the definitions above, it is clear that the largest turbulent eddies that yield a relative velocity between the fluid and the particles, are the resonant eddies. By assuming Kolmogorov scaling, the velocity of the resonant eddies is known to be $u_\ell = u_{\rm rms}(\ell/L)^{1/3}$, which can be combined with the above expression for the time scales to yield

$$k_\ell = k_L {\rm St}^{-3/2} \tag{3.3}$$

when the particle Stokes number is defined as

$${\rm St} = \frac{\tau_p}{\tau_L} \tag{3.4}$$

and $k_\ell = 2\pi/l$ and $k_L = 2\pi/L$ are the wave-numbers of the resonant eddies and the integral scale, respectively. In obtaining Eq. (3.3), it has also been used that the turnover time of the resonant eddies is $\tau_\ell = l/u_\ell$, while that of the integral scale eddies is $\tau_L = L/u_{\rm rms}$.

Since all scales smaller than ℓ will induce a relative velocity between the particles and the fluid, it is reasonable to assume that the relative velocity between the fluid and the particles will be a certain fraction β of the integrated turbulent velocity $\tilde{u}_\ell$ of all scales smaller than ℓ, such that

$$u_{\rm rel} = \beta \tilde{u}_\ell \tag{3.5}$$

when $\tilde{u}_\ell$ is defined as

$$\frac{1}{2}\tilde{u}_\ell^2 = \int_{k_\ell}^{k_\eta} E(k)dk \tag{3.6}$$

and $k_\eta = 2\pi/\eta$ is the wave-number of the Kolmogorov scale ($\eta = (\nu^3/\epsilon)^{1/4}$), where ϵ is the dissipation rate of turbulent kinetic energy. Integration of Eq. (3.6) yields

$$\tilde{u}_\ell = u_{\rm rms}\sqrt{\frac{k_\ell^{-2/3} - k_\eta^{-2/3}}{k_L^{-2/3} - k_\eta^{-2/3}}} \tag{3.7}$$

for $E(k) = c\epsilon^{2/3}k^{-5/3}$ when it has been used that the total turbulent kinetic energy is given by

$$\frac{1}{2}u_{\rm rms}^2 = \int_{k_1}^{k_\eta} E(k)dk, \tag{3.8}$$

where k_1 is the wavenumber of the largest scale in the simulation. Combining Eqs. (3.3) and (3.7) with Eq. (3.5) finally yields

$$u_{\rm rel} = \beta u_{\rm rms}\sqrt{\frac{{\rm St}k_L^{-2/3} - k_\eta^{-2/3}}{k_L^{-2/3} - k_\eta^{-2/3}}}. \tag{3.9}$$

The unknown constant in this equation, β, can be determined numerically from Eq. (3.5), i.e. $\beta = u_{\rm rel}/\tilde{u}_\ell$. Here, $u_{\rm rel}$ is found directly from DNS simulations, while $\tilde{u}_\ell$ is calculated from Eq. (3.7). It is seen from figure 1 that β is close to 0.41 for most Stokes and Reynolds numbers. The main exception is for low Reynolds and Stokes numbers, where β is significantly larger. This can be understood by inspecting the left panel of figure 2, where it is seen that for Re = 180 and St < 0.1, we are already far into the dissipative subrange, where our model is not expected to be correct since it relies on a Kolmogorov scaling.

It is surprising to see that Eq. (3.9) reproduces the relative particle velocity for such low Stokes numbers, even for the smaller Reynolds numbers. This may be explained by reconsidering Eq. (3.2), where we assumed that the resonant eddies correspond to the eddies that have *exactly* the same turnover time as the response time of the particles. This is just an order of magnitude estimate, and a more correct expression would probably be

$$\tau_\ell = \gamma\tau_p, \tag{3.10}$$

where γ is of the order of unity. More work should, however, be devoted to understanding the coupling between the particles and the turbulent eddies. In particular, a more exact definition of the resonant eddies is needed. We nevertheless believe that β is a universal property of the HIP approximation and the Navier-Stokes equations that will have a constant value for all Re and St as long as the resonant eddies are within the inertial range.

In the right panel of figure 2, the average relative particle velocity, as found from the DNS simulations (symbols), is compared with the predicted values from Eq. (3.9) (solid lines). It is seen that the fit is rather good for most Reynolds and Stokes numbers. This supports the use of Eq. (3.9) for predicting the relative particle velocity.

3.2. *The cluster size*

The typical size of the clusters ℓ is assumed to be the size of the resonant eddies. From Eq. (3.3) this yields a cluster size of

$$l = L{\rm St}^{3/2}. \tag{3.11}$$

It can be seen from figure 3 that the particle number density distribution does indeed show more small scale variation for the smaller Stokes numbers. This has been quantified in figure 4 where

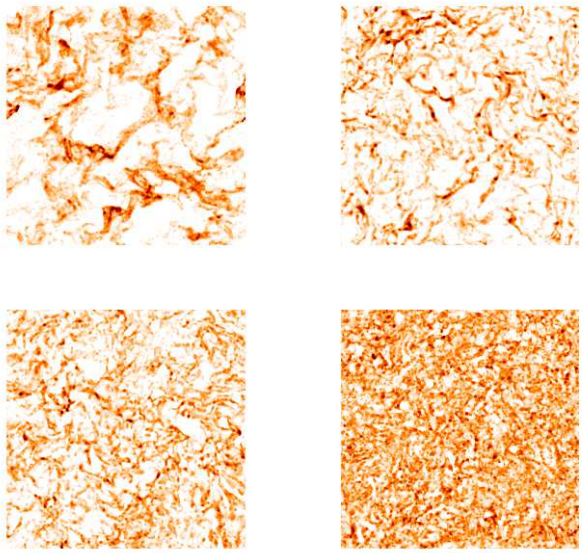

FIGURE 3. Particle number density for St = 1 (upper left), St = 0.3 (upper right), St = 0.1 (lower left) and St = 0.03 (lower right) (runs 3A, 3B, 3C and 3D in table 1).

the power spectrum of the particle number density is shown. Here we see that the spectrum peaks at large scales for St = 1 while the peak is located at much smaller scales for smaller Stokes numbers. The peak in the spectrum does not, however, follow Eq. (3.11) as accurately as expected. The reason for this is most likely that power spectra are not the right diagnostics to study the size of particle clusters, but it may also be partly because of: 1) poor statistics due to too few particles (the smaller clusters are not filled with particles), 2) the constant in the definition of the resonant eddies not being unity (see e.g. Eq. (3.10)), or 3) finite Reynolds number effects.

The power spectrum P can be integrated to yield a measure of the strength in the particle number density fluctuations, given by the root-mean-square (rms) particle number density;

$$n_{\text{rms}} = \int P dk. \tag{3.12}$$

It is found that the rms particle number density is decreasing with Stokes number. More specifically, n_{rms} is 1.6, 1.5, 1.2 and 0.8 for Stokes numbers of 1, 0.3, 0.1 and 0.03, respectively. This means that the high density regimes have higher particle number densities for larger Stokes numbers.

3.3. *Reactant consumption rate*

The normalized reactant consumption rate is shown in figure 5. The symbols correspond to the results from the DNS simulations, while the solid lines are given by Eq. (2.22). Here, the Stokes number is found by using the model for the relative velocity, as given by Eq. (3.9), in the expression for the Sherwood number (Eq. (1.3)). The value of the cluster decay rate, α_c, is the only free parameter and it is chosen by a best fit approach. The values of α_c are found in table 1.

The value of $\tilde{\alpha}$ for small Damköhler numbers equals the Sherwood number divided by two,

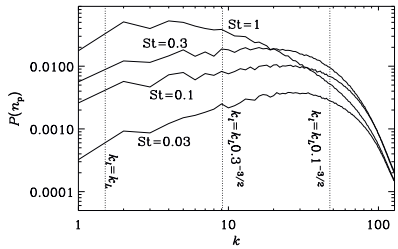

FIGURE 4. Power spectrum of particle number density for runs 3A, 3B, 3C and 3D in table 1.

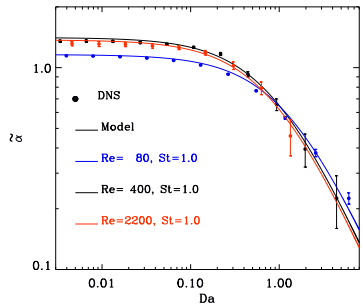

FIGURE 5. Normalized decay rate as a function of Damköhler number for Stokes number of unity (runs 1A-3A).

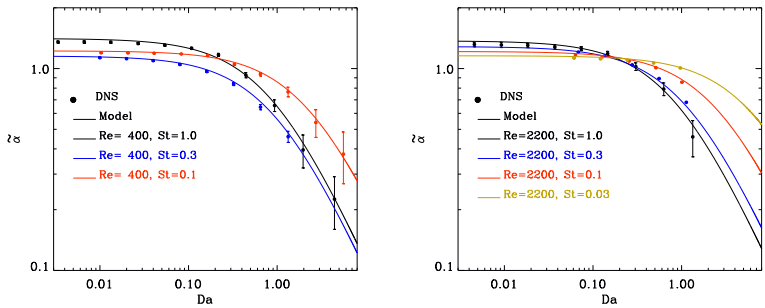

FIGURE 6. Normalized decay rate as a function of Damköhler number for different Stokes numbers. The left panel show the results for Re = 400 (runs 2A-C) while the right panel is for Re = 2200 (runs 3A-3D).

while the Damköhler number for which $\tilde{\alpha}$ starts to decrease is determined by the cluster decay rate α_c. Overall, the model seems to follow the results from the DNS simulations rather well.

From figure 5 it can be seen that for large Stokes numbers, the curves for the normalized decay rates of a given Stokes number overlap for different Reynolds numbers if the Reynolds number is high enough. This is because the resonant eddies are at scales larger than the dissipative subrange.

So increasing the Reynolds number, which may be considered a shift of the dissipative subrange to smaller scales, is not affecting the resonant eddies, and hence also the clustering is unaffected. If, however, the Reynolds or the Stokes number is small, such that the resonant eddies are in the dissipative subrange, a change in Reynolds number will have an effect on the normalized decay rate ($\tilde{\alpha}$).

Figure 6 shows that by decreasing the Stokes number, the normalized reactant decay rate stays unchanged up to larger Damköhler numbers. This means that the effect of particle clustering is weaker for smaller Stokes numbers. This is expected since the limit of very small clusters corresponds to individual particles, where $\tilde{\alpha}$ is independent of Da. From the simulations with small Damköhler numbers and Re = 2200, which are shown in the right panel of figure 6, it can be observed that the normalized decay rate is monotonically decreasing with Stokes number. The reason for this is that for these simulations the particle size is kept constant as the Stokes number is changed, such that the Sherwood number is decreased with decreasing Stokes number. This is, however, not the case for the simulations with Re = 400, where it is found that the normalized decay rate for small Damköhler numbers is lower for St = 0.3 than for St = 0.1. The reason for this is that a smaller particle radius was used for the simulations with St = 0.3. The effect of reducing the particle radius is that the particle Reynolds number, and hence also the Sherwood number, is decreased.

3.4. *The cluster decay rate*

If the chemical time scale is much shorter than the lifetime of the particle clusters, the interior of the clusters will quickly be void of reactants. This means that the reactant consumption rate is controlled by the flux of reactant to the surface of the clusters, where the reactant will be consumed at the exterior of the cluster. Based on this, it is clear that for large Da (small τ_c), the clusters behave as large solid particles, or super-particles. Following Kruger et al. (2016), the reactant decay rate is then given by the so called cluster decay rate;

$$\alpha_c = n_c \kappa_c A_c \tag{3.13}$$

when $n_c = A_1 l^{-3}$ is the number density of clusters (or super-particles), $\kappa_c = D_t \mathrm{Sh}/l$ is the reactant diffusion rate to the super-particles, $A_c = A_2 l^2$ is the surface area of the clusters, D_t is the turbulent diffusivity that carries the reactant from the surrounding fluid to the surface of the clusters and A_1 and A_2 are constants that depend on the dimensionality of the clusters. It is clear that turbulent eddies larger than ℓ, as given by Eq. (3.11), can not participate in the turbulent transport of reactants to the clusters, while eddies slightly smaller than ℓ will participate. A first approximation of the turbulent diffusivity to the surface of the clusters is therefore given by

$$D_t = u_\ell l = u_L L \mathrm{St}^2. \tag{3.14}$$

By combining the above, taking into account Eq. (3.11), it can be found that

$$\frac{\alpha_c \tau_L \mathrm{St}}{\mathrm{Sh}} = A_1 A_2, \tag{3.15}$$

where the right hand side should be constant for resonant eddies well inside the inertial range. From figure 7, it can be seen that the right hand side of the above equation is constant only for Stokes numbers smaller than ~ 0.3. Since the value of the right hand side starts to increase already for St = 0.3, this may once again indicate that γ from Eq. (3.10) is different from unity. The discrepancy may also be due to the fact that when it comes to the shape of the particle clusters, a large scale strain may stretch the particle clusters. For St $\sim$ 1, there are no vortices that are larger than the clusters, and hence the dimensionality of the clusters becomes different. This will inevitably yield different values of $A_1 A_2$. The value of the geometric coefficients can be

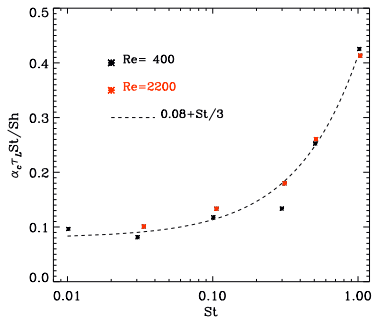

FIGURE 7. The product $\alpha_c \tau_L \mathrm{St}$ as a function of St for runs with resonant eddies in the inertial range.

fitted by

$$A_1 A_2 = 0.08 + \mathrm{St}/3, \tag{3.16}$$

but this is just an empirical fit and more work is required in order to understand the fundamentals behind the shape and size of the particle clusters.

4. Conclusion

In this work, the effect of turbulence on the mass (and heat) transfer between inertial particles and the embedding fluid is studied. The turbulence is shown to have two effects on the mass transfer. The first effect is active for all Damköhler numbers, and here the turbulence increases the mass transfer rate due to the relative velocity between the particles in the fluid. A corresponding model for the relative velocity between the fluid and the particles is given by Eq. (3.9) which uses basic variables of the flow. With this, adding effects of relative velocity into RANS based simulations is possible.

The second effect with which turbulence influences the mass transfer rate is through the clustering of particles. It is shown that the size of the particle clusters increases with the particle Stokes number, and that the clustering decreases the overall mass transfer rate between the particles and the fluid. This is a confirmation of the findings of Kruger et al. (2016). In addition, a model is developed that takes this effect into account and incorporates it into a modified Sherwood number. This model is shown to give reasonable results for Stokes numbers (based on the turbulent integral scale) less than ~ 0.3, while an empirical fit is employed to account for Stokes numbers up to unity. More work is still required in order to fully understand the size and dimensionality of the the particle clusters. As of now, a unique way of characterizing particle clusters does not exist, and very little work has actually been put into the study of large-scale clustering of particles.

Acknowledgements

The research leading to these results has received funding from the Polish-Norwegian Research Program operated by the National Centre for Research and Development under the Norwegian Financial Mechanism 2009-2014 in the frame of Project Contract No Pol-Nor/232738/101/2014. This work was supported by the grant "Bottlenecks for particle growth in turbulent aerosols from the Knut and Alice Wallenberg Foundation, Dnr. KAW 2014.0048 and by grant from Swedish

Research Council (Dnr. 638-2013-9243). NELH and DM also acknowledge the Research Council of Norway under the FRINATEK grant 231444.

REFERENCES

W. P. Jones and B. E. Launder, Int. J. Heat Mass Transfer **15**, 301 (1972).
S. B. Pope, *Turbulent flows*. Cambridge University Press (2003).
L. Schiller and A. Naumann, Ver. Deut. Ing **77**, 318 (1933).
C. T. Crowe, *Multiphase Flows Droplets*. CRC Press (2012).
B. F. Magnussen and B. H. Hjertager, 16'th Symposium (International) on Combustion, pp. 719-729. Pittsburgh: The Combustion Institute (1976).
I. S. Ertesvåg and B. F. Magnussen , Combust. Sci. Technol. **159**, 213 (2000).
C. Dopazo, (ed. P. A. Libby and F. A. Williams), pp. 375-474. London: Academic Press. (1994).
W. E. Ranz and W. R. Marshall, Chem Engr. Prog. **48**, pps. 141 and 173 (1952).
J. Kruger, N. E. L. Haugen, T. Lovas and D. Mitra *Proc. Comb. Symp.*, dx.doi.org/10.1016/j.proci.2016.06.187
A. Silaen and T. Wang, Int. J. Heat Mass Transfer **53**, 2074-2091 (2010).
M. Vascellari, S. Schulze, P. Nikrityuk, D. Safronov and C. Hasse, Flow turbulence and combustion **92**, 319-345 (2014).
M. Vascellari, D. G. Roberts, S. S. Hla, D. J. Harris and C. Hasse, Fuel **152**, 58-73 (2015).
A. Klimanek, W. Adamczyk, A. Katelbach-Wozniak, G. Wecel and A. Szlek, Fuel **152**, 131-137 (2015).
L. Chen, S. Z. Yong and A. F. Ghoniem, Progress in energy and combustion science **38**, 156-214 (2012).
C. Chen, M. Horio and T. Kojima, Chemical Engineering Science **55**, 3875-3883 (2000).
J. Gao, C. Xu. S. Lin and G. Yang, AIChE Journal **45**, 1095-1113 (2004).
Y. Zhang, X.-L. Wei, L.-X. Zhou and H.-Z. Sheng, Fuel **84**, 1798-1804 (2005).
K. Luo, H. Wang, J. Fan and F. Yi, Energy and Fuels **26**, 6128-6136 (2012).
T. Brosh and N. Chakraborty, Energy and Fuels **28**, 6077-0688 (2014).
T. Brosh, D. Patel, D. Wacks and N. Chakraborty, Fuel **145**, 50-62 (2015).
T. Hara, M. Muto, T. Kitano, R. Kurose and S. Komori, Combustion and Flame **162**, 4391-4407 (2015).
N. G. Deen and J. A. M. Kuipers, Chemical Engineering Science **116**, 645-656 (2014).
A. Johansen, J. S. Oishi, M.M.Mac Low, H. Klahr, T. Henning, and A. Youdin, Nature **448**, 1022 (2007).
N. E. L. Haugen and S. Kragset, J. Fluid Mech. **661**, 239 (2010).
N. E. L. Haugen, N. Kleeoring, I. Rogachevskii and A. Brandenburg, Phys. Fluids **24**, 075106 (2012).
The Pencil-Code, http://pencil-code.nordita.org/
N. E. L. Haugen and A. Brandenburg, Phys. Fluids **18**, 075106 (2006).
E. Calzavarini, M. Kerscher, D. Lohse and F. Toschi, J. Fluid Mech. **607**, 13-24 (2008).
M. M. Baum and P. J. Street, Combustion Science and Technology **3**, 231-243 (1971).
J. Bec, L. Biferale, M. Cencini, A. Lanotte, S. Musacchio and F. Toschi, Physical Review Letter **98**, 084502 (2007).
K. D. Squires and J. K. Eaton, Journal of Fluid Mechanics **226**, 1-35 (1991).
A. M. Wood, W. Hwang and J. K. Eaton, International Journal of Multiphase Flow **31**, 1220-1230 (2005).
J. K. Eaton and J. R. Fessler, International Journal of Multiphase Flow **20**, 169-209 (1994).
F. Toschi and E. Bodenschatz, Annual Review of Fluid Mechanics **41**, 375-404 (2009).

5.5 Paper 5

Correlation effects between turbulence and the conversion rate of pulverized char particles

Jonas Krüger, Nils Erland L. Haugen and Terese Løvås
Submitted to Combustion & Flame

Correlation effects between turbulence and the conversion rate of pulverized char particles

Jonas Krüger[a,*], Nils Erland L. Haugen[a,b], Terese Løvås[a]

[a]*Department of Energy and Process Engineering, Norwegian University of Science and Technology Kolbjørn Hejes vei 1B, NO-7491 Trondheim, Norway*
[b]*SINTEF Energy Research, N-7465 Trondheim, Norway*

Abstract

The effect of turbulence on heterogeneous reactions on the surface of char particles embedded in a turbulent oxidizer, consisting of oxygen and carbon-dioxide, is in this work studied numerically. It is shown that for small Damköhler numbers (**Da**), the char conversion rates are somewhat *increased* by the turbulence. This is found to be due to the increased mass transfer rate to the char particle surface that is caused by the turbulence-induced relative velocity between the char and the oxidizer. For large Damköhler numbers, however, the char conversion rate is strongly *reduced* due to particle clustering. This reduction is explained by the fact that when particles are clustered in densely populated particle clusters, the transfer of oxygen to the particles in the centre of the clusters is reduced since the oxygen is consumed by the particles closer to the external surface of the cluster. At the same time, high concentrations of oxygen exist in the voids between the particle clusters. This oxygen can not take part in the conversion of the char until it is transported to the char surface. The effects of turbulence on the heterogeneous reaction rates are furthermore modelled based on Direct Numerical Simulation

*Corresponding Author: jonas.kruger@ntnu.no

(DNS) data for a simplified reacting gas particle system.

Keywords: Reacting multiphase flow; Particle clustering; Heterogeneous combustion; Direct Numerical Simulation; Char; Turbulence;

1. Introduction

Numerical simulations are an important tool in predicting the performance, and planning the operation, of industrial applications involving heterogeneous reactions, such as pulverized coal combustion (PCC) or biomass gasification. To increase efficiency and decrease the environmental impact of new systems and optimize existing ones, more insight into the details of combustion processes is essential. Since combustion processes are a complex interaction of physical and chemical effects such as mass, momentum, heat and species transfer over a wide range of scales, also in conjunction with chemical reactions, even a simplified case description is complex. This restricts simulations of industrial scale combustion systems to be very coarse and use empirical models. This is especially true if a lot of cases have to be simulated for a parametric study.

A common approach used in industry and research is the Reynolds-Averaged Navier Stokes (RANS) model [1]. In addition, the first Large-eddy simulations (LES) are now employed for pilot scale systems [2]. These modelling approaches require subgrid models that account for flow and chemistry effects on scales that are smaller than what is resolved by the simulation. The subgrid models used in RANS and LES are developed by studying lab scale systems or numerical experiments using Direct Numerical Simulation (DNS), where all relevant turbulent scales are resolved. Although they are computationally expensive [3], DNS pro-

vide a way to non-intrusively study turbulent combustion systems and yield flow statistics that are difficult or impossible to obtain in real experiments [4]. This accurate description of the flow in DNS makes it especially suitable to study turbulent flows in detail. The insights gained can then be utilized to develop models and correlations that can be used in simulations of industrial systems.

It is known that turbulence affects combustion systems on different scales, from the recirculation zone behind a bluff body burner to small vortices in the flow far downstream. Turbulence is also essential for mixing and transport of physical properties, such as energy and species composition, which in turn have an influence on the reaction rates. For the case of homogeneous combustion, the interaction between turbulence and combustion has been studied extensively, and consequently a large variety of models have been developed. The review paper by Veynante and Vervisch [5] and the book by Poinsot and Veynante [6] provide an excellent overview over the progress of homogeneous combustion research and the models for turbulence chemistry interaction that have been developed. For premixed flames e.g., models that are based on the interaction of scales [7], probabilities to find either burned or unburned gases [8, 9], or geometrical descriptions of the flame [10, 11] can be used. In the case of non premixed flames with infinitely fast chemistry, one can use a presumed Probability Density Function (PDF) [12] or the Eddy Dissipation Concept (EDM), where the reactions are limited by either a deficiency of fuel, oxidizer or energy [13], or the Conditional Moment Closure (CMC), where all variable parameters are conditionally averaged on flow parameters such as the mixture fraction [14, 15]. If the chemistry is not assumed to be infinitely fast, the reaction rates may be obtained from flamelet libraries based on presumed PDFs of laminar flames or the shape of the flame [16]. Each of these

models have individual strengths and shortcomings making them applicable to different combustion conditions.

Combustion of solid matter adds more complexity to the phenomena of turbulence chemistry interaction due to the multi phase nature of the problem. Depending on the composition of the fuel, each particle has to undergo drying, devolatilization/pyrolysis and finally heterogeneous combustion, all of which have to be accounted for in a complete description of the combustion process [17]. The interested reader is referred to the article of Eaton et al. [18] for a review on models used in pulverized coal combustion. However, to the authors' knowledge, there is no turbulence-chemistry model connecting the effect of turbulence to the process of conversion of a dried, devolatilized char particle, which is the objective of the present work.

A reacting particle and the surrounding turbulent flow are interacting on different scales, and these effects can increase or decrease the reaction rate depending on turbulence intensity. At the scale of a particle, the flow around the particle is responsible for transporting reaction products away from the particle surface, and bringing reactants to it. Additionally, turbulence increases heat transfer from and to the particle, leading to a change in the speed of reaction [19]. On larger scales, turbulence leads to a preferential concentration of particles [20, 21], where particles form dense particle clusters, separated by voids where nearly no particles are present. This can separate the solid fuel from the gaseous oxidizer. Describing the shape and size of these particle clusters and voids is a major research field in itself [22].

Annamalai and Ramalingam [23] performed a theoretical study of the com-

bustion behaviour of clusters of coal particles in a quiescent flow and identify three distinct regimes, which are defined by low, medium or high particle concentrations inside the clusters. The Individual Particle Combustion (IPC) regime, is characterised by that the distances between particles are so high that their interaction can be neglected. For medium particle concentrations, the particles on the outside of the clusters consume the oxidizer fast enough so that particles on the inside of the cluster react under fuel-richer conditions, which is called Group Combustion (GC). Finally, for high particle concentrations, the outermost shell of particles consumes all the oxidizer which is transported to it, effectively preventing oxidizing species transport to the internal particles. This combustion regime is called Sheath Combustion (SC), as only the sheath of the particle cluster is reacting. These regimes were found to have different combustion rates [23]. It is reported that in the IPC, a decrease in particle size (by particle break up, leading to a increase in particle number) results in an increase in the surface specific burning rate. In the SC regime, a decrease in particle size may result in a decrease of the surface specific burning rate. A similar finding is reported by Reveillon and Demoulin [24], who examined the evaporation behaviour of droplets in turbulent flows and found that the evaporation rate inside droplet clusters is slower than on the outside. This is due to the fast saturation of the fluid inside the droplet clusters and the slow mixing of saturated and unsaturated fluid.

Due to the increase of available computing power, DNS of pulverized coal jets under highly turbulent conditions have recently been published, providing insights into this complex phenomenon. Luo et al. performed a DNS of a pulverized coal jet flame [25] for a Reynolds number of around 30000 and compare their results qualitatively with experiments. They identify GC regimes at the jet nozzle and IPC

regimes further downstream in the jet. A lab-scale pulverized coal jet flame was studied by Hara et al. [26], who propose a simple global reaction scheme that takes into account the effects of devolatilization products on the homogeneous reactions. A good agreement on the particle motion between simulation and experiments is reported. Moreover, they find different combustion regimes in the inner and outer flame layer. Brosh and Chackraborty investigated the effect of equivalence ratios and velocity fluctuations on pulverized coal combustion [27] and ignition [28] and found that the premixed combustion regime (which is more similar to IPC and GC than to SC) is more prominent for higher turbulent velocity fluctuations and vice versa. Moreover, an increase in velocity fluctuations is beneficial for mixing, but too high velocity fluctuations lead to flame extinction by increasing the heat transfer from the flame kernel. However, the published studies focus either on early stages of the combustion, where devolatilized fuel is the main driver of combustion [27], or on flows with non-isotropic turbulence [26]. While all studies account for char conversion, it is not explicitly studied.

The present work is part of an effort to provide a subgrid model to account for the effect of turbulence on heterogeneous reactions (such as char oxidation). DNS is used to study clustered char particles in a turbulent reacting flow and analyse the effect of changing Damköhler numbers (from now on written as **Da**) on the char oxidation rates. It is an extension of earlier work that studied this effect in a simplified setup [29, 30], where the isothermal consumption of a passive scalar by particles in a turbulent flow was studied by DNS. This work is now extended to a DNS with heterogeneous reactions between reactive chemical species in order to study the interaction between the kinetics of heterogeneous reactions and turbulent clustering.

Although complex char oxidation reaction mechanisms exist [31, 32], the wide range of time scales of the individual reactions make a deduction of basic flow properties and timescales used in the analysis complicated. Moreover, calculating and storing many species and their reaction rates for both flow field and a large number of particles is prohibitively expensive, hence a simple mechanism is used in this work, although the mathematical framework is developed for a generic kinetic case.

The combustion process investigated in this work is represented by oxy-fuel combustion, which has been proposed as one measure to implement carbon capture technologies, and hence, decrease the environmental impact of fossil fuelled energy generation, as summarized in the review paper of Chen et al. [33]. The main difference between oxy-fuel and conventional combustion is that instead of air, pure oxygen together with recirculated flue gases, mainly CO_2, is used as oxidizing agent. Thus it represents a simple case to study when only oxygen is assumed to be the oxidizing species.

The paper first gives an overview of the equations that are used to describe the fluid, the particles and their interaction in § 2, followed by an introduction of all dimensionless numbers in § 3. Thereafter, a model is proposed to describe the effect of turbulent clustering on the heterogeneous reaction rates, followed by the boundary and initial conditions of the DNS cases in § 4. In § 5, the data obtained is shown and compared with the proposed model, followed by a short discussion of the results and future work in Section § 6.

2. Numerical Modelling

2.1. Fluid Equations

For the DNS simulations shown in this work, "The Pencil-Code" [34] is used, which is a an open source CFD code. It solves the fluid equations using a sixth-order finite difference scheme for spatial discretization and a compact third-order Runge-Kutta scheme [35] for temporal discretization. Gravity is neglected for both particle and fluid phase for simplicity and all domain boundaries are periodic. The implementation of the homogeneous chemistry has previously been described in detail by Babkovskaia et al. [36]. The continuity equation is solved as

$$\frac{\mathrm{D}\rho}{\mathrm{D}t} = -\rho\boldsymbol{\nabla}\cdot\boldsymbol{u} + S_\rho, \tag{1}$$

where $\mathrm{D}/\mathrm{D}t = \partial/\partial t + \boldsymbol{u}\cdot\boldsymbol{\nabla}$ is the advective derivative, ρ is the density, $\boldsymbol{u}$ is the velocity and

$$S_\rho = \frac{-1}{V_{\mathrm{cell}}}\sum_{i}^{N_{p,cell}}\frac{dm_{p,i}}{dt} \tag{2}$$

is the mass source term due to mass transfer from the particles to the fluid. In the above equation, $m_{p,i}$ represents the mass of particle number i, V_{cell} is the volume of the grid cell and the summation is over all particles i in the grid cell. The number of particles in the cell is given by $N_{p,cell}$. The momentum equation is written in the form

$$\rho\frac{\mathrm{D}\boldsymbol{u}}{\mathrm{D}t} = -\boldsymbol{\nabla}p + \nabla\cdot\tau + \boldsymbol{f} + S_{m,p}, \tag{3}$$

where p is pressure and $\boldsymbol{f}$ is a volume force. The volume force has random directions and wavelengths that are short compared to the length of the domain. The forcing mechanism is described in the work of Brandenburg et al. [37] and yields homogeneous isotropic turbulence. The viscous stress is given by:

$$\tau = 2\rho\nu\boldsymbol{S}, \tag{4}$$

where $\boldsymbol{S} = (1/2)(\partial u_i/\partial x_j + \partial u_j/\partial x_i) - (1/3)\delta_{ij}\nabla \cdot \boldsymbol{u}$ is the trace-less rate of strain tensor. Since the resolution in all cases is sufficient to resolve the smallest scales of the turbulence, no modelling of turbulence is required. The term $S_{m,p} = (1/V_{\text{cell}}) \sum_i \dot{m}_{p,i}(\boldsymbol{u} - \boldsymbol{v}_{p,i})$ in Eq. (3) accounts for the momentum that is transferred to the fluid by the mass that is released from the particle with velocity $\boldsymbol{v}_{p,i}$. The equation for the mass fractions of each species is given by

$$\rho\frac{\mathrm{D}Y_k}{\mathrm{D}t} = -\nabla \cdot \boldsymbol{J}_k + \dot{\omega}_k + S_{y,k}, \tag{5}$$

where Y_k is the mass fraction of species k, $\boldsymbol{J}_k$ is the diffusive flux and $\dot{\omega}_k$ is the chemical source term of species k due to homogeneous reactions, described in detail in the work of Babkovskaia et al. [36], and

$$S_{y,k} = \frac{1}{V_{\text{cell}}} \sum_{i}^{N_{p,cell}} \left(\dot{W}_{k,i} + Y_k \frac{dm_{p,i}}{dt} \right) \tag{6}$$

is the source term due to gas phase species being involved in the heterogeneous reactions. Here, $\dot{W}_{k,i}$ is the source of gas phase species k due to heterogeneous

reactions on particle i (see Eq. (26)). The diffusive flux of species k is given by

$$\boldsymbol{J}_k = \rho Y_k \boldsymbol{V}_k \tag{7}$$

when $\boldsymbol{V}_k$ is the diffusive velocity of species k. Finally, the energy equation is

$$\begin{aligned} c_v \frac{\mathrm{D} \ln T_g}{\mathrm{D}t} = \sum_k^{N_{species}} \left(- \nabla \cdot \boldsymbol{J} + \dot{\omega}_k \right) \left(\frac{R}{m_k} - \frac{h_{s,k}}{T_g} \right) - \frac{R}{m_k} \nabla \cdot \boldsymbol{u} \\ + \frac{2\nu \boldsymbol{S}^2}{T_g} - \frac{\nabla \cdot \mathbf{q}}{\rho T_g} + S_{T,conv} + S_{enth}, \end{aligned} \tag{8}$$

where T_g is the gas temperature, c_v is the heat capacity at constant volume, R is the universal gas constant, $h_{s,k}$ is the sensible enthalpy of species k, m_k is the molar mass of species k,

$$\boldsymbol{q} = \sum_k^{N_{species}} h_k \boldsymbol{J}_k - k_g \nabla T_g \tag{9}$$

is the heat flux and $h_k = h_{s,k} + \Delta h^0_{f,k}$ becomes the enthalpy of species k when $\Delta h^0_{f,k}$ is the heat of formation of species k. The thermal conductivity is given by k_g. In the above equation, the sum of the conductive and convective heat transfer from the particles to the gas is given by

$$S_{T,conv} = \frac{1}{\rho T_g} \frac{1}{V_{\text{cell}}} \sum_i^{N_{p,cell}} Q_{c,i}, \tag{10}$$

when

$$Q_{c,i} = H_i A_{p,i} (T_{p,i} - T_g), \tag{11}$$

and the temperature of particle i is $T_{p,i}$. The mass that is transferred to the fluid carries enthalpy with it, which is accounted for by the term

$$S_{enth} = \frac{1}{\rho T_{gas}} \frac{1}{V_{\text{cell}}} \sum_{i}^{N_{p,cell}} \dot{W}_{k,i} h_{k,i}(T_{phase}). \tag{12}$$

The temperature T_{phase}, at which the species enthalpy is evaluated is taken from the phase where the species originated. When gas phase species are consumed, the enthalpy is evaluated at the gas phase temperature, if the species in question is produced by the particle, its enthalpy is evaluated at the particle temperature. The heat transfer coefficient H_i, taken from [38], can be expressed as

$$H_i = \frac{\text{Nu}_i k_g}{2 r_{p,i}} \frac{B_i}{\exp(B_i) - 1} \tag{13}$$

when Nu_i is the Nusselt number obtained from the Ranz-Marshall [19] correlation:

$$\text{Nu}_i = 2 + 0.6 \text{Re}_{p,i}^{0.5} \text{Pr}^{0.33} \tag{14}$$

with Pr being the Prandtl number of the fluid, calculated as

$$\text{Pr} = \frac{\mu c_p}{k_g}, \tag{15}$$

where μ is the dynamic viscosity of the fluid and c_p the heat capacity at constant pressure. The particle Reynolds number is given by

$$\text{Re}_{p,i} = \frac{d_{p,i} |\boldsymbol{v}_{p,i} - \boldsymbol{u}|}{\nu}, \tag{16}$$

when $d_{p,i} = 2r_{p,i}$ is the particle diameter, $r_{p,i}$ is the particle radius and $A_{p,i} = \pi r_{p,i}^2$ is the cross sectional area of the particle. The Stefan flow constant in Eq. (13) is given by

$$B_i = \frac{\dot{m}_{p,i} c_v}{2\pi r_{p,i} \mathrm{Nu}_i k_g}. \tag{17}$$

In this work, we use the ideal gas equation of state, such that the pressure is found as

$$p = \frac{\rho R T}{m}. \tag{18}$$

Detailed expressions for viscosity, species diffusion, thermal conduction, enthalpy and heat capacity are found in [36].

To increase the numerical stability of the simulations, the particle related source terms in the fluid equations S_ρ, $S_{Y,k}$, $S_{m,p}$, and S_{enth} are stored in temporary scalar or vector fields and diffused by Laplacian diffusion before being added to the fluid cells. A general flow variable θ_0 is stored in a scalar field before the diffusion steps. The value of the variable is then, after the n'th diffusion step:

$$\theta_{n+1} = \theta_n + \frac{D_{num} \Delta t}{N_{step}} \nabla^2 \theta_n, \tag{19}$$

when D_{num} is a numerical diffusion coefficient, Δt is the simulation timestep and N_{step} is the total number of diffusion steps per timestep. A compact 6-th order scheme is used to obtain the second derivative. The diffusion coefficient D_{num} is chosen as small as possible while ensuring stable calculations with three diffusion steps for every timestep. Of the total mass, energy or species transfer from a parti-

cle to the fluid, 80% is added to nodes directly neighbouring the node the particle is closest to. This approach greatly stabilizes the simulations without significantly changing the dynamics of the flow. An alternative to the approach described above is to use a spatial filter to distribute the effect of a particle onto several fluid grid points. The spatial filter would typically be a weighted distribution over the fluid grid points in the neighbourhood of the particle. For more numerical stability, a spatial filter with a larger radius of influence will be needed, which means that the effect of the particle will be distributed over more grid points. The effect of the radius of influence in such methods is studied by Sundaram and Collins [39]. During the development of the method used in the current work, comparisons with established interpolation methods for particle-fluid transfers, like the particle-in-cell-method (PIC) of Squires and Eaton [40] and the projection onto neighbouring nodes (PNN) method as used by Elghobashi and Truesdell [41], have been performed. The method used in this work (Eq. (19)) yielded results that lie between the PIC and the PNN.

2.2. The particle equations

The particle model of the Pencil-Code has been extended to account for reactive particles, which exchange momentum, mass, species and energy with the fluid. A detailed description of the particle reaction model can be found in Haugen et al. [38, 42]. The only momentum transfer from the particles to the fluid is via the mass they transfer to the fluid. The back reaction due to the particle drag force is not considered in this work, since its focus lies not on turbulence statistics. The particles are regarded as point particles, displacing no fluid, which is valid for particles that are much smaller than the grid cells. Furthermore, particle-particle interactions are not considered due to the dilute nature of the flow. Particle track-

ing is achieved using a Lagrangian formalism where the evolution equation for the particle velocity is given as

$$\frac{\mathrm{d}\boldsymbol{v}_p}{\mathrm{d}t} = \frac{\boldsymbol{F}_p}{m_p}, \tag{20}$$

and for the position as

$$\frac{\mathrm{d}\boldsymbol{x}}{\mathrm{d}t} = \boldsymbol{v}_p, \tag{21}$$

where m_p, $\boldsymbol{v}_p$ and $\boldsymbol{x}$ are the mass, velocity and position of the particle's centre of mass, respectively. Furthermore, the force $\boldsymbol{F}_p$ is the sum of all forces acting on the particle. Since gravity is neglected, and since a high density ratio between the particles and the fluid is assumed, the only force on the particles that has to be considered is the drag force. The Stokes drag, with extension to low and medium particle Reynolds numbers, is used in the present work. This means that the total force acting on the particles is given by

$$\boldsymbol{F}_p = \frac{1}{2}\rho C_D A_p |\boldsymbol{u} - \boldsymbol{v}_p|(\boldsymbol{u} - \boldsymbol{v}_p) = \frac{m_p}{\tau_p}(\boldsymbol{u} - \boldsymbol{v}_p), \tag{22}$$

when

$$\tau_p = \frac{2m_p}{\rho C_D \pi r_p^2 |\boldsymbol{u} - \boldsymbol{v}_p|} = \frac{8\rho_p r_p}{3\rho C_D |\boldsymbol{u} - \boldsymbol{v}_p|} = \frac{S\, d_p^2}{18\nu(1 + f_c)} \tag{23}$$

is the particle response time (Stokes time). In this equation, $S = \rho_p/\rho$ is the density ratio between a particle and the fluid. The extended Stokes drag coefficient

is

$$C_D = \frac{24}{\mathrm{Re}_p}(1 + f_c), \tag{24}$$

where $f_c = 0.15\mathrm{Re}_p^{0.687}$ is due to the Schiller-Naumann correlation, which is valid for particle Reynolds numbers up to 800 [43]. The particles in our simulations have a mean particle Reynolds number of 0.1. The mass loss rate of a single particle is calculated as:

$$\frac{dm_p}{dt} = -\sum_{k}^{N_{species}} \dot{W}_k, \tag{25}$$

while the net species mass production rate is given by

$$\dot{W}_k = A_p \widehat{RR}_k M_k. \tag{26}$$

The surface area of the particle is denoted A_p, the molar mass of species k is M_k and

$$\widehat{RR}_k = \sum_{j}^{N_{reactions,het}} (\nu''_{j,k} - \nu'_{j,k})\widehat{R}_j \tag{27}$$

is the surface specific molar production rate of species k. The stoichiometric coefficients $\nu'_{j,k}$ and $\nu''_{j,k}$ are for the reactant and product side of reaction j, respectively. The rate of reaction j is given by:

$$\widehat{R}_j = k_{kin,j}\left(\prod_{l}^{N_{species}} \left(X_{l,s}C_g\right)^{\nu'_{j,l}} \right). \tag{28}$$

Here, $X_{l,s}$ is the mole-fraction of species l at the particle surface, C_g is the local gas concentration, which is evaluated at the particle film temperature $T_{film} = T_p + (T_g - T_p)/3$ and found from the ideal gas law;

$$C_g = \frac{N_m}{V} = \frac{p}{RT_{film}}. \tag{29}$$

In this equation, N_m represents the number of moles in the volume V. The kinetic rate of reaction j is given by the Arrhenius expression

$$k_{kin,j} = B_{n,j} T^{\alpha_{n,j}} \exp(-E_{an,j}/RT_p), \tag{30}$$

where B_n is the pre-exponential factor, α_n is the temperature exponent, and E_{an} the activation energy, which are all empirical coefficients that are given by the kinetic mechanism.

For a single irreversible global heterogeneous reaction with only one homogeneous reactant species r, an algebraic solution for the surface mole fraction $X_{r,s}$ of the reactant can be found by applying the Baum and Street model [44] and assuming equilibrium between the transport and consumption of the reactant r:

$$\underbrace{X_{r,s}\dot{n}_{\text{total}}}_{Stefan\ Flow} - \underbrace{C_g k_{diff}(X_{r,\infty} - X_{r,s})}_{Diffusion} = \underbrace{C_g k_{kin} X_{r,s}}_{Production/Consumption}. \tag{31}$$

If the heterogeneous reaction is unimolar, i.e. $\dot{n}_{total} = 0$, Eq. (31) gives a very simple expression for the mole fraction of reactant r at the particle surface;

$$X_{r,s} = \frac{X_{r,\infty} k_{diff}}{k_{kin} + k_{diff}}, \tag{32}$$

when k_{diff} is the mass transfer coefficient. For multiple reactant species, a multivariate set of Eq. (32) can be solved by a Newton-Raphson method. As long as the particle is much smaller than the fluid grid cell, the expression in Eq. (32) makes it possible to use the mean reactant mole fraction in the grid cell, $X_{r,\infty}$, instead of the reactant mole fraction at the particle surface, $X_{r,s}$. For a single reaction with one reactant species, Eq. (28) then reduces to

$$\widehat{R} = k_{eff} X_{r,\infty} C_g, \tag{33}$$

when the mean effective reaction coefficient,

$$k_{eff} = \frac{k_{kin} k_{diff}}{k_{kin} + k_{diff}}, \tag{34}$$

is introduced to account for kinetic reaction rate as well as diffusive transport of reactant to the particle. The term k_{diff} is the mass transfer rate, which is defined by

$$k_{diff} = \frac{D\mathrm{Sh}}{2r_p}, \tag{35}$$

where D is the diffusivity in the bulk gas and

$$\mathrm{Sh} = 2 + 0.69\mathrm{Re}_p^{0.5}\mathrm{Sc}^{0.33} \tag{36}$$

is the particle Sherwood number, which is obtained using the Ranz-Marshall correlation [19] for flows with low and intermediate Reynolds numbers. Here, Re_p is the particle Reynolds number and Sc the Schmidt number. It is interesting to note that for a RANS simulation, the relative velocity between the particles and the

fluid is not available since the turbulence velocity is not resolved. In many RANS modelling tools, it is therefore customary to include some kind of particle dispersion model, where the particles are displaced in random directions and distances based on the local turbulence parameters in order to make the particles diffuse through the fluid. As a by-product of the particle dispersion that is obtained with these models, there will be a relative velocity between the particles and the fluid, but, since no account is made for the correlation with the instantaneous turbulent structures, this velocity does not have anything to do with the reality. It is therefore often better to simply neglect the effect of the relative particle-fluid velocity by setting the particle Reynolds number in Eq. (36) to zero, such that the Sherwood number becomes 2. Hence, for a quiescent fluid, or for a RANS simulation, the Sherwood number is 2 and the mass transfer coefficient then reduces to

$$k_{diff,q} = D/r_p. \tag{37}$$

The particle temperature evolution is given by:

$$\frac{dT_p}{dt} = \frac{1}{m_p c_{p,p}}(Q_{reac} - Q_c + Q_{rad}), \tag{38}$$

where Q_{reac} is the heat due to the surface reactions, Q_c the conductive heat loss to the fluid and $Q_{rad} = 4\epsilon\sigma\pi r_p^2(T_s^4 - T_p^4)$ is the radiative heating of the particle. Here, ϵ is the emissivity, σ the Stefan-Boltzmann constant and T_s is the temperature of the surroundings. If $T_p > T_s$, this corresponds to a situation where the particles are radiatively cooled, acting as heat sinks in the system. The particle heat capacity is denoted by $c_{p,p}$. The particle is assumed to be thermally thin, resulting in a uniform temperature distribution throughout the particle.

The reactive heating rate is given by:

$$Q_{reac} = A_{p,i} \sum_{j}^{n_{reactions}} \widehat{R}_j h_j, \tag{39}$$

when the heating due to reaction j is composed of the surface specific reaction rate $\widehat{R}_j$ and the heat of reaction h_j. The specific enthalpies are calculated at the particle temperature for all products and for all solid reactants, and at the gas temperature for gaseous reactants. The reactive heating only heats up the particle, as the heat loss to the fluid is already accounted for by evaluating the species enthalpy that is transferred to the fluid at the particles temperature in the term S_{enth} in Eq. (12).

3. Dimensionless numbers

In this work, four dimensionless numbers are of special interest and therefore explained in detail: The Damköhler number Da, the Sherwood number Sh, the particle Stokes number St and the Sherwood correction factor $\tilde{\alpha}$. The Damköhler number is the ratio between the turbulent time scale τ_L and the chemical time scale τ_{hom}:

$$\mathrm{Da} = \frac{\tau_L}{\tau_{hom}}, \tag{40}$$

where τ_{hom} is the inverse of the ideal homogeneous reaction rate. If we assume a reactive object, which is typically a particle or a dense cluster of particles, the ideal homogeneous reaction rate then depends on the mean reactive surface area of the object $\overline{A}'$, the mean reactive density $\overline{n}'$ and its effective reaction rate $\overline{k}'_{eff}$.

Accordingly, τ_{hom} can be expressed as

$$\tau_{hom} = \frac{1}{\alpha_{hom}} = \frac{1}{\overline{A}'\overline{n}'\overline{k}'_{eff}}, \tag{41}$$

such that the Damköhler number becomes:

$$\mathrm{Da} = \alpha_{hom}\tau_L = \overline{A}'\overline{n}'\overline{k}'_{eff}\tau_L. \tag{42}$$

The turbulent time scale considered in this work is the time scale τ_L of the integral scale, $l = L/2\pi k_f$, which is given by

$$\tau_L = \frac{L}{2\pi k_f u_{\mathrm{RMS}}}, \tag{43}$$

where L is the domain size, k_f is the wave number of the external forcing and the root mean square velocity is u_{RMS}.

The particle Stokes number is given by the ratio between the particle response time and the turbulent time scale:

$$\mathrm{St} = \frac{\tau_p}{\tau_L}. \tag{44}$$

To achieve clustering at the large scales of the flow, the density and radius of the particles are chosen so that for the simulations in this work a Stokes number of approximately 1 is achieved.

3.1. The ideal homogeneous reaction rate and the Damköhler number

For low **Da**, the fluid composition and temperature is relatively homogeneously distributed throughout the domain. This means that the fluid surroundings of a

given particle is not directly influenced by the particles in its immediate neighbourhood, but rather by the accumulated effect of all particles in the domain. Thus, the reaction rate, and hence also the Damköhler number, scale proportionally to the mean surface area of the particles $\overline{A}' = \overline{A}_p$, the mean particle number density in the domain $\overline{n}' = \overline{n}_p$ and mean effective particle reaction rate $\overline{k}'_{eff} = \overline{k}_{eff,p}$, which means that the Damköhler is given by

$$\mathrm{Da} = \overline{A}_p \overline{n}_p \overline{k}_{eff,p} \tau_L = \alpha_{hom,q} \tau_L, \tag{45}$$

when the ideal homogeneous reaction rate is

$$\alpha_{hom,q} = \overline{A}_p \overline{n}_p \overline{k}_{eff,p}, \tag{46}$$

for a quiescent fluid (Sh=2) and a mean effective particle reaction rate $\overline{k}_{eff,p}$ that is equal to the mass transfer rate k_{diff}, is established as a base value to compare against. This case, when $k_{diff} = k_{eff,p}$, corresponds to the situation when $k_{diff} \ll k_{kin}$, i.e., when the reactions are diffusion controlled. The ideal homogeneous reaction rate is also used to define the Damköhler number of each case.

3.2. Low Damköhler number in turbulence

For low **Da** and diffusion limited reaction rates, the actual reaction rate is higher than the ideal homogeneous reaction rate. This is due to the fact that the ideal homogeneous reaction rate (Eq. (46)) is based on a quiescent flow, for which the Sherwood number is 2 according to the Ranz-Marshall correlation [19]. The actual Sherwood number is higher than 2 because of the relative motion of particle and fluid. The increase in the reaction rate becomes the ratio of the actual Sher-

wood number divided by two. When account is made for the relative fluid-particle velocity due to turbulence, the mean effective diffusion limited particle reaction rate is therefore given by:

$$\underbrace{\alpha_{hom,t}}_{turbulent} = \alpha_{hom,q}\frac{\mathrm{Sh}}{2}. \tag{47}$$

Note that in this regime, the reaction rate still scales linearly with the number density of particles, $\overline{n}_p$.

3.3. High Damköhler number, SC regime

It is known that particles embedded in a turbulent flow will form particle clusters where the particle number density is significantly above the mean value [20, 21, 22]. For large **Da**, the particle number density inside these clusters is very high and the internal oxygen is consumed rapidly. Following the description in the work of Haugen et al. [30], the characteristic length scale l of these particle clusters is obtained by assuming that the eddies responsible for the clustering have the same time scale as the clustering particles, such that $\tau_l = \tau_p = \mathrm{St}\tau_L$. Assuming Kolmogorov scaling between the scales l and L, one obtains $l = L\mathrm{St}^{3/2}$ and $D_{diff,cl} = u_l l = u_{\mathrm{RMS}} L\mathrm{St}^2$ [30]. The subscript cl stands for all cluster related properties. After the internal oxygen is consumed, the reaction rate is limited by the transport of oxygen to the surface of the particle clusters. This is a combustion regime similar to Sheath Combustion [23], and the reaction rate converges to a *particle number density independent* value α_{cl} [30]:

$$\alpha_{cl} = \overline{A}_{cl}\overline{n}_{cl}\overline{k}_{diff,cl} = A_1 A_2 \frac{D_{diff,cl}\mathrm{Sh}}{l^2}. \tag{48}$$

The cluster dependent reaction rate, α_{cl}, is dependent on the mean cluster surface area $\overline{A}_{cl} = A_1 l^2$, the mean cluster number density $\overline{n}_{cl} = A_2/l^3$ and the cluster dependent mass transfer rate $\overline{k}_{diff,cl} = D_{diff,cl}\mathrm{Sh}/l$, where A_1 and A_2 are fitting factors related to the shape of the particle clusters, influencing their number and surface area, respectively. Inserting the expressions for l and $D_{diff,cl}$ into Eq. (48) then yields:

$$\alpha_{cl} = \frac{A_1 A_2 \mathrm{Sh}}{\tau_L \mathrm{St}}. \tag{49}$$

Haugen et al. [30] determined values for $A_1 A_2$ for a range of Re_L and St and they arrive at the following functional dependence; $A_1 A_2 = 0.08 + \mathrm{St}/3$, which predicts the effect of turbulent clustering on the reaction rate in a simpler system. Note that the expression for α_{cl} has no dependence on the number of individual particles.

3.3.1. Connecting IPC and SC combustion regimes

A model for the reaction rate connecting the limits for small and large **Da** (IPC and SC in the terminology of Annamalai and Ramalingam) can be obtained by constructing the harmonic mean:

$$\alpha = \frac{\alpha_{cl}\alpha_{hom,t}}{\alpha_{cl} + \alpha_{hom,t}}. \tag{50}$$

By dividing this expression by the ideal homogeneous reaction rate for a quiescent fluid, a Sherwood correction factor $\tilde{\alpha} = \alpha/\alpha_{hom,q}$ can be found as:

$$\tilde{\alpha} = \frac{\alpha_{cl}}{\alpha_{cl} + \mathrm{DaSh}/(2\tau_L)} \frac{\mathrm{Sh}}{2}. \tag{51}$$

This expression takes into account both the influence of the turbulence on each individual particle via the Sherwood number, as well as the influence of large scale clustering via the cluster dependent reaction rate α_{cl}.

If the chemical timescale, the turbulent flow time scale and the particle Stokes number are known properties the Sherwood correction factor can be obtained and combined with Eq. (37) to obtain a mass transfer rate

$$k_{diff,turb} = \tilde{\alpha} k_{diff,q} \tag{52}$$

that takes into account the effect of small scale turbulence and turbulent clustering.

3.4. Finding the Sherwood correction factor from simulations

To validate the model in Eq. (51), we compare the mean mass loss rates of the particles obtained from the DNS simulations with the mean homogeneous mass loss rate of the same case. In current state of the art RANS models for char conversion, no model exists that accounts for the effect of turbulence on the heterogeneous reactions. The mean homogeneous mass loss rate, which is the mass loss rate one would obtain if small char particles were homogeneously mixed in a quiescent fluid, is therefore what is used in a typical RANS simulation. The aim of this paper is to provide a model for heterogeneous combustion of char that accounts for the effects of turbulence and that can be used for any RANS simulation.

Based on Eq. (34), the mean effective reaction coefficient in a quiescent fluid is given by

$$k_{eff,q} = \frac{k_{kin} k_{diff,q}}{k_{kin} + k_{diff,q}}, \tag{53}$$

when $k_{diff,q}$ is found from Eq. (37). The mean homogeneous mass loss rate is

found by combining Eq. (25) and Eq. (26), such that

$$\frac{d\overline{m}_{p,hom}}{dt} = -\overline{A}_p M_k \sum_{k}^{N_{species}} \widehat{RR}_k. \tag{54}$$

For a single reaction with only one reactant, where the reaction removes one carbon atom from the surface of the char particle, Eqs. (53) and (54) can then be combined with Eqs. (27) and (33) to yield

$$\frac{d\overline{m}_{p,hom}}{dt} = -\overline{A}_p M_c \overline{k}_{eff,q} \overline{X}_{r,\infty} \overline{C}_g. \tag{55}$$

As argued in § 3.3.1, the turbulence only affects the mass transfer rate to the particles, not the kinetic rate. The corresponding mean effective reaction coefficient that incorporates the effect of turbulence is therefore given by

$$k_{eff,turb} = \frac{k_{kin} k_{diff,turb}}{k_{kin} + k_{diff,turb}}, \tag{56}$$

when $k_{diff,turb}$ is found from Eq. (52). Hence, the actual mass loss rate in a turbulent flow is given by

$$\frac{d\overline{m}_p}{dt} = -\overline{A}_p M_c \overline{k}_{eff,turb} \overline{X}_{r,\infty} \overline{C}_g. \tag{57}$$

By combining Eqs. (55) and (57), the ratio of the mean *actual* mass loss rate, which includes the effect of turbulence, to the mean homogeneous mass loss rate, which neglects the effect of turbulence, is found to be

$$\beta = \frac{d\overline{m}_p/dt}{d\overline{m}_{p,hom}/dt} = \frac{k_{eff,turb}}{k_{eff,hom}}. \tag{58}$$

This is a measure of how fast the reactions proceed compared to the homogeneous assumption. From Eqs. (53) and (56), it can then shown that

$$\beta = \frac{k_{kin}\tilde{\alpha}k_{diff,q}/(k_{kin} + \tilde{\alpha}k_{diff,q})}{k_{kin}k_{diff,q}/(k_{kin} + k_{diff,q})} = \frac{\tilde{\alpha}(k_{kin} + k_{diff,q})}{k_{kin} + \tilde{\alpha}k_{diff,q}}. \tag{59}$$

Solving for the Sherwood correction factor, $\tilde{\alpha}$, yields:

$$\tilde{\alpha} = \frac{\beta k_{kin}}{k_{kin} + k_{diff,q}(1-\beta)}. \tag{60}$$

This expression takes into account the effect of the ratio between the kinetic and the diffusive rate on the Sherwood correction factor. When $k_{kin} \gg k_{diff}$, $\tilde{\alpha}$ is nearly proportional to β. However, when the reaction is kinetically controlled, $\tilde{\alpha}$ is less dependent on β. In short, a Sherwood correction factor of 1 describes no change in the reaction rates in comparison to the homogeneous assumption *in a quiescent fluid*, a ratio $\tilde{\alpha} > 1$ signifies a speed-up, and a value $\tilde{\alpha} < 1$ corresponds to a slow-down.

In § 5, the value of $d\overline{m}_p/dt$ is given by the actual mass loss rate obtained from the DNS simulation, while $d\overline{m}_{p,hom}/dt$ is found from Eq. (55). The Sherwood correction factor is then determined from Eq. (60).

4. Simulation setup

For simplicity, char is here considered to react with oxygen to form carbon dioxide. Hence, no homogeneous reactions are present, and the gas phase source term, $\dot{\omega}_k$ in Eq. (5), is zero. The heterogeneous mechanism is taken from the work of Li and You [45] and summarized in table 1. To achieve relatively constant Stokes and **Da** for the duration of the simulation, the particles react with

Table 1: Heterogeneous mechanism

$C + O_2 \rightarrow CO_2$		
$B_n[m/s]$	$\alpha_n[-]$	$E_n[J/mol]$
$1.2{\cdot}10^4$	0	$101{\cdot}10^3$

oxygen present in the fluid and transfer mass to the fluid phase while the particles themselves do not lose mass. This allows us to exclude the effects of varying Damköhler and Stokes numbers, and therefore different clustering or mass transfer behaviour, from the present analysis. The reactions assume a fully dried and devolatilized char particle reacting with oxygen in isotropic and homogeneous turbulence. This setup is ment to resemble what would be observed when studying a small fluid volume that is advected with the mean flow downstream of the zone of gas phase combustion. The Damköhler number is varied from simulation to simulation by varying the number of particles in the domain according to Eq. (45).

4.1. Initialization and start time of reactions

All cases are initialized with random particle positions and then run with reactions disabled until a statistically steady state is reached, which is determined by a stabilization of the shape of the PDF of the particle number density. The evolution of the PDF of the particle number density over time is presented in Fig. (1). As can be seen, the initial distribution is close to a gaussian distribution, which is expected from a true random distribution. As the simulation progresses, the PDF broadens to show a high number of cells with few particles, but also a significant number of cells with many particles. This corresponds to clusters of particles, separated by voids with nearly no particles present. The mean relative velocity between the particles and the fluid varies around a constant value, as shown in

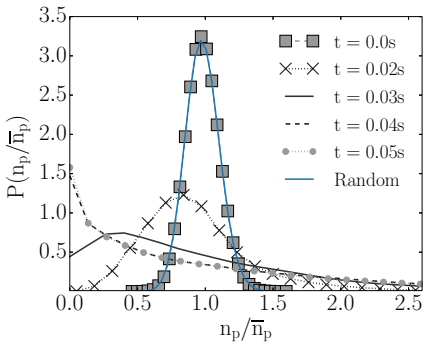

Figure 1: Evolution of the PDF of the particle number density over time

Fig. (2) for a representative case. A simulation time of 0.06 seconds, which corresponds to 16 eddy turnover times, is sufficient to reach a statistically steady state for all cases. The long term variation in relative particle velocity that occur after the reactions are turned on is due to the effect of chemical reactions on temperature and fluid composition. Only data from when the mean oxygen mass faction is still above 1% is taken into account in the subsequent analysis.

4.2. Particle size to grid size dependence

Attention must be given to the fact that the ratio of the particle diameter to the square of the cell size should not exceed a certain value. If a single particle in a cell represents too much reactive surface, the cell's oxygen content is rapidly consumed and a region devoid of oxygen forms around the particle. In the work of Annamalai and Ramalingam [23], this zone is called the film zone and the particle is undergoing Individual Particle Combustion. This is a physical effect, which leads to a reaction rate that is lower than the ideal homogeneous reaction rate, even for small Damköhler numbers. In addition, particles that are large compared

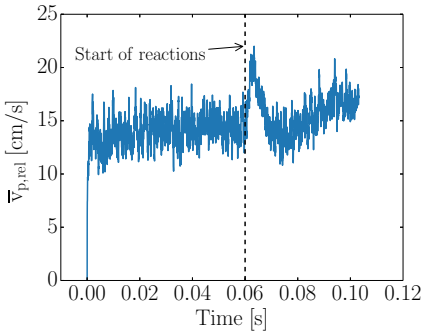

Figure 2: Evolution of the relative particle velocity over time.

to the grid cell tend to introduce numerical instability in the simulations, and, in extreme cases, they will also violate the point-particle assumption that the particle tracking model is based upon. To mitigate these numerical issues, and the forming of a significant "film zone" around each particle, sufficiently small particles are needed. To hold the Damköhler number constant when decreasing the particle surface area, the number density n_p of particles has to be increased according to Eq. (41). This effect is illustrated in Fig. (3), where the Sherwood correction factor is shown to decrease for increasing oxygen conversion and larger ratios of $r_p/\Delta x^2$. The oxygen conversion is defined as:

$$c(t) = 1 - \frac{\overline{Y}_{O_2}(t)}{Y_{O_2,0}}. \tag{61}$$

Figure 4 shows the oxygen mass fraction for simulations with decreasing particle sizes and increasing particle numbers from left to right. All cases have the same low Damköhler number. The areas of low oxygen content around single, large particles are particularly visible in the leftmost panel. Moving towards the right

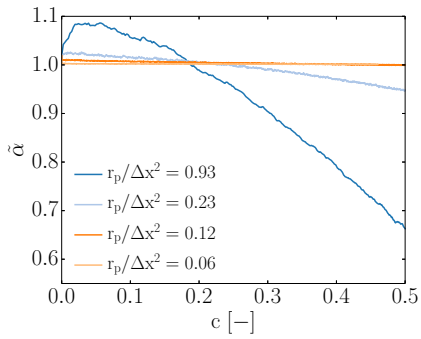

Figure 3: Ratio of the real to the ideal homogeneous reaction rate for a constant Damköhler number of 0.1 for different particle sizes as a function of oxygen conversion.

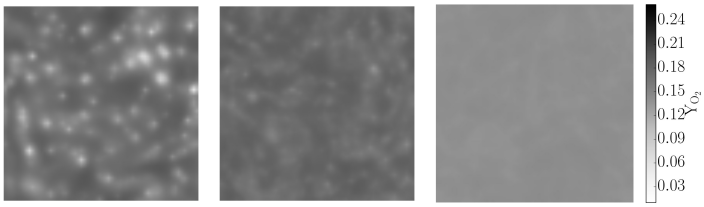

Figure 4: Plots of the oxygen mass fraction for cases with increasing particle numbers and decreasing particle radii at a low and constant Damköhler number.

panel it is clear that for smaller particles, the oxygen distribution is more uniform. When decreasing the particle size, the Damköhler number is kept constant by increasing the particle number density. For turbulent cases, it is also important to maintain the same Stokes number, which is achieved by increasing the material density of the particles.

The Sherwood correction factor is shown as a function of the particle size ($r_p/\Delta x^2$) for Da = 0.1 in Fig. (5). It can be seen from the figure that the Sherwood correction factor starts to decrease for $r_p/\Delta x^2 > 0.12$. This decrease is, as explained previously, due to the presence of a film zone with lower oxygen around

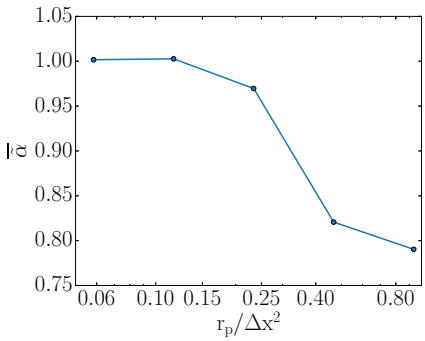

Figure 5: Ratio of the real to the ideal homogeneous reaction rate for a constant Damköhler number of 0.1 over the ratio $r_p/\Delta x^2$.

the large particles. To avoid having to account for the effect of the film zone, a particle radius of 11.25 μm ($r_p/\Delta x^2 = 0.12$) is chosen for the remainder of the simulations. To satisfy the requirement of a Stokes number of unity, a large density ratio between particle and fluid is required. This would not be a requirement for larger Reynolds numbers though, since the flow time scale would be reduced. Table 2 summarizes the general conditions of all simulations.

5. Results

Figure 6 shows the Damköhler number as given by Eq. (42) as a function of oxygen conversion for cases with different particle number densities. Higher particle number densities yield higher **Da**, and the Damköhler number for each case increases until 75% conversion, and then decreases again. The change in fluid diffusivity with temperature is the most important fluid property influencing the variability of the Damköhler number.

Figure 7 shows the ratio of the kinetic to the mass transfer rate for cases with

Table 2: Common boundary conditions of the cases. Here, subscript 0 refers to the initial condition.

$T_{gas,0}$	2100 [K]
$T_{wall,0}$	2100 [K]
$T_{p,0}$	2100 [K]
ρ_{char}	8.55 [g/cm^3]
ρ_{gas}	$3{\cdot}10^{-4}$ [g/cm^3]
u_{RMS}	180.0 [cm/s]
Re	40 [-]
L_f	1/1.5 [cm^{-1}]
$Y_{\mathrm{CO_2},0}$	0.74 [-]
$Y_{\mathrm{O_2},0}$	0.26 [-]
L	6.28 [cm]
r_p	11.25 [μm]
N_{cell}	64^3 [-]

different **Da**, plotted as a function of oxygen conversion. The ratio first increases, with the maximum being higher for lower **Da**. The reason for this is that the amount of oxidizer per particle is higher for lower **Da**. This means that for low **Da**, the particles obtain higher temperatures, and hence larger values of k_{kin}. The decrease in the kinetic rate at later times is due to radiative particle cooling. It is clear from the figure that for these simulations, the char conversion is diffusion controlled for low Damköhler numbers.

5.1. The reaction rate, oxygen consumption and inhibition

The decrease of oxygen content over time can be seen in Fig. (8) for several **Da**. The x-axis is at 1% Y_{O_2}, which illustrates the large differences in time to reach this mass fraction. The case with the highest Damköhler number reaches 1% mass fraction of oxygen after 0.02s, while the case with the lowest Damköhler number takes 60 times longer, i.e. 1.2s. The mean oxygen mass fraction decreases near exponentially, which can be seen in the inset. The exponential decay is expected

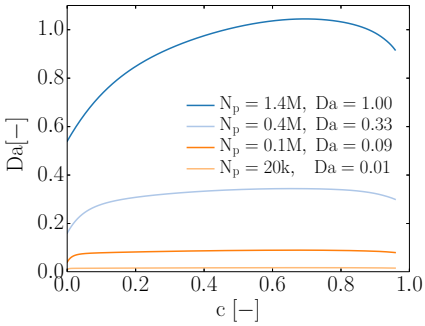

Figure 6: Evolution of the Damköhler number over time.

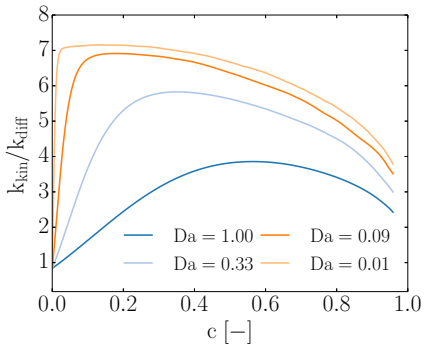

Figure 7: Ratio of kinetic and mass transfer rate over time.

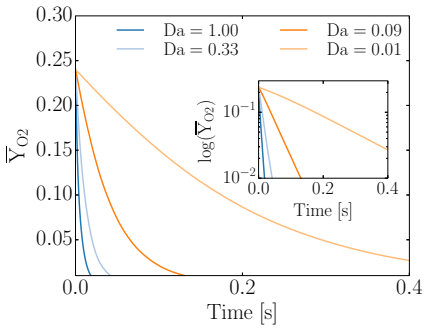

Figure 8: Evolution of the mean oxygen mass fraction over time.

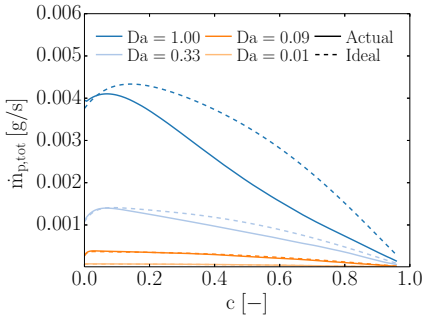

Figure 9: Comparison of ideal and actual total particle mass loss rates over time for simulations with different **Da**.

from a first order reaction equation [29]. In Fig. (9), the actual total particle mass loss rate ($d\overline{m}_p/dt$) and the ideal homogeneous mass loss rate ($d\overline{m}_{p,hom}/dt$), assuming homogeneous distribution of particles, are compared for several **Da**. For low conversions (early times), all cases show comparable ideal and actual mass loss rates. For higher conversion values, the ideal mass loss is higher than the actual one, and the difference is stronger for higher **Da**. The fastest reactions are found in the beginning, when oxygen is still available inside the particle clusters. The

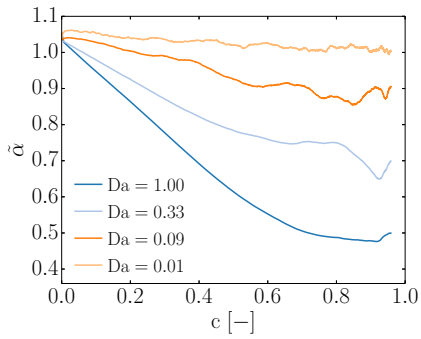

Figure 10: Sherwood correction factor over conversion for simulations with different Damköhler numbers.

reason for the difference between the ideal and the actual mass loss for high **Da** is that the particle clusters become void of oxygen, even though there are large amounts of oxygen available between the clusters. This means that the ideal homogeneous mass loss is only taking into account the total amount of oxygen in the domain or cell, while the actual mass loss is also taking into account the distribution of oxygen and particles. Figure 10 shows the corresponding Sherwood correction factor over conversion, as obtained from Eq. (60), for the same cases as was shown in Fig. (9). The curve ends when the mass fraction of oxygen has reached 1%. The decrease of the Sherwood correction factor for high **Da** is clearly seen. It can also be seen that the Sherwood correction factor has a tendency to decrease with conversion for conversions less than about 50%. The reason that the Sherwood correction factor is higher for early times is that the particles clusters are not yet void of oxygen. For larger conversions, a clear positive or negative trend in the behaviour of the Sherwood correction factor is no longer seen, and we therefore choose to define the steady state Sherwood correct factor as the value

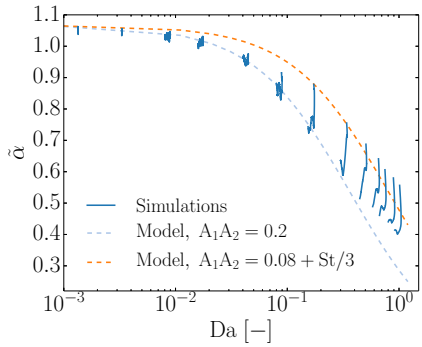

Figure 11: Sherwood correction factor over the Damköhler number

obtained in the range from 50%-99% conversion.

In Fig. (11), the steady state Sherwood correction factor is plotted over Damköhler number for a range of different simulations. The small scale influence of turbulence can be seen in the fact that for small **Da**, the reaction rate is faster than the ideal homogeneous one (i.e. $\tilde{\alpha} > 1$). This is due to the fact that the turbulence induces a relative velocity between the particles and the fluid, which results in fresh reactants constantly being convected to the particle surface, and hence, that the conversion rate is increased.

For large Damköhler numbers (Da > 0.3), the Sherwood correction factor is less than unity. This is due to the effect of the particle clustering, where the fluid in the particle clusters are depleted of oxygen, while there is still significant amounts of oxygen left in the volumes between the clusters. The dashed lines in Fig. (11) represent the model for the Sherwood correction factor, as given by Eq. (51), where the cluster dependent reaction rate, α_{cl}, is given by Eq. (48). The Sherwood number can be found from Eq. (36), when utilizing the model for the relative particle-fluid velocity that was developed by Haugen et al. [30]. Furthermore,

for the upper orange dashed line, the value of A_1A_2 used in Eq. (48) is given by $A_1A_2 = 0.08 + \mathrm{St}/3$, which is taken from Haugen et al. [30]. For comparison, the light blue lower dashed line has been obtained by using $A_1A_2 = 0.2$. It can be seen that the qualitative behaviour of Eq. (51) is fairly similar to the results from the DNS. The model for A_1A_2 as found by Haugen et al. [30], yields a surprisingly good result, even though the physics in their case was more simplified and only mass transfer was considered. This supports the assumption that it is primarily the mass transfer effect that is influenced by the turbulence. We do believe though, that the discrepancy between the simulation results and the model results (orange upper dashed line) is due to the effect of the turbulence on the heat transfer. Finally, it could also be noted that a higher Damköhler number yields a higher variance in the Sherwood correction factor, while the variance is fairly small for the smaller **Da**.

5.2. The distribution of oxygen and temperature in the domain

Figure 12 shows the instantaneous value of the oxygen mass fraction in a slice of the domain when the mean oxygen mass fraction is 15% for three cases with increasing **Da** from left to right. A distinct increase in the difference between the oxygen rich and lean regions is clearly visible for higher **Da**. A high Damköhler number results in a large variance in the oxygen mass fraction, as clusters become depleted of oxygen in a short time, while the regions with low particle number density are left nearly untouched. This effect can be observed in Fig. (13), where a scatter plot of the normalized particle number density as a function of the oxygen mass fraction is shown. The low Damköhler case shows very similar levels of oxygen content for all particle number densities, while the large Damköhler case shows a clear correlation between high relative particle number densities and low

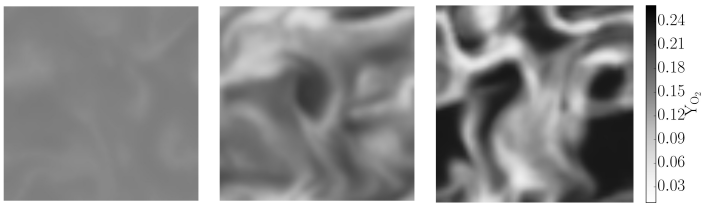

Figure 12: Plots of the oxygen mass fraction for cases with increasing **Da**, 0.01, 0.09 and 1.00 from left to right, $\bar{Y}_{O_2}$ = 15%, the time of the snapshots is 100ms, 6ms and 2ms from left to right.

oxygen content. In Fig. (14) the corresponding PDF of the oxygen mass fraction is shown. The constrained probabilities for regions where the particle number density is higher than its mean value, $n_p > \overline{n}_p$ (dashed line in Fig. (13)), have different positions in the overall distribution. While the constrained distribution for low **Da** fills nearly the full range of values of the unconstrained one, the constrained distribution for the large Damköhler case only covers the lower half of the unconstrained range of values. The values of oxygen mass fraction have a larger spread for higher **Da**. Note that the mean oxygen mass fraction for all cases at the time of the snapshot was around 15%, hence the data is from different times (see Fig. (8)).

Finally the effect of turbulence on the temperature distribution in the domain is studied. The normalized particle number density is plotted as a function of the gas temperature in Fig. (15), and the resulting PDF of the gas temperature is shown in Fig. (16). The mean oxygen mass fraction is 15% for all cases. A higher Damköhler number simulation has a wider range of temperatures and a lower mean temperature than simulations of lower **Da**. The lower mean temperature of the high Damköhler cases is explained by the high number of particles in the domain, which constitute a higher fraction of the energy stored in the particles,

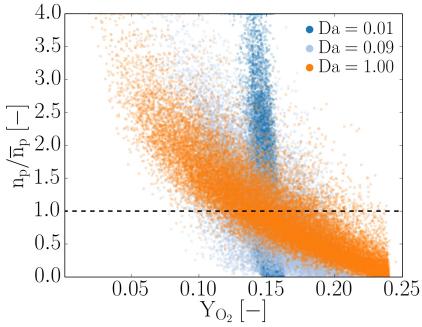

Figure 13: Scatter plot of the particle number density over the oxygen mass fraction. The mean oxygen mass fraction is $\overline{Y}_{O_2} = 15\%$ for all three simulations.

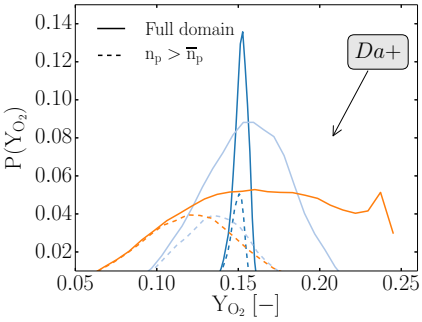

Figure 14: PDF of the oxygen mass fraction for the full domain (continuous lines) and in regions where $n_p > \bar{n}_p$ (dashed lines). Higher **Da** result in broader distributions.

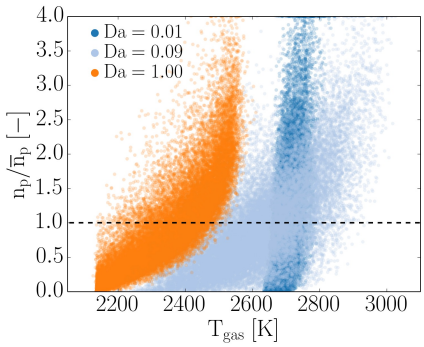

Figure 15: Scatter plot of the particle number over the domain temperature density.

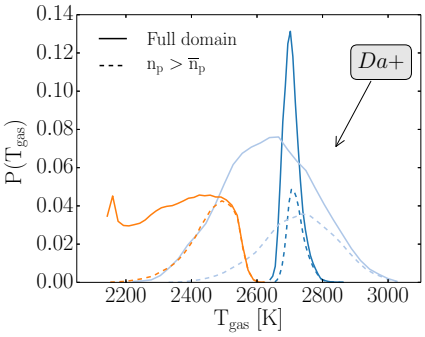

Figure 16: PDF of the domain temperature for cases with three different **Da**. The dashed line represents the subset of the domain where $n_p > \overline{n}_p$.

and an increase in radiation losses from the sum of all particles. The wide range of temperatures found for medium **Da** is believed to be due to the wide range of states the gas can be in. For medium **Da**, parts of the domain have already been emptied of oxygen and cooled down, while other parts have not yet been in contact with particles.

6. Conclusions

The simple model of Haugen et al. [30] and Krüger et al. [29], where DNS was used to analyse heterogeneous reactions in isotropic turbulence, has been extended to incorporate real species and temperature effects. It has been found that the particles form clusters because of the turbulence. Treating the reactions for high **Da** as only occurring on the outer shell of these particle clusters is found to give reasonable results, and a cluster dependent reaction rate α_{cl} is found to yield a good approximation of the maximum rate of reaction that can be achieved for heterogeneous reactions. Haugen et al. [30] has given an approximate value of A_1A_2, which fits the results reasonably well. The fitting factors A_1 and A_2 are factors relating to the number density and surface-to-volume ratio of the particle clusters, both of which depend on the shape of the clusters. Predicting the shape of the particle clusters, and thus values of A_1 and A_2 from flow field and particle properties is the topic of ongoing work. The simulations show the same trend as obtained in the work of Haugen et al. [30] and Krüger et al. [29]. However, using $A_1A_2 = 0.08 + \mathrm{St}/3$ slightly overpredicts the reaction rate for low and medium **Da**. For low and intermediate **Da**, a good fit is achieved with $A_1A_2 = 0.2$, at the cost of underprediction for higher **Da**. The developed model, as presented in Eq. (51), should be used in RANS simulations to account for the effect of turbulence on the

conversion of heterogeneously reacting particles. The model accounts both for 1) the effect of increased mass transfer due to turbulence-induced relative velocities between particles and fluid, and 2) the effect of particle clustering.

The reason for the discrepancies between the results obtained in this work and the results of Haugen et al. [30] are thought to be due to the thermal and kinetic effects that have been included in the current work. In the work of Haugen et al. [30], the consumption of a passive scalar is studied, which does not influence the carrier fluid. Meanwhile, the consumption of oxygen directly affects the density, temperature, composition and momentum of the fluid. Another difference is the lower flow Reynolds number of approximately 40 that has been studied here, while the work of Haugen et al. studies flows with Reynolds numbers in the range of 80-2200.

The Sherwood correction factor is also dependent on the size ratio of the particles and the grid cells size, which are all factors that influence the cost of the simulations. The ratio of particle to grid cell size in the present work was chosen so that the reaction rates at small **Da** behave similar to the homogeneous assumption at reasonable cost and ensure the validity of the point-particle assumption. Increasing the particle size will yield lower Sherwood correction factors. In addition, it tends to yield numerical instabilities.

It is worth noting that extending this analysis to include several heterogeneous and homogeneous reactions will complicate the interpretation of the effect of turbulence. Interestingly, this can result in cases where production/consumption of one species can be modelled by the homogeneous approach, while other species' reactions are happening at the cluster dependent reaction rate.

The proposed model gives a good approximation of the char consumption rate

in reacting flows with heterogeneous reactions. To further improve its predictability, more work has to be done to identify an appropriate correlation for A_1A_2, and to analyse the effect of several heterogeneous and homogeneous reactions, especially for cases where non-unimolar reactions are considered. The effects of particle heating and heat transfer between fluid and particles should also be examined.

Acknowledgements

The research leading to these results has received funding from the Polish-Norwegian Research Programme operated by the National Centre for Research and Development under the Norwegian Financial Mechanism 2009-2014 in the frame of Project Contract No Pol-Nor/232738/101/2014.

References

[1] N. Hashimoto, H. Watanabe, Numerical analysis on effect of furnace scale on heat transfer mechanism of coal particles in pulverized coal combustion field, Fuel Processing Technology 145 (2016) 20 – 30. doi:http://dx.doi.org/10.1016/j.fuproc.2016.01.024.
URL http://www.sciencedirect.com/science/article/pii/S0378382016300236

[2] G. Olenik, O. Stein, A. Kronenburg, LES of swirl-stabilised pulverised coal combustion in IFRF furnace no. 1, Proceedings of the Combustion Institute 35 (3) (2015) 2819 – 2828. doi:http://dx.doi.org/10.1016/j.proci.2014.06.149.

URL http://www.sciencedirect.com/science/article/pii/S1540748914003071

[3] J. H. Chen, A. Choudhary, B. de Supinski, M. DeVries, E. R. Hawkes, S. Klasky, W. K. Liao, K. L. Ma, J. Mellor-Crummey, N. Podhorszki, R. Sankaran, S. Shende, C. S. Yoo, Terascale direct numerical simulations of turbulent combustion using s3d, Computational Science & Discovery 2 (1) (2009) 015001.
URL http://stacks.iop.org/1749-4699/2/i=1/a=015001

[4] J. Kim, P. Moin, R. Moser, Turbulence statistics in fully developed channel flow at low reynolds number, J. Fluid Mech 177 (1987) 133–166.

[5] D. Veynante, L. Vervisch, Turbulent combustion modeling, Progress in Energy and Combustion Science 28 (3) (2002) 193 – 266. doi:http://dx.doi.org/10.1016/S0360-1285(01)00017-X.
URL http://www.sciencedirect.com/science/article/pii/S036012850100017X

[6] T. Poinsot, D. Veynante, Theoretical and Numerical Combustion, Poinsot and Veynante, 2012.

[7] D. Spalding, Mixing and chemical reaction in steady confined turbulent flames, Proceedings of the Combustion Institute (1971) 649–657.

[8] S. B. Pope, Pdf method for turbulent reacting flows., Progr. Energy Combustion Sci. 11 (1985) 119–95.

[9] K. Bray, J. Moss, A unified statistical model of the premixed turbulent flame, Acta Astronautica 4 (3) (1977) 291 – 319.

doi:http://dx.doi.org/10.1016/0094-5765(77)90053-4.
URL http://www.sciencedirect.com/science/article/pii/0094576577900534

[10] S. Pope, The evolution of surfaces in turbulence, International Journal of Engineering Science 26 (5) (1988) 445 – 469. doi:http://dx.doi.org/10.1016/0020-7225(88)90004-3.
URL http://www.sciencedirect.com/science/article/pii/0020722588900043

[11] A. R. Kerstein, W. T. Ashurst, F. A. Williams, Field equation for interface propagation in an unsteady homogeneous flow field, Phys. Rev. A 37 (1988) 2728–2731. doi:10.1103/PhysRevA.37.2728.
URL http://link.aps.org/doi/10.1103/PhysRevA.37.2728

[12] S. Burke, T. Schumann, Diffusion flames, Industrial & Engineering Chemistry 20 (1928) 998–1004.

[13] B. Magnussen, B. Hjertager, On mathematical models of turbulent combustion with special emphasis on soot formation and combustion, Proceedings of the Combustion Institute 16 (1) (1979) 719729.

[14] A. Y. Klimenko, Multicomponent diffusion of various admixtures in turbulent flow, Fluid Dynamics 25 (3) (1990) 327–334. doi:10.1007/BF01049811.
URL http://dx.doi.org/10.1007/BF01049811

[15] R. W. Bilger, , Physics of Fluids A: Fluid Dynamics 5 (2) (1993) 436–444. doi:10.1063/1.858867.
URL https://doi.org/10.1063%2F1.858867

[16] N. Peters, Laminar flame concepts in turbulent combustion, Proceedings of the Combustion Institute 21 (1986) 1231–50.

[17] M. L. de Souza-Santos (Ed.), Solid Fuels Combustion and Gasification, CRC Press, 2010. doi:10.1201/9781420047509.

[18] A. Eaton, L. Smoot, S. Hill, C. Eatough, Components, formulations, solutions, evaluation, and application of comprehensive combustion models, Progress in Energy and Combustion Science 25 (4) (1999) 387 – 436. doi:http://dx.doi.org/10.1016/S0360-1285(99)00008-8.
URL http://www.sciencedirect.com/science/article/pii/S0360128599000088

[19] W. E. Ranz, W. R. Marshall, Evaporation from drops, Chemical Engineering Progress 48 (1952) 141–146.

[20] J. K. Eaton, J. R. Fessler, Preferential concentration of particles by turbulence, International Journal of Multiphase Flow 20 (1994) 169–209.

[21] A. M. Wood, W. Hwang, J. K. Eaton, Preferential concentration of particles in homogeneous and isotropic turbulence, International Journal of Multiphase Flow 31 (2005) 1220–1230.

[22] J. Bec, Fractal clustering of inertial particles in random flows, Physics of Fluids 15 (11) (2003) L81–L84. doi:http://dx.doi.org/10.1063/1.1612500.
URL http://scitation.aip.org/content/aip/journal/pof2/15/11/10.1063/1.1612500

[23] K. Annamalai, S. Ramalingam, Group combustion of char carbon particles, Combustion and Flame 70 (3) (1987) 307–332. doi:10.1016/0010-2180(87)90111-8.

[24] J. Reveillon, F. Demoulin, Evaporating droplets in turbulent reacting flows, Proceedings of the Combustion Institute 31 (2) (2007) 2319 – 2326. doi:http://dx.doi.org/10.1016/j.proci.2006.07.114.
URL //www.sciencedirect.com/science/article/pii/S1540748906001222

[25] K. Luo, H. Wang, J. Fan, F. Yi, Direct Numerical Simulation of Pulverized Coal Combustion in a Hot Vitiated Co-flow, Energy & Fuels 26 (10) (2012) 6128–6136. doi:10.1021/ef301253y.

[26] T. Hara, M. Muto, T. Kitano, R. Kurose, S. Komori, Direct numerical simulation of a pulverized coal jet flame employing a global volatile matter reaction scheme based on detailed reaction mechanism, Combustion and Flame 162 (12) (2015) 4391 – 4407. doi:http://dx.doi.org/10.1016/j.combustflame.2015.07.027.
URL http://www.sciencedirect.com/science/article/pii/S001021801500228X

[27] T. Brosh, N. Chakraborty, Effects of equivalence ratio and turbulent velocity fluctuation on early stages of pulverized coal combustion following localized ignition: A direct numerical simulation analysis, Energy and Fuels 28 (2014) 6077–0688.

[28] T. Brosh, D. Patel, D. Wacks, N. Chakraborty, Numerical investigation of

localised forced ignition of pulverised coal particle-laden mixtures: A direct numerical simulation (dns) analysis, Fuel 145 (2015) 50–62.

[29] J. Krüger, N. E. Haugen, D. Mitra, T. Løvås, The effect of turbulent clustering on particle reactivity, Proceedings of the Combustion Institute (2016) –doi:http://dx.doi.org/10.1016/j.proci.2016.06.187.
URL http://www.sciencedirect.com/science/article/pii/S1540748916302498

[30] N. E. Haugen, J. Krüger, D. Mitra, T. Løvås, The effect of turbulence on mass and heat transfer rates of small inertial particles. doi:arXiv:1701.04567v1.
URL https://arxiv.org/abs/1701.04567

[31] M. B. Tilghman, R. E. Mitchell, Coal and biomass char reactivities in gasification and combustion environments, Combustion and Flame 100 (2014) 100–101.

[32] M. B. Tilghman, N. E. L. Haugen, R. E. Mitchell, A comprehensive char-particle gasification model adequate for entrained-flow and fluidized-bed gasifiers, Energy & Fuelsdoi:10.1021/acs.energyfuels.6b02148.

[33] L. Chen, S. Z. Yong, A. F. Ghoniem, Oxy-fuel combustion of pulverized coal: Characterization, fundamentals, stabilization and CFD modeling, Progress in Energy and Combustion Sciense 38 (2) (2012) 156–214. doi:10.1016/j.pecs.2011.09.003.

[34] A. Brandenburg, Pencil code homepage (July 2014).
URL http://pencil-code.nordita.org/

[35] J. Williamson, Low-storage runge-kutta schemes, Journal of Computational Physics 35 (1) (1980) 48 – 56. doi:http://dx.doi.org/10.1016/0021-9991(80)90033-9.
URL http://www.sciencedirect.com/science/article/pii/0021999180900339

[36] N. Babkovskaia, N. Haugen, A. Brandenburg, A high-order public domain code for direct numerical simulations of turbulent combustion, Journal of Computational Physics 230 (1) (2011) 1 – 12. doi:http://dx.doi.org/10.1016/j.jcp.2010.08.028.
URL http://www.sciencedirect.com/science/article/pii/S0021999110004754

[37] A. Brandenburg, The inverse cascade and nonlinear alpha-effect in simulations of isotropic helical hydromagnetic turbulence, The Astrophysical Journal 550 (2) (2001) 824.
URL http://stacks.iop.org/0004-637X/550/i=2/a=824

[38] N. E. L. Haugen, M. B. Tilghman, R. E. Mitchell, The conversion mode of a porous carbon particle during oxidation and gasification, Combustion and Flame 161 (2) (2014) 612 – 619. doi:http://dx.doi.org/10.1016/j.combustflame.2013.09.012.
URL http://www.sciencedirect.com/science/article/pii/S0010218013003441

[39] S. Sundaram, L. R. Collins, Numerical considerations in simulating a turbulent suspension of finite-volume particles, Journal of Computational Physics 124 (2) (1996) 337 – 350. doi:http://dx.doi.org/10.1006/jcph.1996.0064.

URL http://www.sciencedirect.com/science/article/pii/S0021999196900649

[40] K. D. Squires, J. K. Eaton, Particle response and turbulence modification in isotropic turbulence, Physics of Fluids 7 (1990) 1191–12–3.

[41] S. Elghobashi, G. C. Truesdell, On the two-way interaction between homogeneous turbulence and dispersed solid particles. i: Turbulence modification., Physics of Fluids A 5 (1993) 1790–1801.

[42] N. E. L. Haugen, R. E. Mitchell, M. B. Tilghman, A comprehensive model for char particle conversion in environments containing O2 and CO2, Combustion and Flame 162 (4) (2015) 1455 – 1463. doi:http://dx.doi.org/10.1016/j.combustflame.2014.11.015.
URL http://www.sciencedirect.com/science/article/pii/S0010218014003575

[43] C. T. Crowe, J. D. Schwarzkopf, M. Sommerfeld, Y. Tsuji, Multiphase Flows Droplets, CRC Press, 2012.

[44] M. M. Baum, P. J. Street, Predicting the combustion behaviour of coal particles, Combustion Science and Technology 3 (5) (1971) 231–243. arXiv:http://dx.doi.org/10.1080/00102207108952290, doi:10.1080/00102207108952290.
URL http://dx.doi.org/10.1080/00102207108952290

[45] K. Li, C. You, Particle combustion model simultaneously considering a volatile and carbon reaction, Energy & Fuels 24 (2010) 4178–4184.

List of Figures

List of Tables